

MECHANISMS AND APPLICATIONS OF ELECTROCHEMICAL
NANOPATTERNS

MECHANISMS AND APPLICATIONS OF THE ELECTROCHEMICAL
FORMATION OF NANOPATTERNS

By YUE WANG, B.SC.

A Thesis Submitted to the School of Graduate Studies in Partial Fulfillment of the
Requirements for the Degree Doctor of Philosophy

DOCTOR OF PHILOSOPHY (2015)

McMaster University

(Chemistry and Chemical Biology)

Hamilton, Ontario

TITLE: Mechanisms and Applications of the Electrochemical Formation of Nanopatterns

AUTHOR: Yue Wang, BSc. (Honours, Nanjing University)

SUPERVISOR: Dr. Peter Kruse

NUMBER OF PAGES: xxvii, 175

ABSTRACT

Surface nanofabrication is the art of making novel materials with surface features or patterns smaller than 100 nm. To this end, various techniques have been proposed, *e.g.* optical/ electron lithography, Langmuir Blodgett films, Dip-pen lithography, block co-polymer templates, and ion irradiation. However, each technique has its own inborn limitation, whether time-consuming or expensive or lack of resolution.

In this thesis, the author describes a cheap and time-efficient alternative to generate nanopatterns on several transition metals, alloy, and silicon *via* electrochemical methods and provides more insight into the mechanism that leads to the formation of these patterns.

Self-organized nanopatterns discovered on electropolished vanadium include dots (called pimples), labyrinths (interconnected elongated pimples), and valleys (called dimples).

The window for these patterns to occur is extremely small. A little (0.1%) variance of the electrolyte composition can lead to pattern transition. A time evolution of patterns, from a flat surface to pimple pattern to labyrinth pattern to dimple pattern, has been observed as well.

The author also found out that dimple pattern can be achieved on tantalum *via* electropolishing and nanotubes can be fabricated by anodization. The relative amount of HF and water in the electrolyte is the key that controls the switch between these two patterns.

The author has extended the formation of dimples from pure metals to a biomedical alloy (Ti-6Al-4V). Since the size of the dimple pattern is on the same scale as cell features, this dimpled alloy has great potential in biomedical implantation.

Last but not least, this thesis explores the pattern formation on silicon, a semiconductor, *via* electropolishing, which is thus proven to be a universal nanopatterning technique.

This thesis opens a route to nanopatterning metals, alloys, and semiconductors *via* electropolishing, while making a contribution to a deeper understanding of the mechanisms behind the formation of these patterns.

To those who have touched my life and whose lives I have touched

ACKNOWLEDGEMENTS

I wish to express my genuine gratitude to a number of people whose support and moral encouragement lead to this important scientific piece of work. I could only mention a few by name, but the support of others is not less important. I pay heartfelt tribute to all who have shared part of their scientific lives with me.

I am deeply grateful to my thesis advisor, Dr. Peter Kruse, for his continuous encouragement, for his guidance and, for providing me with necessary means to do the present research.

I am very much obliged to Dr. Kalai Saravanamuttu and Dr. Gillian Goward for being my committee members and for initiating important discussions during my committee meetings.

Moreover, I particularly wish to thank my labmates: Kevin Moonosawmy, Sherdeep Singh, Mark Greiner, Tanzina Chowdhury, Allen Pauric, and Amirmasoud Mohtasebi.

Thanks go also to undergraduates in our group: Bill Ye, Alan Awez, Tsz Ho, Alon Genkin, Phillip G. Daniel-Ivad, Adam Pantaleo, Daniel Manickam, Paul Hodgson, Nathan Costa, Sarwat Baig, Douglas Riddell and Alex Imbault.

I am also deeply indebted to CCEM and CEDT both at McMaster University, CLS at University of Saskatchewan, and Watlabs at Waterloo University for the use of their scientific instruments and Chemistry Main Office at McMaster University.

Last but not least, I would like to thank Lijia Tian, Dr. Svetlana Kostina, Dr. Peng Wang, Ian Duffy, Dr. Corey Thompson, Dr. Steven Burger, and Peter Ho.

Financial support by the ‘Natural Science and Engineering Research Council of Canada’ and from McMaster University is gratefully acknowledged.

TABLE OF CONTENTS

ABSTRACT.....	III
ACKNOWLEDGEMENTS	VI
TABLE OF CONTENTS	VIII
LIST OF FIGURES.....	XIV
LIST OF TABLES.....	XXIV
LIST OF ABBREVIATIONS.....	XXV
DECLARATION OF ACADEMIC ACHIEVEMENT	XXVII
CHAPTER - 1 INTRODUCTION	1
1.1. PATTERN FORMATION.....	1
1.1.1. CONVECTION TYPE PATTERN FORMATION.....	1
1.1.2. REACTION-DIFFUSION TYPE PATTERN FORMATION.....	3
1.1.2.1. TEMPORAL OSCILLATIONS	3
1.1.2.2. FROM TEMPORAL OSCILLATIONS TO SPATIAL PATTERNS.....	4
1.1.2.3. FROM SPATIAL PATTERNS TO STATIONARY TURING PATTERNS.....	5
1.1.3. SUMMARY	8
1.2. PATTERN FORMATION IN ELECTROCHEMICAL SYSTEMS.....	10
1.2.1. THE ELECTROCHEMICAL SYSTEM	10
1.2.1.1. THE ELECTROLYTE/ELECTRODE INTERFACE.....	10
1.2.1.2. THE DOUBLE LAYER	12
1.2.1.3. MASS TRANSPORT	13
1.2.2. ELECTROCHEMICAL PATTERN FORMATION DUE TO CONVECTION.....	14

1.2.3. ELECTROCHEMICAL PATTERN FORMATION DUE TO REACTION-DIFFUSION	17
1.3. NANOPATTERN FORMATION IN ELECTROCHEMICAL SYSTEMS	18
1.3.1. NANOPATTERN FORMATION DURING ANODIZATION.....	19
1.3.1.1. POROUS ANODIC ALUMINA (PAA).....	19
1.3.1.2. OXIDE NANOTUBES	20
1.3.1.3. FORMATION MECHANISM	21
1.3.1.3.1. OXIDE FLOW MODEL	21
1.3.1.3.2. NANOBUBBLE.....	22
1.3.1.3.3. OXYGEN BUBBLE MOULD EFFECT (OBME)	22
1.3.1.3.4. FIELD-ASSISTED DISSOLUTION MODEL.....	22
1.3.2. NANOPATTERN FORMATION DURING ELECTROPOLISHING	24
1.3.2.1. NANOPATTERNS ON AL DURING ELECTROPOLISHING AND THE ADSORPTION MODEL	24
1.3.2.2. CRYSTAL ORIENTATION MODEL	26
1.3.2.3. NANOPATTERN (DIMPLE) ON TA, TI, W AND ZR AND THE CONVECTIVE MODEL	27
1.4. OVERVIEW OF THIS THESIS.....	29
1.5. STRUCTURE OF THIS THESIS.....	30
CHAPTER -2 OVERVIEW OF EXPERIMENTS.....	33
2.1. EXPERIMENTAL SETUP.....	33
2.2. ELECTROPOLISHING.....	34
2.2.1. MACROSMOOTHING	34
2.2.2. MICROSMOOTHING.....	35
2.3. TYPES OF TECHNIQUES	37

2.3.1. CHRONOAMPEROMETRY	37
2.3.2. LINEAR SWEEP VOLTAMMETRY	38
2.3.3. CHRONOPOTENTIOMETRY	39
CHAPTER-3 CHARACTERIZATION TECHNIQUES	41
3.1. ATOMIC FORCE MICROSCOPY (AFM).....	41
3.2. SCANNING ELECTRON MICROSCOPY (SEM)	44
3.2.1. SEM IMAGING	45
3.2.2. CONTAMINATION	47
3.2.3. CHARGING.....	47
3.2.4. ENERGY-DISPERSIVE X-RAY SPECTROSCOPY (EDX)	48
3.3. PHOTOEMISSION ELECTRON MICROSCOPY (PEEM)	50
3.4. ABSORPTION SPECTROSCOPY (VIS).....	51
CHAPTER-4 NANO-PATTERNING VANADIUM VIA	
ELECTROPOLISHING	53
4.1. INTRODUCTION	53
4.2. EXPERIMENTAL	54
4.3. RESULTS	57
4.3.1. THE FORMATION OF PATTERNS	58
4.3.2. WHAT MATTERS?	62
4.3.2.1. WATER IN THE ELECTROLYTE	62
4.3.2.2. HF IN THE ELECTROLYTE	65
4.3.2.3. WATER-HF BALANCE	67
4.3.2.4. ELECTROPOLISHING POTENTIAL.....	69
4.3.2.5. TIME EVOLUTION.....	72

4.3.2.6. ELECTRODE SIZE VS. ELECTROLYTE VOLUME	75
4.3.2.7. AGING ELECTROLYTE	77
4.3.2.8. NATIVE OXIDE	79
4.4. DISCUSSION	80
4.4.1. ON ELECTROPOLISHING	80
4.4.1.1. THE IONS FORMED DURING ELECTROPOLISHING	80
4.4.1.2. MASS TRANSPORT OF VO_2^+	81
4.4.2. ON PATTERN FORMATION	84
4.4.2.1. ANODIC-OXIDE-BASED MODELS	84
4.4.2.2. LIQUID-PHASE-BASED MODELS	85
4.4.2.2.1. POLAR ADSORBATE MODEL	85
4.4.2.2.2. REACTION-DIFFUSION MODEL	87
4.4.2.2.3. THE CONVECTION MODEL	87
4.4.3. PATTERN FORMATION IN A BASIC ELECTROLYTE	89
4.5. CONCLUSION	91

CHAPTER-5 FORMATION OF NANOTUBES AND NANOPATTERNS ON TANTALUM.....92

5.1. INTRODUCTION	92
5.2. EXPERIMENTAL	94
5.3. RESULTS	96
5.3.1. FORMATION OF TANTALUM DIMPLE ARRAY AND NANOTUBES	96
5.3.2. METALLIC DIMPLES VS. OXIDE NANOTUBES	97
5.3.2.1. SIZE VARIANCE OF DIMPLES	99
5.3.2.2. DIFFERENT PATTERNS?	102
5.3.3. CHRONOAMPEROMETRY OF DIMPLES AND NANOTUBES	103

5.3.4. ELECTROLYTE'S IMPACT ON DIMPLES <i>VS.</i> NANOTUBES.....	104
5.3.4.1. WATER	104
5.3.4.2. HF	105
5.3.5. QUANTIFYING THE AMOUNT OF NANOTUBES.....	106
5.3.6. PHASE DIAGRAM – H ₂ O <i>VS</i> HF	107
5.4. DISCUSSION	109
5.4.1. COMPARISON WITH THE VANADIUM SYSTEM.....	109
5.4.2. PHASE DIAGRAM.....	109
5.4.3. DIMPLE OR NANOTUBE?.....	110
5.5. CONCLUSION	110
CHAPTER-6 NANO-PATTERNING A BIOMEDICAL ALLOY (Ti-6Al-4V) VIA ELECTROPOLISHING.....	112
6.1. INTRODUCTION	112
6.2. EXPERIMENTAL	114
6.3. RESULTS AND DISCUSSION	116
6.3.1. OPTIMUM CONDITIONS TO DIMPLE Ti-6Al-4V	116
6.3.1.1. ELECTROLYTE COMPOSITION	116
6.3.1.2. POTENTIAL	118
6.3.1.3. ELECTROPOLISHING TIME.....	119
6.3.2. EFFECT OF SURFACE COMPOSITION	121
6.3.2.1. EDX.....	122
6.3.2.2. PEEM.....	123
6.4. CONCLUSION	132
CHAPTER-7 NANO-PATTERNING SILICON VIA ELECTROPOLISHING	134

7.1. INTRODUCTION	134
7.2. EXPERIMENTAL	134
7.3. RESULTS	135
7.3.1. POROUS SILICON AND YELLOW SILICON OXIDE	135
7.3.2. ‘FENCE’ AND DISORDERED NANOPATTERN IN DILUTE HF	139
7.3.3. DIMPLE PATTERN - TUNING THE ELECTROLYTE	141
7.3.3.1. SODIUM FLUORIDE	142
7.3.3.2. NH ₄ F	143
7.3.3.3. ACETIC ACID/HF	144
7.3.3.4. ETHYLENE GLYCOL/HF	145
7.4. CONCLUSION	146
CHAPTER-8 CONCLUSIONS AND OUTLOOK	147
BIBLIOGRAPHY	151
APPENDIX.....	165
10.1. APPENDIX A. LABVIEW PROGRAM.....	165
10.2. APPENDIX B CERTIFICATES OF ANALYSIS	169

LIST OF FIGURES

Figure 1.1. The formation of patterns due to Rayleigh-Benard type convection (A) and Reaction-diffusion (B). (Adapted by permission from Elsevier: <i>Int. J. Heat Mass Transf.</i> , Ref. ⁴ , copyright 1974 and Macmillan Publishers Ltd: <i>Nature</i> , Ref. ⁵ , copyright 1970).....	1
Figure 1.2. Heat conduction (A) and heat convection (B), which gives birth to the convective pattern in Figure 1.1a.	2
Figure 1.3. The origin of oscillations in nonlinear system.	4
Figure 1.4. The propagation of concentration waves in a two-dimensional oscillating chemical system. (Reprinted by permission from Macmillan Publishers Ltd: <i>Nature</i> , Ref ⁵ , copyright 1970).....	5
Figure 1.5. The Activator-Inhibitor mechanism.	6
Figure 1.6. The formation of Turing pattern: (a) stationary patterns, (b) spots, (c) stripes, and (d) transition of stripes into spots, in a reactor mixed with $\text{CH}_2(\text{COOH})_2$, NaOH, Na_2SO_4 , H_2SO_4 and ClO_2^- . (Reprinted by permission from Macmillan Publishers Ltd: <i>Nature</i> , Ref ¹³ , copyright 1991)	7
Figure 1.7. Charge transfer at the electrode/electrolyte interface	11
Figure 1.8. Double layer model. NB: the charge on the electrode in this figure is positive and the charge in the electrolyte is negative in this case.	12
Figure 1.9. Mass transport of ions across the diffuse layer: diffusion, migration and convection.	13
Figure 1.10. Unstable convective cells. Convection can occur where convection cells form, grow, break, merge, and reform at the surface, as the moving gradient layer moves	

farther from the electrode. (Reprinted by permission from American Chemical Society: <i>J. Phys. Chem. C</i> , Ref ³⁵ , copyright 2007).....	15
Figure 1.11. Evolution of the luminescent pattern on ITO electrode due to convection within ion depletion layer. The size of the image is 2.4 x 3 mm ² . (Reprinted by permission from PCCP Owner Societies: <i>Phys. Chem. Chem. Phys.</i> , Ref. ³⁶ , copyright 2000)	17
Figure 1.12. Formation of porous anodic alumina with hexagonally-close-packed nanopores. (Reprinted by permission from AIP Publishing LLC: <i>Appl. Phys. Lett.</i> , Ref. ⁷⁰ , Copyright 1998.).....	19
Figure 1.13. Large scale (a) and zoom-in (b, c) SEM images of nanotube formation on tantalum. (Reprinted by permission from The Royal Society of Chemistry: <i>J. Mater. Chem.</i> , Ref ⁷⁶ , Copyright 2009.)	20
Figure 1.14. The velocity vectors (red arrows) of oxide flow during the formation of the oxide nanopores or nanotubes (colour scale is stress). (Adapted by permission from Macmillan Publishers Ltd: <i>Nat. Mater.</i> , Ref ⁸⁴ , Copyright 2009.)	21
Figure 1.15. The formation of the nanobubbles during the anodization of W in NaOH. (Adapted by permission from American Chemical Society: <i>J. Phys. Chem. C</i> , Ref ⁸⁶ , copyright 2011).	22
Figure 1.16. Chemical reactions at the base of a pore during pore formation.	23
Figure 1.17. Different kinds of patterns formed on aluminum <i>via</i> electropolishing at different potentials and time intervals. (Reprinted by permission from Springer: <i>J. Electron. Mater.</i> , Ref ⁹⁴ , copyright 1996)	24

Figure 1.18. The surfactant molecules in the electric double layer shields the electrode surface and form a pattern.....	25
Figure 1.19. SEM images of the dimple pattern formed on tantalum, titanium, tungsten, and zirconium. (Reprinted by permission from American Chemical Society: <i>ACS Nano</i> , Ref ⁶² , copyright 2008).	27
Figure 1.20. The formation of convective cells within the double layer during electropolishing, which leads to the dimple pattern on the working electrode surface. (Reprinted by permission from American Chemical Society: <i>ACS Nano</i> , Ref ⁶² , copyright 2008).	29
Figure 2.1. Scheme of a typical electropolishing cell	33
Figure 2.2. Macrosmoothing. The current density is higher at the protruding part than the receding part. As a result, the protruding part gets etched more, which levels the electrode surface.	35
Figure 2.3. Proposed mass transport limiting species: dissolved ions (a), acceptor anion (b), and water (c).	36
Figure 2.4. Probing the electrochemical system.	37
Figure 2.5. In chronoamperometry, the potential is constant(a), the ion concentration gradient profile at different time intervals (b) and the corresponding <i>i-t</i> curve (c).	38
Figure 2.6. Linear potential sweep (a) and resulting <i>i-E</i> curve (b).	39
Figure 2.7. The <i>E-t</i> curve in galvanostatic study.	40
Figure 3.1. The light level system in AFM.	42
Figure 3.2. The atomic force interaction between the sample and the tip.	43

Figure 3.3. Interaction volume.....	45
Figure 3.4. Topographic contrast in SEM due to the loss of secondary electrons (red dashed).	46
Figure 3.5. Example of poor-quality SEM image due to surface contamination.....	47
Figure 3.6. Example of poor-quality SEM image of tantalum nanotube due to charging. 48	
Figure 3.7. The origin of the X-ray photon formed in EDX.....	49
Figure 3.8. EDX of dimple pattern on biomedical alloy (Ti-6Al-4V).....	50
Figure 4.1 The electrochemical setup during electropolishing.	56
Figure 4.2. The <i>Vis.</i> Spectra taken before and after electropolishing confirms the formation of VO_2^+ during electropolishing. ¹³⁷	58
Figure 4.3. SEM images of the electropolished vanadium surfaces. a) Flat surface, b) Pimple pattern, c) Labyrinth pattern, and d) Dimple pattern (Scale bar 100 nm).	59
Figure 4.4. 3D AFM images of the dimple and pimple pattern and cross section profile of each pattern. The average depth of dimple is about 7nm and the average height of pimple is about 4nm and dimple is wider than pimple. (NB: the y-scale difference in the 3D AFM images and the cross-section profile AFM images.).....	61
Figure 4.5. The transition of patterns due to the water concentration variance in the electrolyte. Each sample (a ~ f) is electropolished at 20V for 5 minutes, but in different electrolytes, as listed in Table 4.3. (Scale bar: 100 nm)	64
Figure 4.6. Patterns' dependence on the HF concentration in the electrolyte. Each sample (a~f) is electropolished for 5 minutes at 20V in electrolytes listed in Table 2. (Scale bar: 100 nm)	66

Figure 4.7. Phase diagram of all the patterns on vanadium electropolished in different electrolytes. The flat pattern is highlighted with red colour; pimple yellow colour; labyrinth green colour; dimple blue colour; and random pink collar.	67
Figure 4.8. Pattern's dependence on potential. Each sample is electropolished in the 98.7% H ₂ SO ₄ , 0.4% H ₂ O and 0.9% electrolyte for 5 minutes at different potentials: a) 10V, b) 15V, c) 17.5V, d) 20V, e) 22.5V, f) 25V. (Scale bar 100 nm)	70
Figure 4.9. Fast Fourier Transform (FFT) of an SEM image (left).	71
Figure 4.10. Potential's impact on the pattern's periodicity. As the potential increases, the spacing between each pattern also increases.....	72
Figure 4.11. The pattern evolution also depends on the electropolishing time. Sample a~f are electropolished in 99% H ₂ SO ₄ , 0.6% HF and 0.4% H ₂ O electrolyte for a) 30 seconds, b) 2 minutes, c) 5 minutes, d) 15 minutes, e) 30 minutes and f) 120 minutes. (Scale bar: 100nm)	74
Figure 4.12. SEM images of samples in Table 4.5.	76
Figure 4.13. The initial current spike compared to normal current during electropolishing. The spike sample have been oxidized during the 15-minute sonication in water before electropolishing	80
Figure 4.14. The formation of the 'viscous layer' during electropolishing. The blue curve indicates the relative concentration of dissolved ions, which decreases as it moves away from the anode towards the bulk electrolyte.	82
Figure 4.15. The nanoscale pattern formed on vanadium upon electropolishing at 10V in 2.4M NaOH for 1 minute.....	90

Figure 5.1. Large-scale and zoomed-in SEM images of dimple pattern (a, c) and nanotubes (b, d) and their EDX analyses.	97
Figure 5.2. TEM images of dimples on tantalum (a) EELS line-scan of dimples on tantalum (b) TEM image of the base of dimples and the electron diffraction pattern (c) TEM image of the oxide layer and the electron diffraction pattern. (Data taken by Dr. Sherdeep Singh)	99
Figure 5.3. Large-scale SEM image shows the size modulation of dimples of tantalum electropolished for 5min.	100
Figure 5.4. AFM image of dimple size variance on electropolished tantalum, with profiling at spot A and B.	101
Figure 5.5. SEM images of the surface morphologies on the electropolished tantalum at current density of 20 mA/cm ² (a), 40 mA/cm ² (b), 70 mA/cm ² (c), 100 mA/cm ² (d), 160 mA/cm ² (e), 170 mA/cm ² (f).....	102
Figure 5.6. The formation of stripe pattern on tantalum.	103
Figure 5.7. The formation of tantalum oxide nanotubes as water concentration increases and their corresponding <i>i-t</i> curve. Curve 1 is for sample b; 2 for c; 3 for d, respectively.	104
Figure 5.8. Large scale and zoomed-in (inserts) SEM images of samples dipped in electrolyte for 0 seconds (a), 15 seconds (b), 4 min (c), and 3 hours (d) after electropolishing.	106
Figure 5.9. SEM images of dimple pattern with nanotubes and their binary figures, black: nanotubes, white: dimple pattern.	107

Figure 5.10. Phase diagram showing the formation dimple pattern and nanotube subject to the water and HF concentration in the electrolyte.	108
Figure 6.1. SEM images of electropolished titanium alloy surfaces showing the deterioration of the long range order of dimples as one moves away from the narrow electrochemical regime of ordered pattern (dimples) formation by changing the concentration: (a) 9:1 H ₂ SO ₄ / HF; (b) 8.5:1.5 H ₂ SO ₄ / HF; (c) 8:2 H ₂ SO ₄ / HF; (d) 7.5:2.5 H ₂ SO ₄ / HF. The potential is kept at 15 V through all the samples and the electropolishing time is 300 seconds.	117
Figure 6.2. SEM images of electropolished titanium alloy surface showing the deterioration of the long range order of dimples as one moves away from the narrow electrochemical regime of ordered pattern (dimples) formation by changing the concentration: (a) 13V; (b) 15V; (c) 17V; (d) 20V. The electrolyte solutions for all samples are 8:2 (volume ratio) H ₂ SO ₄ / HF, and the electropolishing time is 300 seconds.	119
Figure 6.3. Large scale (a) and high resolution (b) SEM images of titanium alloy samples electropolished for 30 seconds; large scale (c) and high resolution (d) SEM images of titanium alloy samples electropolished for 120 seconds. The electrolyte for this time series experiment is 8:2 (volume ratio) H ₂ SO ₄ / HF and the cell potential is kept at 15 V.	121
Figure 6.4. Large scale SEM image of titanium sample dimpled under optimized conditions, showing that dimples are not uniform in size across the whole surface.	122

Figure 6.5. EDX of dimpled titanium alloy sample. Titanium $K\beta_1$ peak (4.931 KeV) overlaps with vanadium $K\alpha_1$ (4.952 KeV), $K\alpha_2$ (4.944 KeV) peaks.....	123
Figure 6.6. X-ray Absorption Spectra (XAS) of titanium (a), vanadium (b), aluminum (c) obtained by PEEM.	125
Figure 6.7. High-resolution synchrotron images of control sample. Image <i>a,b,c</i> are synchrotron images captured at baseline, images from d to f are synchrotron images taken at titanium peak (465 eV), vanadium peak (516 eV), Aluminum peak (1566 eV) correspondingly. Image g (the ratio of image d to image a) is the titanium map of the control sample; image h (the ratio of image e to image b) is the vanadium map; image i (the ratio of image f to image c) is the Aluminum map. All images are rescaled for viewing.....	126
Figure 6.8. The Hg lamp image (a) of the un-dimpled sample (control) and its surface element maps of titanium (b), vanadium (c) and aluminum (d). NB: differences between each colour bar.	127
Figure 6.9. The correlation of the PEEM Hg lamp image of the dimpled titanium alloy sample with its SEM image.	128
Figure 6.10. High-resolution synchrotron images of dimpled sample. Images (a) to (c) are synchrotron images captured at baseline, images from d to f are synchrotron images taken at titanium peak (465 eV), vanadium peak (516 eV), Aluminum peak (1566 eV) correspondingly. Image (g), the ratio of image (d) to (a) is the titanium map of the control sample; image (h), the ratio of image (e) to (b) is the vanadium map; image (i), the ratio of image (f) to (c) is the Aluminum map. All images are rescaled for viewing.	129

Figure 6.11. The Hg lamp image (a) of the dimpled sample and its surface element maps of titanium (b), vanadium (c) and aluminum (d) at the ‘V’ shape scratch. NB: differences between each colour bar.....	130
Figure 6.12. (a) High-resolution SEM image of Figure 6.11; there are dimples off the plateau (b); (c) there are no dimples on the plateau, where the concentration of vanadium is relatively higher.....	131
Figure 6.13. SEM image of vanadium electropolished in 8:2 H ₂ SO ₄ / HF (volume ratio) electrolyte at 15 V for 2 min, showing that the surface is rough at microscale.....	132
Figure 7.1. SEM image of the porous silicon, electropolished in 8:2 (98% sulphuric acid to 48% HF, volume ratio) at 15V.....	136
Figure 7.2. Anodized in the 8:2 (volume ratio of concentrated sulfuric acid to concentrated HF) at 20V, a layer of yellow oxide is formed on the surface and began to detach off the surface.	137
Figure 7.3. An optical image captured by an AFM camera shows the coloured layer-type structures on the surface.....	137
Figure 7.4. Optical microscope picture of sample shown in Figure 7.1.	138
Figure 7.5. SEM image of the sample with covered by the yellow oxide. The yellow colour originates from structures on the peeling surface.	139
Figure 7.6. SEM image of the ‘fence’ structure formed on silicon sample, which have been electropolished in 1% HF at 30V.	140
Figure 7.7. Cross-section SEM image of sample in Figure 7.6.	140
Figure 7.8. EDX of ‘fence’ structure.	141

Figure 7.9. SEM of silicon electropolished at 15V in 5 percent HF for 5minutes	142
Figure 7.10 Oscillations in current during the electropolishing of silicon.	142
Figure 7.11. Silicon electropolished at 15V in 1M NaF	143
Figure 7.12. Porous silicon is achieved after the silicon sample is electropolished in 50% acetic acid with 5% HF at 15V	144
Figure 7.13. SEM image of the silicon sample electropolished in 40% acetic acid+ 6.5% HF at 17.5V for 5 minutes.	145
Figure 7.14. SEM of silicon electropolished in ethylene glycol (EG) and HF at 22V. The volume ratio of EG to HF is 4.5:1.....	146
Figure 10.1 The front panel of the Labview program for Picoammeter.	165
Figure 10.2 The background wiring of the Labview program for Picoammeter.	166
Figure 10.3. The Labview front panel of Version 2.0 for <i>Keithley 487</i>	167

LIST OF TABLES

Table 1.1. The comparison of self-assembly patterning and dissipative patterning	9
Table 1.2 Summary of dimple morphologies on different metals and fabrication conditions.....	28
Table 4.1. The different oxidation numbers of vanadium and colours	54
Table 4.2. The detailed breakdown of electrolytes for flat surface, pimples, labyrinths, and dimples on vanadium during electropolishing.	59
Table 4.3. The composition (wt. %) of electrolytes in the water concentration varying experiment. The number of samples correspond with the image number in Figure 4.5....	63
Table 4.4. The composition (wt. %) of electrolytes in the HF concentration varying experiment. The number of samples correspond with the image number in Figure 4.6....	65
Table 4.5. The impact of electrode surface area and the volume of the electrolyte on patterns' evolution.	76
Table 4.6 Reference samples for Aging Electrolyte Experiment.....	77
Table 4.7. Test samples in Aging Electrolyte Experiment	78
Table 5.1. The composition of electrolyte in Figure 5.7.....	105

LIST OF ABBREVIATIONS

AFM	Atomic Force Microscope
BZ	Belousov-Zhabotinsky
CaPeRS	Canadian Photoemission Electron Research Spectromicroscope
CE	Counter Electrode
CLS	Canadian Light Source
DPA	9, 10-diphenylanthracene
EDX	Energy-Dispersive X-ray Spectroscopy
FFT	Fast Fourier transform
EG	Ethylene Glycol
HA	Hydroxyapatite
HF	Hydrofluoric Acid
IHP	Inner Helmholtz Plane
MFP	Mean Free Path
OHP	Outer Helmholtz Plane
PAA	Porous Anodic Alumina
PEEM	Photoemission Electron Microscope

RB	Rayleigh Benard
RE	Reference Electrode
SCE	Saturated Calomel Electrode
SEM	Scanning Electron Microscope
SHE	Standard Hydrogen Electrode
STM	Scanning Tunnelling Microscope
TEM	Transmission Electron Microscope
WE	Working Electrode
XAS	X-ray Absorption Spectra

DECLARATION OF ACADEMIC ACHIEVEMENT

Authors' contribution

Chapter 4 is based on a manuscript that will be submitted for publication.

Contributions are as follows: the thesis author prepared, designed, conducted experiments, analyzed the data, put together figures and wrote the manuscript draft in constant consultation with Dr. Peter Kruse. Alan Awez conducted the base experiments.

Chapter 5 is based on a manuscript that will be submitted for publication.

Contributions are as follows: the thesis author prepared, designed, conducted experiments, analyzed the data, put together figures and wrote the manuscript draft in constant consultation with Dr. Peter Kruse. Dr. Sherdeep Singh conducted the TEM measurement.

Chapter 6 is based on a manuscript which has been reproduced with permission from *AIP Adv.* **2012**, 2, 032101. Copyright 2012, American Institute of Physics.

Contributions for the work presented in chapter 6 are as follows: the thesis author prepared, designed, conducted experiments, analyzed the data, put together figures and wrote the manuscript draft as presented in this chapter in constant consultation with Dr. Peter Kruse. Sherdeep Singh participated in the discussion.

CHAPTER - 1

INTRODUCTION

1.1. PATTERN FORMATION

Patterns with perfect symmetries are spectacular and attractive for their eye-catching appearances (Figure 1.1) and intriguing formation mechanisms.¹ Examples of pattern formation are everywhere (for example clouds and sand ripples), though some of the patterns may not seem that obvious to us (for example stripes on zebrafish² and ant colonies³).

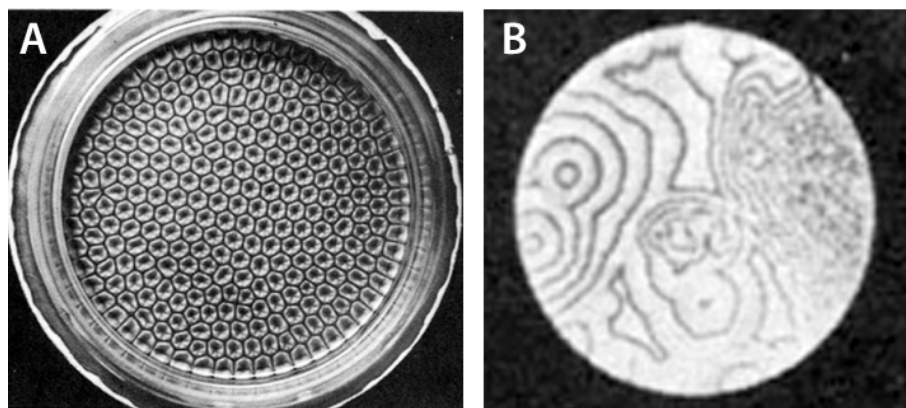


Figure 1.1. The formation of patterns due to Rayleigh-Benard type convection (A) and Reaction-diffusion (B). (Adapted by permission from Elsevier: *Int. J. Heat Mass Transf.*, Ref. ⁴, copyright 1974 and Macmillan Publishers Ltd: *Nature*, Ref. ⁵, copyright 1970)

1.1.1. CONVECTION TYPE PATTERN FORMATION

The formation of a cloud is an example of heat convection. Within cooler air, warm air rises with moisture. During this process, the water vapor in the warm air condenses and forms clouds.

A simple convective pattern to recreate is the Rayleigh-Benard type convection (Figure 1.1A). If a thin layer of oil is heated in a pan, a temperature gradient will be established inside the oil layer *via* heat conduction (red arrows in Figure 1.2A).

If the oil is further heated, conduction alone is no longer sufficient to transfer the excess heat. The oil layer close to the bottom will expand and become less dense. As a result, the top layer oil will move down because of gravity, which will push up the bottom layer. Because of space limitations, the top and bottom layer cannot exchange as a whole. The most efficient way for them to exchange is through convection cells.⁶

Convective rolls can be observed from the top of the pan (Figure 1.2B).

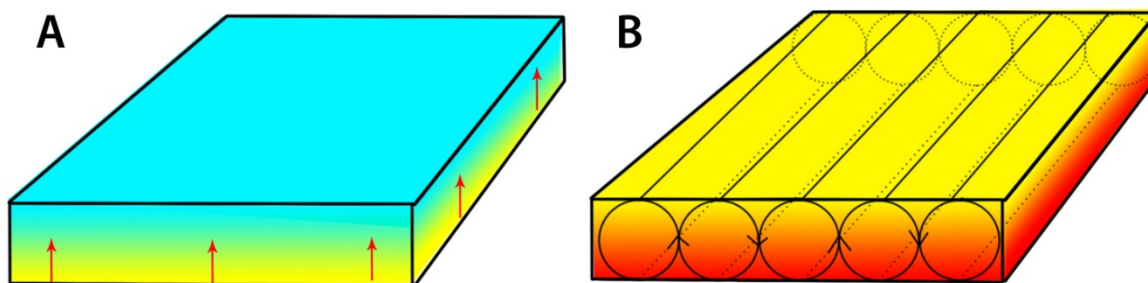


Figure 1.2. Heat conduction (A) and heat convection (B), which gives birth to the convective pattern in Figure 1.1a.

In the above system, the heat-induced buoyancy force $\rho_0 \alpha g \Delta T$ destabilizes the system, which is offset by the stabilizing dissipative force $\nu \kappa \rho_0 / d^3$. The dimensionless ratio of the destabilizing force over the stabilizing dissipative force is called Rayleigh number, R

$$R = \frac{\alpha g \Delta T d^3}{\kappa \nu} = \frac{\text{destabilizing force}}{\text{stabilizing dissipative force}}$$

,where α is the thermal expansion coefficient, g the acceleration of gravity, ν the viscosity, κ the thermal diffusivity and d the size of convective cells.

Only when the Rayleigh number reaches a critical value (R_c), the convective rolls start to form within the oil layer.

1.1.2. REACTION-DIFFUSION TYPE PATTERN FORMATION

1.1.2.1. TEMPORAL OSCILLATIONS

Another group of pattern formation is produced by reaction and diffusion, a phenomenon which is first witnessed by Boris P. Belousov.⁷ From a mixture of potassium bromate, citric acid, and cerium ions, he observes a periodic colour change.⁸ This colour oscillation, however, was believed to contradict the second thermodynamics law at that time, which states that reactions can only proceed in one direction with increasing entropy (S). As a result, Belousov couldn't publish his work in any major journals, and they were dismissed as unscientific.

Zhabotinsky improved Belousov's recipe by replacing citric acid with malonic acid and demonstrated that the periodic colour change is caused by the cyclic oxidation and reduction of the Ce^{3+}/Ce^{4+} . The complete mechanism of the Belousov-Zhabotinsky (BZ) reaction is much more complicated than that, involving a total of 18 reactions with 21 compounds.⁹ The proposed mechanism is nonlinear in essence, which explains the colour oscillation.

In a nonlinear system, for simplicity take $x = y^2$ as an example (Figure 1.3), both State 1 (\sqrt{x}) and State 2 ($-\sqrt{x}$) are valid states. As a result, the BZ reaction can jump

between these two states. Constant jump between these two states cause oscillations. Eventually, intermediates in the BZ reaction will be used up and the oscillations will stop, which still obeys the second thermodynamic law.

Nonlinear systems in the real world are much more complicated than the example given below (Figure 1.3).

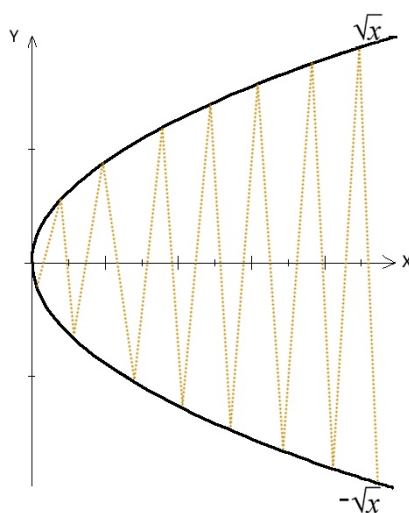


Figure 1.3. The origin of oscillations in nonlinear system.

1.1.2.2. FROM TEMPORAL OSCILLATIONS TO SPATIAL PATTERNS

In a well-stirred beaker, the BZ reaction can start simultaneously everywhere, due to the stirring. However, when confined to an unstirred petri-dish, the BZ reaction loses the global coupling and can only initiate at certain spots/defects, in which case, propagations of concentration waves can be observed¹⁰, as shown in Figure 1.4.⁵

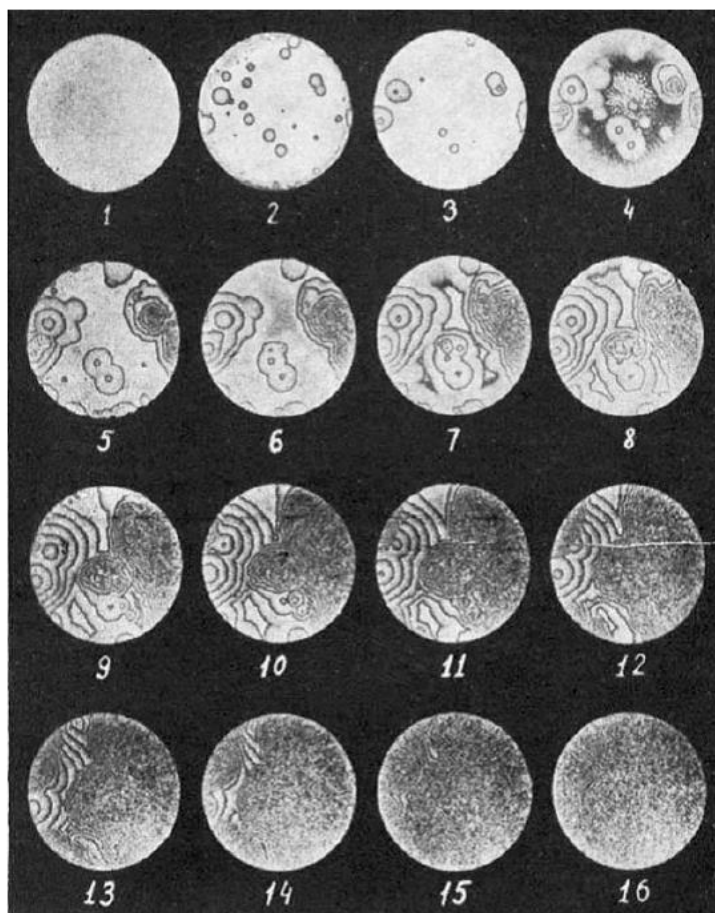


Figure 1.4. The propagation of concentration waves in a two-dimensional oscillating chemical system. (Reprinted by permission from Macmillan Publishers Ltd: *Nature*, Ref ⁵, copyright 1970)

1.1.2.3. FROM SPATIAL PATTERNS TO STATIONARY TURING PATTERNS

Roughly at the same time when Belousov observed these temporal colour oscillations, Turing showed mathematically that stationary patterns can arise from the reaction-diffusion system.¹¹

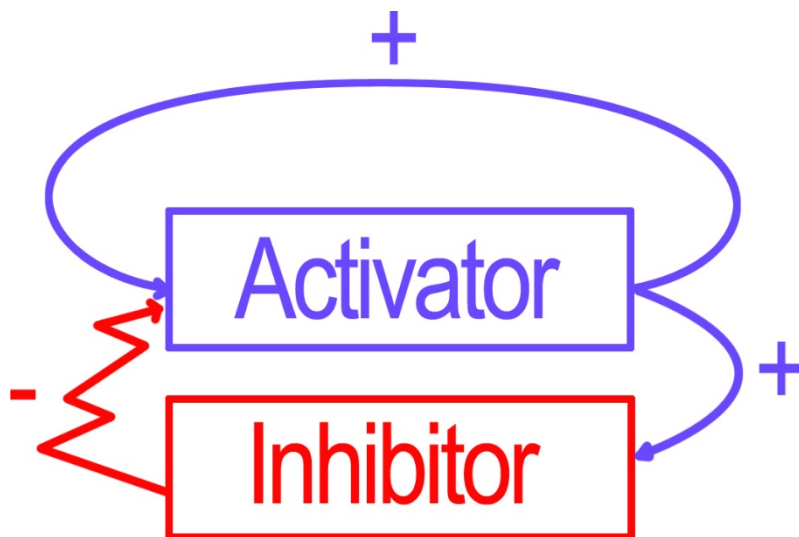


Figure 1.5. The Activator-Inhibitor mechanism.

If an autocatalytic activator is joined by an inhibitor, which in turn suppresses the autocatalysis (Figure 1.5), it is possible to achieve dot and stripe patterns, which are called Turing patterns. The autocatalytic reaction of the activator creates a local ‘hot spot’ while the existence of the inhibitor, which diffuses faster, can prevent the ‘hot spot’ from spreading. Both the dot and stripe patterns have the same size and spacing; however, the stripe pattern is less common and tends to break into the dot pattern. The difference between these two patterns is the production rate of activators and inhibitors.¹²

A crucial prerequisite for the Turing pattern to occur is that the inhibitor has to diffuse faster than the activator, which is rarely the case. This explains why it took 40 years to reproduce Turing patterns (Figure 1.6¹³) in chemical systems.^{14,15}

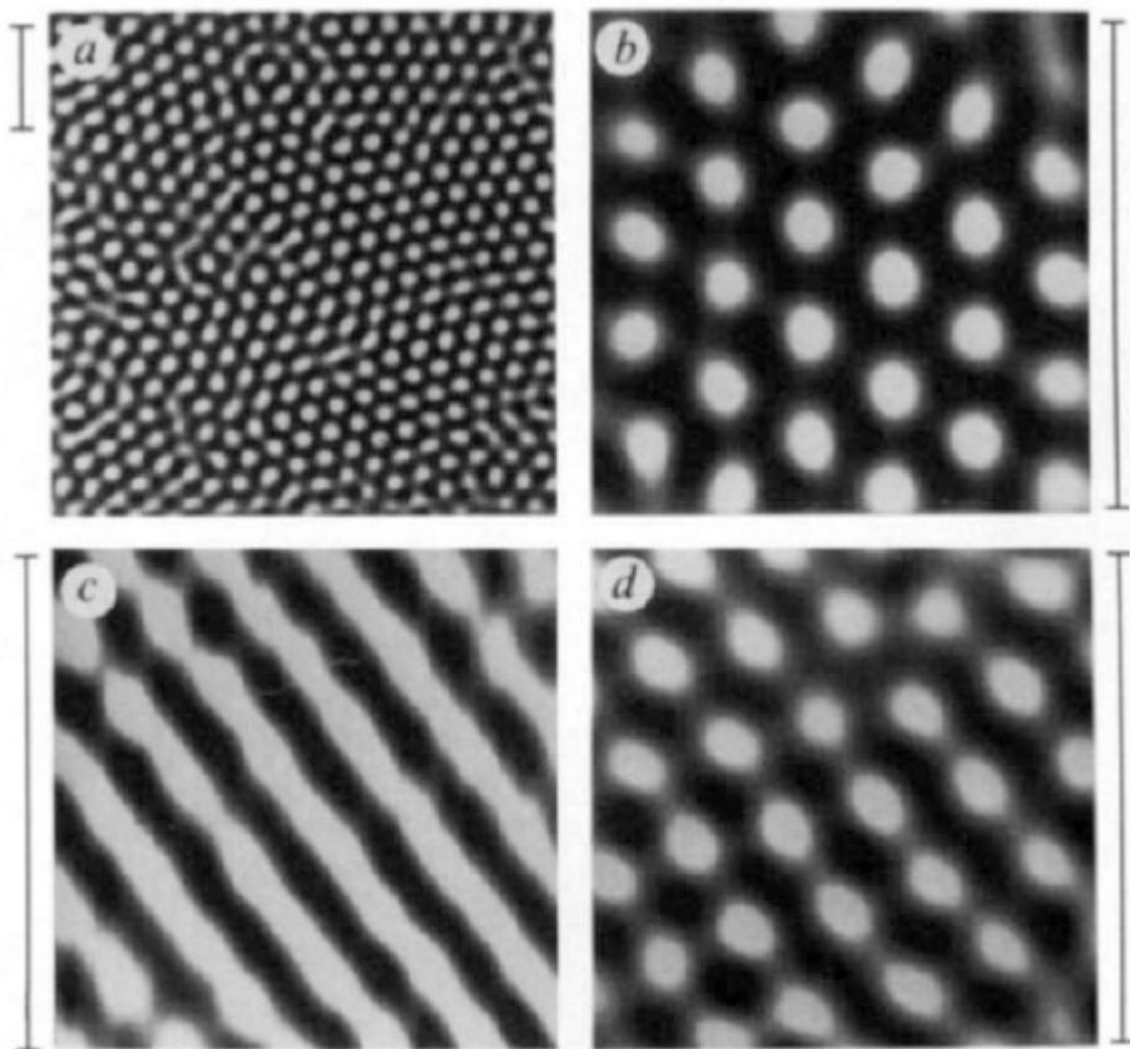


Figure 1.6. The formation of Turing pattern: (a) stationary patterns, (b) spots, (c) stripes, and (d) transition of stripes into spots, in a reactor mixed with $\text{CH}_2(\text{COOH})_2$, NaOH , Na_2SO_4 , H_2SO_4 and ClO_2^- . (Reprinted by permission from Macmillan Publishers Ltd: *Nature*, Ref ¹³, copyright 1991)

It is worth pointing out that the propagating concentration wave in Figure 1.4 is not a stationary Turing pattern, because there is no inhibitor involvement, but the concentration wave pattern still belongs to the reaction-diffusion patterns.

Turing patterns have been used to explain the formation of sand ripples and the pattern formation in developmental biologies^{16–20}, animal communities³ and the social sciences.²¹

1.1.3. SUMMARY

The pattern formation systems described above, either convective or reaction-diffusion, have these properties in common: thermodynamically open, far from equilibrium, and nonlinear. I. Prigogine²², the 1977 Nobel Prize laureate, called these systems *dissipative structures*, because such patterns are maintained by energy dissipation. The corresponding patterns, formed in these dissipative systems, are called *self-organization*. *Self-organized* patterns are fundamentally different from *self-assembly* patterns.^{23,24} Table 1.1 compares them.

Table 1.1. The comparison of self-assembly patterning and dissipative patterning.

Self-assembly Patterning²³	Self-organizing Patterning²⁵
◆ Near equilibrium	◆ Far from equilibrium
◆ Towards local minimum of free energy	◆ Driven by energy dissipation
◆ Pattern formation mechanism is linear	◆ Pattern formation mechanism is nonlinear
◆ Stops when minimum energy is achieved	◆ Stops when driving force disappears
◆ Pattern is permanent	◆ Pattern may disappear with the removal of the driving force
◆ Pattern is stationary	◆ Pattern may evolve over time
◆ Driving force determined by depth of valley in energy map	◆ Driving force determined by speed of energy dissipation
◆ Length scale determined by size of building blocks	◆ Length scale determined by interaction of building blocks
◆ Boundary conditions have no impact on the pattern	◆ Boundary conditions have crucial impact on the pattern
◆ Length scale typically from micrometer to angstrom	◆ Length scale typically from kilometer to micrometer
◆ Examples: DNA Surface reconstructions, <i>etc.</i>	◆ Examples: Convection: cloud Reaction-diffusion: BZ, <i>etc.</i>

Since the formation of self-organized pattern is more dependent on the delicate interplay of building blocks, the window for self-organized patterns to occur is extremely narrow. Outside this window is usually dominated by random chaos or a perfect symmetry, *e.g.* a flat surface.

Electrochemical cells are not acknowledged as a nonlinear system until recent advancement in knowledge²⁶, however oscillations in electrochemical experiments date back to 1828.²⁷ Soon after that, periodic oscillation was reported during the electrodisolution of iron.²⁸ It was not until 1996 that Koper provided a better understanding about the electrochemical oscillations, which are linked to the changing potentials.²⁶ Recently, self-organized Turing patterns are observed *in-situ* during electrochemical experiments.²⁹

1.2. PATTERN FORMATION IN ELECTROCHEMICAL SYSTEMS

The electrochemical cell is a great system for studying the *self-organized* pattern formation, because the reaction on the electrode can be coupled with diffusion, migration, and/or convection within the electrolyte.³⁰

1.2.1. THE ELECTROCHEMICAL SYSTEM

1.2.1.1. THE ELECTROLYTE/ELECTRODE INTERFACE

When an electrode is immersed into an electrolyte, an interface is created (Figure 1.7).³¹ Charges are transferred by electrons in the electrode and by the movement of ions in the electrolyte. The transfer of charges across the interface is accomplished by the redox reaction of the electrode or electrolyte ions (Figure 1.7).

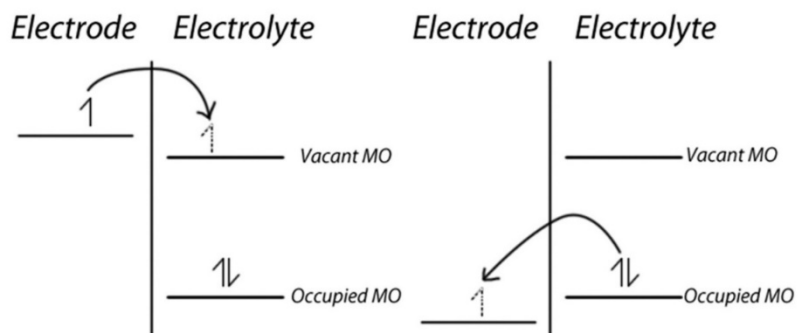


Figure 1.7. Charge transfer at the electrode/electrolyte interface

The electrolyte/electrode interface itself cannot be studied alone. It must be connected to another half-reaction to form an electrochemical cell. Most of the time, one's interest is only on one of the electrodes, the working electrode (WE). To this end, an inert electrode, much larger than the working electrode, is chosen as the counter electrode (CE) to minimize the interference from the CE.

Since it is difficult to measure the potential drop (loss) across the bulk electrolyte, a reference electrode (RE) *e.g.* standard hydrogen electrode (SHE) or saturated calomel electrode (SCE) is normally placed next to the WE to monitor the potential on the WE. Since the potential of the standard electrode is known and fixed, the potential on the WE can be measured by altering the external potential between these two electrodes to achieve a virtually zero current.

The electrolyte/electrode interface can be simply modeled as a leaky capacitor. The charge on the electrode is equal to the total charge within the electrolyte. Areas that hold these electrons, charged ions, and oriented dipoles are called the double layer.

1.2.1.2. THE DOUBLE LAYER

The double layer in the electrolyte can be further divided into several layers (Figure 1.8). The layer adjacent to the electrode, made up of solvent molecules and specifically adsorbed ions, is called the *inner* or *Helmholtz* or *Stern* layer. The next layer consists of non-specifically adsorbed solvated ions, which carry an opposite charge of the specifically adsorbed ions. The inner Helmholtz plane (IHP) separates itself from the electrode by the radius of specifically adsorbed ions. The outer Helmholtz plane (OHP) is determined by the distance from the center of non-specifically adsorbed ions to the electrode. The space beyond OHP is called diffuse layer which extends into the bulk solution.

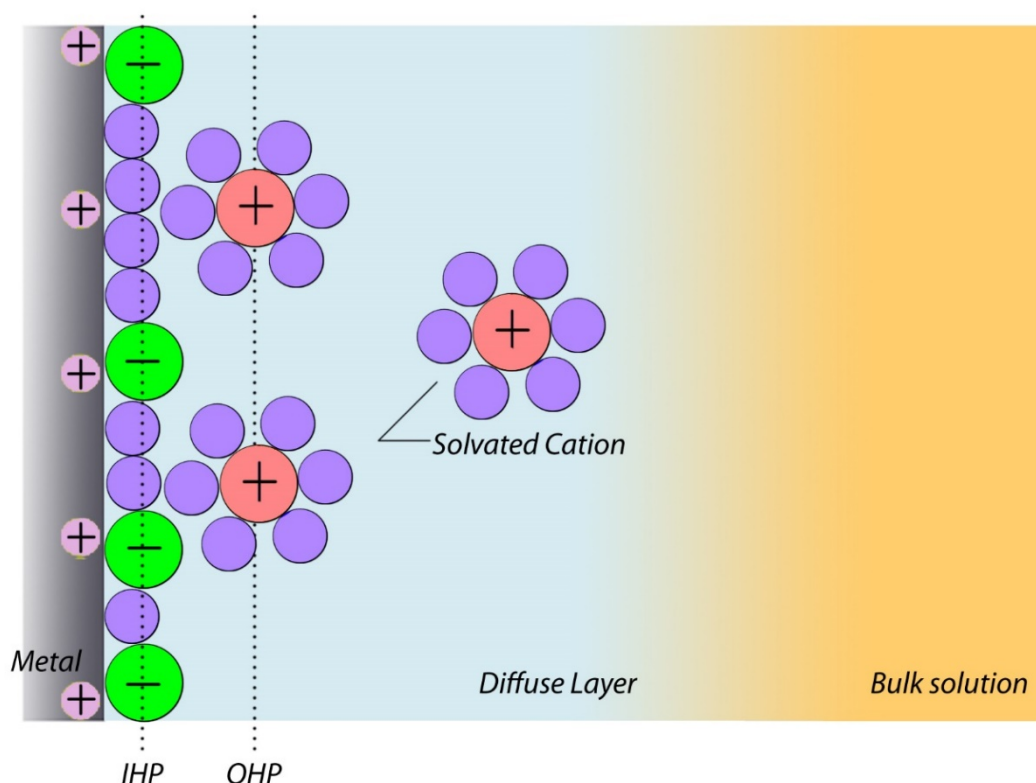


Figure 1.8. Double layer model. NB: the charge on the electrode in this figure is positive and the charge in the electrolyte is negative in this case.

The continuous reaction at the electrode/electrolyte interface may cause a surplus or deficit of ions within the diffuse layer, thus creating an ion-concentration gradient.

1.2.1.3. MASS TRANSPORT

To counterbalance this ion-concentration gradient, ions are carried across the diffuse layer *via* diffusion, migration, and convection, the total of which is called mass transport of ions³¹ (Figure 1.9).

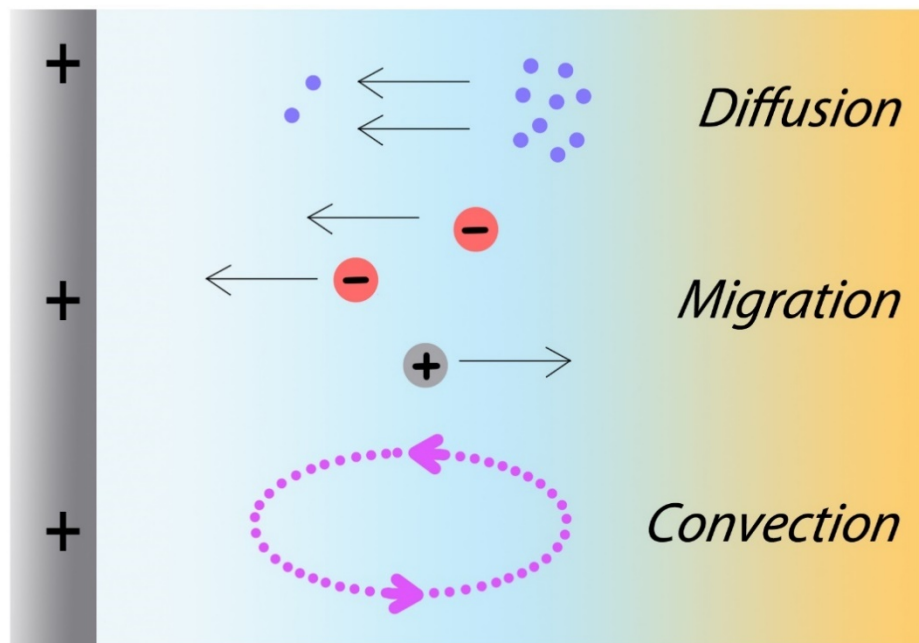


Figure 1.9. Mass transport of ions across the diffuse layer: diffusion, migration and convection.

Diffusion is the movement of a species in accordance with the concentration gradient – *i.e.* from high concentration to low concentration; migration is the movement of a charged species in line with the electric field; convection describes the hydrodynamic movement of a fluid, which takes species within it to move in the same direction (Figure 1.9).

The mathematical treatment for each term is given by the *Nernst-Planck* equation (Equation 1.1). On the right side of Equation 1.1, the first term denotes diffusion, the second represents migration, and the third stands for convection

$$J(x) = -D \frac{\partial C(x)}{\partial x} - \frac{zF}{RT} DC \frac{\partial \phi(x)}{\partial x} + Cv(x) \quad (\text{Equation 1.1})$$

, where $J(x)$ is the flux of species at distance x from the surface, D the diffusion coefficient, $\partial C / \partial x$ the concentration gradient at distance x , $\partial \phi / \partial x$ the potential gradient, z the charge of species, C the concentration of species, and v the convective move velocity towards the electrode.

Various kinds of oscillations and pattern formation in the electrochemical systems can be traced back to the convection and/or reaction-diffusion of ions, which are summarised below. In accordance with introduction in 1.1, convective electrochemical patterns will be reviewed first, followed by reaction-diffusion type patterns.

1.2.2. ELECTROCHEMICAL PATTERN FORMATION DUE TO CONVECTION

In normal electrochemical experiments, high concentrations of reactants and low over-potentials are used to ensure the efficiency of the electrochemical reaction.³² This can cause the formation of gravitational convective cells within the bulk solution, because a significant density gradient is created from the electrode to the bulk solution.

The instability of this electrochemical system is determined by a modified Rayleigh number for the electrochemical systems, R ³³

$$R = \frac{g\beta(\frac{\delta\rho}{\delta c})d^4}{\rho D\nu} \text{ (Equation 1.2)}$$

, g is the gravity acceleration, β the concentration gradient, c the concentration of the electrolyte, d the distance between the electrodes, ρ the density, D the effective diffusion coefficient, and ν the coefficient of kinematic viscosity.

The calculated critical R value (R_c) for convections in copper sulphate is 1707, while the experimental value is 1130 ± 210 .³³

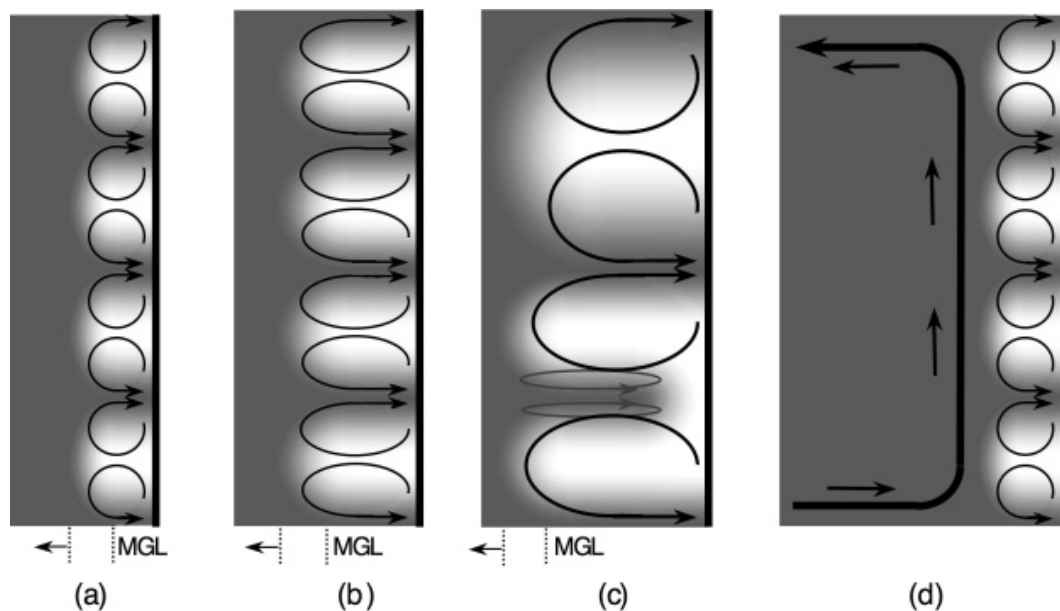


Figure 1.10. Unstable convective cells. Convection can occur where convection cells form, grow, break, merge, and reform at the surface, as the moving gradient layer moves farther from the electrode. (Reprinted by permission from American Chemical Society: *J. Phys. Chem. C*, Ref³⁵, copyright 2007)

In a smaller scale, the electrochemical convection within the micrometer-thick ion-depletion layer has been modeled (Figure 1.10).³⁴ If the current through the electrochemical cell is much higher than the diffusion-limited current, diffusion alone can

no longer keep up with the chemical reaction on the electrode. (Recall the oil pan!) As a result, convective cells start to form within a space next to the electrode (called ion depletion layer in this case) to assist the mass transport of ions (Figure 1.10a).³⁵ As these convective cells use up the ions next to the electrode, they start to grow larger (Figure 1.10b). However, large convective cells are not stable, they tend to rearrange themselves by breaking, merging, and growing new cells (Figure 1.10c). Some of these cells may grow so large that they are no longer close to the electrode surface. Instead, these large convective cells are in charge of bringing ions from the bulk solution to the end of small convective cells (Figure 1.10d). The size of the small convective cells discussed above is on the same scale as the thickness of the ion-depletion layer.

These convective cells were made visible by Dini³⁶ (Figure 1.11) and Orlik³⁷ in a forced convection electrochemical system bounded by two electrodes, which are kept at 60 μm apart. The luminescence photon signal comes from 9, 10-diphenylanthracene* (DPA*), which is created by the collision of a radical cation DPA^+ (formed at the anode) and a radical anion DPA^- (formed at the cathode). DPA^- is carried by convection from the cathode to the anode. Convective cells are observed on the transparent cathode^{38,39}.

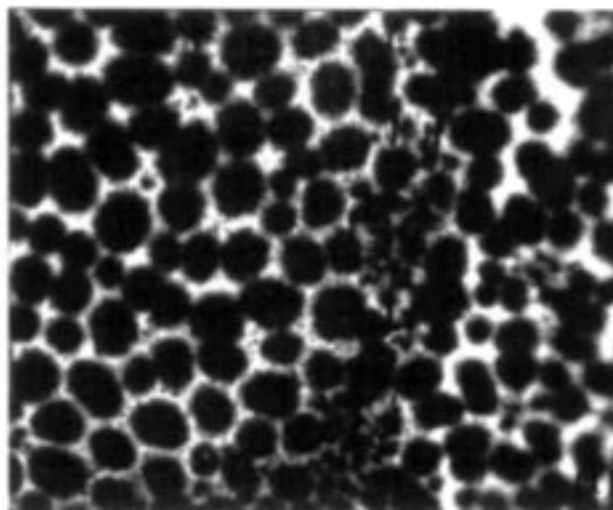


Figure 1.11. Evolution of the luminescent pattern on ITO electrode due to convection within ion depletion layer. The size of the image is 2.4 x 3 mm². (Reprinted by permission from PCCP Owner Societies: *Phys. Chem. Chem. Phys.*, Ref. ³⁶, copyright 2000)

1.2.3. ELECTROCHEMICAL PATTERN FORMATION DUE TO REACTION-DIFFUSION

The first report of electrochemical oscillations dates back to 1828,²⁷ which was followed by Joule⁴⁰ in 1844. Joule was also the first person to link these oscillations to pattern formation.⁴⁰ Ostwald systematically studied the periodic oscillation during the electrochemical dissolution of chromium in acids.⁴¹

A groundbreaking advancement in this field is the introduction of nonlinearity into the electrochemical systems⁴², which is followed by myriad attempts on explaining and modelling the electrochemical oscillations, either random⁴⁸ or periodic.⁴³⁻⁵²

Oscillations can lead to the formation of patterns in electrochemical systems.^{26,53,54} A general model for this pattern formation is provided by K. Krischer *et al.*⁵⁵ In the light of this, Turing pattern is achieved in the electrochemical system.^{29, 58}

Patterns discussed above could form on an electro-catalytic electrode or an active electrode.^{39,56} The electro-catalytic (passive) electrode only acts as a site for electron transfer; it isn't involved in the chemical reaction. On the contrary, the active electrode participates in the chemical reaction, either by electrochemical dissolution or electrodeposition.

The pattern formed on the electro-catalytic electrode will disappear, once the driving force is removed. (*Cf. self-organized* pattern in Table 1.1) However, the pattern on the active electrode, obtained *via* deposition or dissolution, is permanent.

If the size of the electrochemical pattern is on the nanometer scale, it could be of additional interest and application potential in the booming nanotechnology.

1.3. NANOPATTERN FORMATION IN ELECTROCHEMICAL SYSTEMS

“There’s Plenty of Room at the Bottom” – Richard Feynman⁵⁷

If the minimum dimension of the pattern falls within the nanometer range, this pattern is defined as a nanopattern.⁵⁸ Materials with nanopatterns at the surface are of great interest in scientific research as well as in engineering applications, because these materials could exhibit novel and distinct properties.⁵⁹ To name a few, bulk silicon is colourless because of the relatively large band gap; however, nanoporous silicon can emit red light due to the quantum size effect⁶⁰; biomedical alloys with nanoscale features can substantially improve cells' affinity, and thus improve the quality of implantation⁶¹.

Different kinds of methods have been developed for nanopatterning; however, they are either expensive or time-consuming or limited by the spatial resolution.⁶² The electrochemical method offers a cheap and time-efficient alternative for nanopatterning.

To date, the most extensively studied and widely used electrochemical nanopattern is porous anodic alumina (PAA).

1.3.1. NANOPATTERN FORMATION DURING ANODIZATION

1.3.1.1. POROUS ANODIC ALUMINA (PAA)

Self-organized hexagonally-close-packed pore arrays (Figure 1.12)^{63,64} have been obtained on anodic alumina *via* anodization.^{65,66,67} The interpore spacing, which is dependent on the applied voltage, ranges from 60 nm to 420 nm.⁶⁸ It has been found that the volume expansion factor, a ratio of the thickness of the anodic oxide over that of the dissolved metal layer, is between 0.8 for 1.7 for the pattern to occur. The most ordered pattern is achieved at a ratio of 1.4.⁶⁸ PAA is extensively used as templates for other nanofabrications⁶⁹.

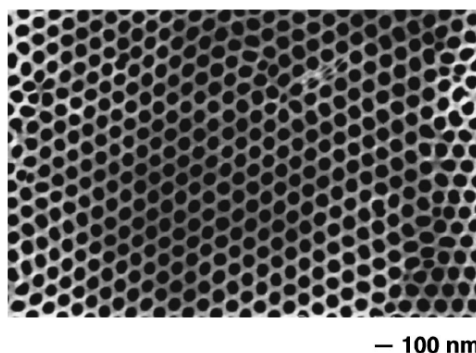


Figure 1.12. Formation of porous anodic alumina with hexagonally-close-packed nanopores. (Reprinted by permission from AIP Publishing LLC: *Appl. Phys. Lett.*, Ref. ⁷⁰, Copyright 1998.)

1.3.1.2. OXIDE NANOTUBES

The formation of tubular oxide during anodization has been reported on Al⁶⁹, Ti^{71,72,73}, Ta (Figure 1.13)^{74,75,76}, V⁷⁷, and alloys.⁷⁸ These nanotubes exhibit the same hexagonally-close-packed order as PAA, however, each nanotube is well separated from other nanotubes.

These nanotubes have found their applications in biomedical implantation⁷⁹, water photoelectrolysis⁸⁰, supercapacitors⁸¹, and nanofabrication.⁸²

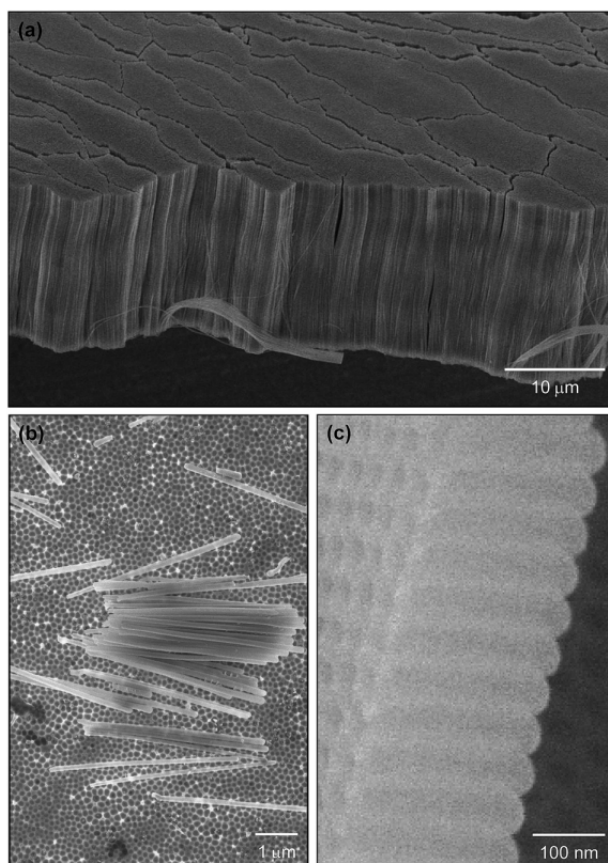


Figure 1.13. Large scale (a) and zoom-in (b, c) SEM images of nanotube formation on tantalum. (Reprinted by permission from The Royal Society of Chemistry: *J. Mater. Chem.*, Ref ⁷⁶, Copyright 2009.)

1.3.1.3. FORMATION MECHANISM

The forming mechanisms for PAA and nanotubes are still controversial.^{71,83}

Various models have been proposed, which are summarized below:

1.3.1.3.1. Oxide flow model

Hebert⁸⁴ shows that anodic metal ions (e.g. Al^{3+} , Ti^{4+}) react with O^{2-} at the Metal/Oxide interface to form corresponding oxides. Under high pressure, the freshly formed oxide behaves as a fluid and is being pushed away from the Metal/Oxide interface (as indicated by arrows in Figure 1.14).⁸⁵ As a result, the wall of the nanopore grows higher. During the same process, the interaction with neighboring nanopores creates the hexagonally-closed-packed ordering.

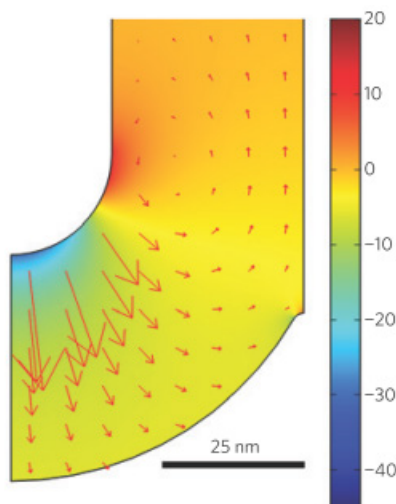


Figure 1.14. The velocity vectors (red arrows) of oxide flow during the formation of the oxide nanopores or nanotubes (colour scale is stress). (Adapted by permission from Macmillan Publishers Ltd: *Nat. Mater.*, Ref ⁸⁴, Copyright 2009.)

1.3.1.3.2. Nanobubble

Y.-L. Wang⁸⁶ demonstrates that nanobubbling can occur on the anode during anodization. After anodizing in NaOH with a particular concentration, an arrangement similar to the hexagonally-close-packed pattern is achieved on tungsten. Cross-sectional SEM (Figure 1.15) confirms the formation of nanobubbles between the metal and the oxide layer.

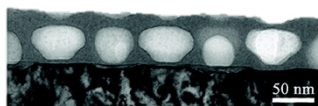


Figure 1.15. The formation of the nanobubbles during the anodization of W in NaOH. (Adapted by permission from American Chemical Society: *J. Phys. Chem. C*, *Ref*⁸⁶, copyright 2011).

1.3.1.3.3. Oxygen bubble mould effect (OBME)

Combining the oxide flow model and the nanobubble model, X. Zhu^{87,88} provides a theoretical background to the nanobubble formation and argues that the total anodic current can be split into two parts: ionic current (forming anodic oxide) and electronic current (forming oxygen bubbles). These oxygen bubbles sit at the bottom of pores, as in Figure 1.15.

1.3.1.3.4. Field-assisted dissolution model

Field-assisted dissolution model suggests that a thin layer of anodic oxide, formed at the start of anodization, is the starting material for the nanopore growth.^{89,90} Due to local defects, where the dissolving speed is slightly higher, shallow pores are created on the anodic oxide (Figure 1.16). During this process, H^+ is generated at the bottom of pores

(Equation 1.3), which will bind with F^- to produce more HF, and HF keeps dissolving the anodic oxide. As a result, pores are etched deeper and deeper.

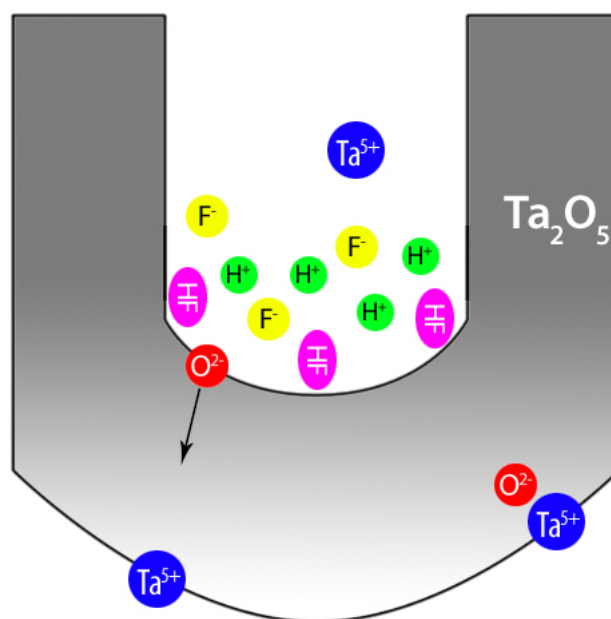
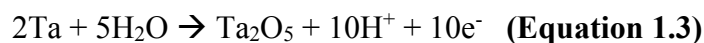


Figure 1.16. Chemical reactions at the base of a pore during pore formation.

However, this model fails short in explaining the origin of the hexagonal order of nanopores.

Other researchers⁹¹ have shown that the formation of nanotubes depends on the HF concentration in the electrolyte⁸³ and the total anodization time.⁹¹ These nanotubes may detach off the surface, exposing the metallic pattern beneath it.⁹¹

The models discussed above assume that the pattern originates within the oxide, the models to be introduced below suggest that the pattern forms within the electrolyte.

1.3.2. NANOPATTERN FORMATION DURING ELECTROPOLISHING

1.3.2.1. NANOPATTERNS ON AL DURING ELECTROPOLISHING AND THE ADSORPTION MODEL

Different kinds of nanopatterns (stripes^{92,93} and dots⁹⁴) have been reported on aluminium after electropolishing in a commercial electrolyte (Figure 1.17).^{95,96} The transitions between stripes and dots are controlled by the electropolishing potential and time.⁹⁷

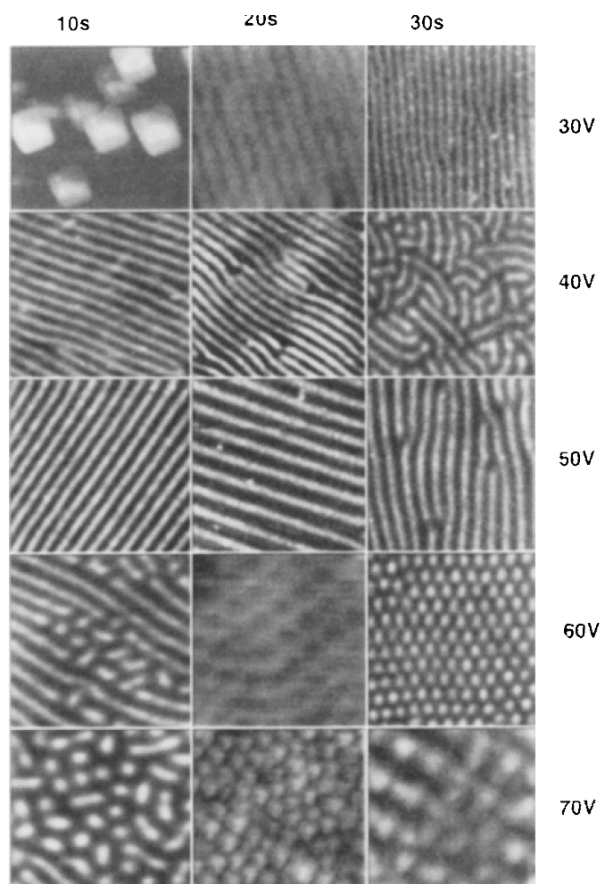


Figure 1.17. Different kinds of patterns formed on aluminum *via* electropolishing at different potentials and time intervals. (Reprinted by permission from Springer: *J. Electron. Mater.*, Ref ⁹⁴, copyright 1996)

The pattern originates within the double layer and is driven by the potential drop within the layer. Using the Poisson equation and long-wavelength expansion, Chang

shows that the electric field is higher at the protruding (maximum) part than the receding (minimum) part. A higher electric field means a higher adsorption rate of polar molecules, a condition which can in turn shield the electrode beneath it from further dissolution, thus creating and preserving the pattern (Figure 1.18).

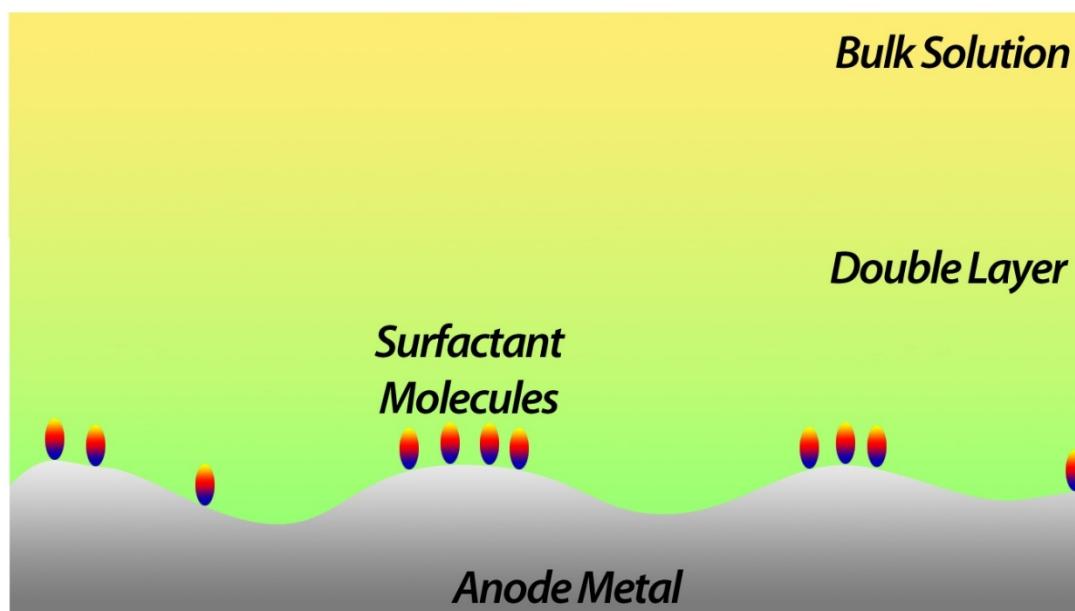


Figure 1.18. The surfactant molecules in the electric double layer shields the electrode surface and form a pattern.

Chang⁹⁷ *et al.* postulates that these surfactant molecules could be the organic molecules in the electrolyte, though he does not exclude the possibility of solvated ions. The simulations from this model matched well with the experimental data. The same model has also been used to explain the pattern formation on aluminum electropolished in different electrolytes.⁹⁸

1.3.2.2. CRYSTAL ORIENTATION MODEL

Under certain circumstances, the pattern formation on electropolished aluminum depends on crystal orientation.⁹⁹ Different kinds of patterns have been observed on Al(100) and Al(111). This observation still complies with the adsorption model, if assuming that different crystal orientations have different molecule adsorptivity.⁹⁹

Johnson¹⁰⁰ replaced the electric energy in Chang's simulation with interfacial energy and showed that different patterns could exist on different crystal orientations during anisotropic etching.¹⁰¹

However, Basumallick⁹³ argues that the nanopattern formation on aluminum is due to the relaxation and reconstruction of the newly exposed surface. According to his DFT calculations, Basumallick predicts that different dissolving speeds are present at different crystal orientations. He further argues that after the dissolution of the top layer, atoms in the newly formed layer could have a chance to relax from their previous locations and minimize the overall surface energy. This relaxation causes the surface atoms to be displaced, thus forming patterns. Since the dissolving speed varies on different orientations, the displacement amplitude is also different, thus creating different kinds of patterns.

Electropolishing is assumed to be isotropic, as a result, patterns achieved *via* electropolishing should be uniform on all orientations. Patterns, subject to crystal orientations, are products of anisotropic etching.

1.3.2.3. NANOPATTERN (DIMPLE) ON TA, TI, W AND ZR AND THE CONVECTIVE MODEL

Previous work in our group has shown the formation of dimples on tantalum during electropolishing.^{102,103} After that, similar patterns have been found on titanium, tungsten, and zirconium⁶² (Figure 1.19).

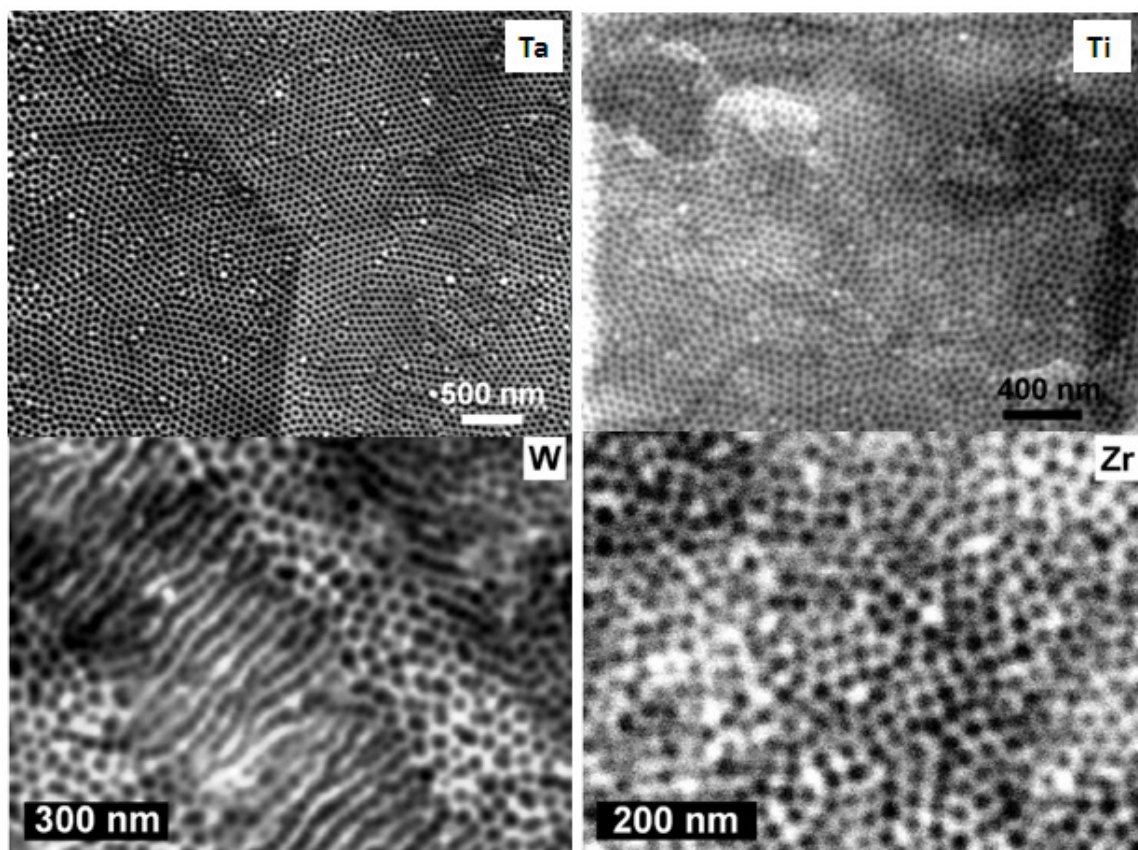


Figure 1.19. SEM images of the dimple pattern formed on tantalum, titanium, tungsten, and zirconium. (Reprinted by permission from American Chemical Society: *ACS Nano*, Ref ⁶², copyright 2008).

Arranged in highly ordered arrays, dimples are tens of nanometers in diameter and six to ten nanometers in depth. The morphology of dimples on each metal and fabricating conditions are summarized in Table 1.2.

Table 1.2 Summary of dimple morphologies on different metals and fabrication conditions.

Metal	Ta⁶²	Ti⁶²	W⁶²	Zr⁶²	Al^{97,104}	Steel^{105,106}
Depth /nm	10	3	6	n/a	2	10
Periodicity/ nm	55-60	55-60	55-60	40-45	50-70	90
Potential /V	15	15	15	20	20	~60
Electrolyte	98% H ₂ SO ₄ 48% HF 9:1 v/v	98% H ₂ SO ₄ 48% HF 8:2 v/v	98% H ₂ SO ₄ 48% HF 93:7 v/v	0.5M NH ₄ F	HClO ₄ Ethanol 1:4	HClO ₄ Monobutylether 1:9

A model, based on convection, has been proposed to explain the formation of dimples (Figure 1.20).⁶² During electropolishing, the electrochemical double layer is broken into convective cells to assist the mass transport of ions (*Cf.* 1.2.2 Convection in the ion depletion layer). These convective cells will bring fresh solutions to the electrode surface, where the etching speed is slightly higher, thus creating a pattern.

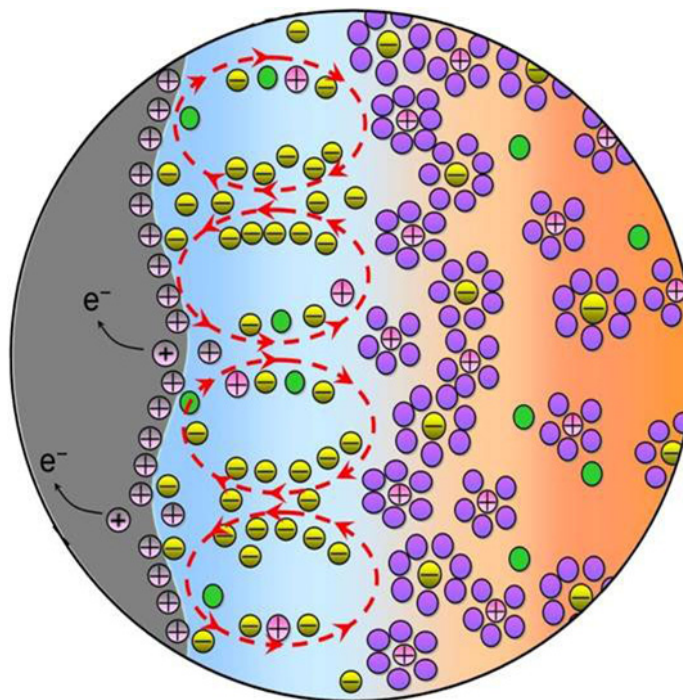


Figure 1.20. The formation of convective cells within the double layer during electropolishing, which leads to the dimple pattern on the working electrode surface. (Reprinted by permission from American Chemical Society: *ACS Nano*, Ref ⁶², copyright 2008).

1.4. OVERVIEW OF THIS THESIS

This thesis is on (a) a continuing search of patterns formed *via* electropolishing. The electrochemical method has emerged as an indispensable tool for nanofabrication. The formation of dimples on tantalum, titanium, tungsten, and zirconium indicates that the electrochemical pattern formation is a universal process. It opens the door to generate an ordered nanopattern on more metals *via* electropolishing under optimized conditions. As a result, this thesis explores the formation of dimples on various metals, together with different kinds of nanopatterns and nanotubes.

(b) The intriguing formation of various kinds of nanopatterns and nanotubes leads to a full-scale investigation into all the parameters that control the pattern formation,

pattern transition and pattern evolution, towards a deeper understanding of the pattern formation mechanism.

(c) One of the potential applications of the dimple pattern is demonstrated by extending dimples onto a biomedical alloy, which could be of great interest in biomedical implantation.

(d) Given the fact that the electrochemical nanopattern formation is a universal process, attempts have been made to nanopattern silicon, a semiconductor, *via* electropolishing.

1.5. STRUCTURE OF THIS THESIS

Detailed outlines of this thesis are as follows: the next chapter (Chapter 2) will be on the electrochemical setup, followed by a summary of the experimental methods, such as potentiostatic and galvanostatic.

Characterization techniques used throughout this thesis (*e.g.* AFM, SEM, and PEEM) will be explained in Chapter 3 with a brief description of basic principles and a discussion of optimizing conditions, based on thesis author's hands-on experience, to obtain best quality images.

Chapter 4 is a systematic study of the pattern formation on vanadium. Different kinds of patterns (pimple, labyrinth, and dimple pattern) have been discovered on electropolished vanadium. The formation of each nanopattern is subject to the electrolyte composition, electropolishing potential and time. Electrolyte composition is systematically varied and a phase diagram is plotted to visualize electrolyte's impact on

the pattern transition. Electropolishing potential alters the periodicity of each pattern. A pattern evolution (from pimples to labyrinths to dimples) is observed on electropolished samples. These new findings will be discussed in the context of existing models on pattern formation.

Different kinds of patterns have been achieved on tantalum during electropolishing, which are discussed in Chapter 5. Besides that, the pattern formation on tantalum also includes nanotubes. A phase diagram is plotted to demonstrate water and HF's impact on the nanotube formation. What's more, the effect of electropolishing parameters, *e.g.* current density and electropolishing time, are studied as well with respect to the morphology of dimples.

The application of the dimple pattern on a biomedical alloy is presented in Chapter 6. Cells are sensitive to mesoscale, microscale, and nanoscale structures on implant surfaces. As a result, novel materials with surface features at these scales have shown to improve cell adhesion, proliferation and differentiation. In this chapter, the dimple pattern, previously found on Ta, Ti, W, Zr, and V, is reproduced on the biomedical alloy (Ti-6Al-4V). Besides that, it is found that the size of dimples on this alloy is subject to the electropolishing potential, electrolyte concentration and surface chemical composition. This gives us more opportunities to tailor the surface features to better accommodate cells.

Chapter 7 is an attempt at expanding dimples onto silicon, a semi-conductor. A series of electrolytes have been tested for nanopatterning silicon *via* electropolishing.

Porous silicon is achieved after electropolishing in $\text{H}_2\text{SO}_4/\text{HF}$ solution. Electropolishing silicon in diluted HF solution creates a ‘fence’ structure. The most promising results are achieved when electropolishing is carried out in acetic acid/HF and ethylene glycol/HF electrolytes.

Finally, results of this thesis are summarized in Chapter 8 with a view on future work.

CHAPTER -2

OVERVIEW OF EXPERIMENTS

2.1. EXPERIMENTAL SETUP

Electropolishing/anodizing can be carried out in a two-electrode system (Figure 2.1) with the omission of a reference electrode (*Cf.* 1.2.1). The disadvantage of this setup is that the information on the potential difference between the working electrode and the reference electrode is missing, because the potential drop across the electrolyte is unknown. The potential drop (loss) within the electrolyte is extremely high, given the high viscosity and low conductivity of the electrolyte.³¹

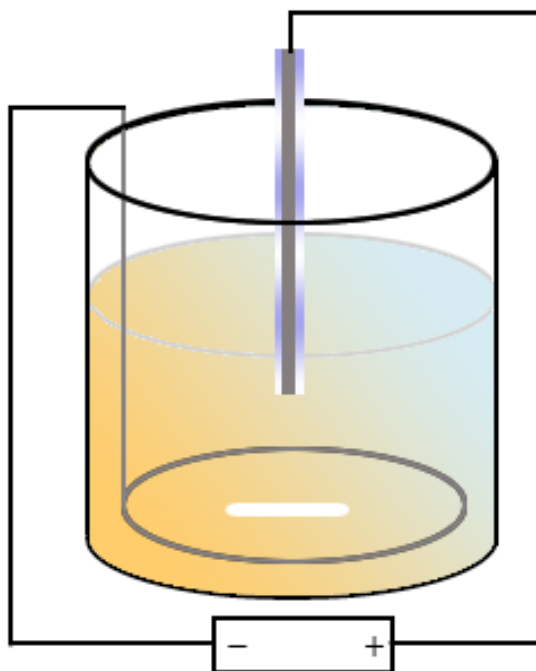


Figure 2.1. Scheme of a typical electropolishing cell

The anode, the working electrode, is the metal/semiconductor to be electropolished or anodized. Normally, an inert metal electrode (*e.g.* Pt/Ir) is chosen as the cathode for conducting purpose. Both electrodes are immersed in the electrolyte with a potential applied for a certain amount of time.

Upon turning on the power supply, H^+ gains an electron at the cathode and evolves as hydrogen gas. The anode metal is oxidized and forms *anodic oxide* with O^{2-} at the metal/metal oxide interface.¹⁰⁷ In the meantime, anodic oxide can be dissolved by etchants in the electrolyte, if present.¹⁰⁸

At the end of this electrochemical treatment, if the resulting anodic oxide is thicker than the *native oxide*, this process is defined as anodization; otherwise, it is called electropolishing. Electropolishing has been extensively used to remove surface abrasions on various metals and producing STM tips¹⁰⁹ and Atom Probe Microscope tips.¹¹⁰

2.2. ELECTROPOLISHING

The American Society for Testing and Materials (ASTM) defines electropolishing as the smoothening of the working electrode surface by making it anodic in a suitable electrolyte.¹¹¹ Two levels of flattening can be achieved *via* electropolishing: *macrosmoothing*, which removes surface roughness larger than one micrometer and *microsmoothing*, which eliminates surface roughness smaller than one micrometer.

2.2.1. MACROSMOOTHING

During electropolishing, the current density is unevenly distributed on the working electrode (Figure 2.2). The current density is higher at the protruding part, which

is closer to the cathode, than the receding part. As a result, the dissolving speed is higher at the peak than the valley¹¹², thus removing the surface roughness, which is larger than one micrometer¹¹³.



Figure 2.2. Macrosmoothing. The current density is higher at the protruding part than the receding part. As a result, the protruding part gets etched more, which levels the electrode surface.

2.2.2. MICROSMOOTHING

Microsmoothing can only be achieved under mass-transport-limit condition.¹¹⁴

There are three hypotheses regarding the species, which is mass transport limited, during microsmoothing¹¹⁴:

Hypothesis 1¹¹⁵ (Figure 2.3a): during electropolishing, the anode metal is continuously being oxidized and dissolved into the electrolyte. Since electropolishing is carried out in concentrated acids, the mass transport of dissolved ions is greatly hindered by the viscous electrolyte; thus, an ion concentration gradient is formed adjacent to the anode.¹¹⁶ Due to its viscous nature, some researchers have named this layer as *viscous layer*^{117,118} or *salt film*.¹¹⁹ The existence of this layer is linked to the removal of micro-

scale roughness on the surface.¹¹³ After the establishment of the concentration gradient, further mass transport of ions across the viscous layer is hindered.

Hypothesis 2 (Figure 2.3b) proposes that the acceptor anion is used up at the electrode surface, which leads to the limiting mass transport of anions.^{120, 121}

Hypothesis 3 (Figure 2.3c) suggests that the water molecules, used to form the anodic oxide, are used up at the electrode and further mass transport of water is the limiting step.¹²²

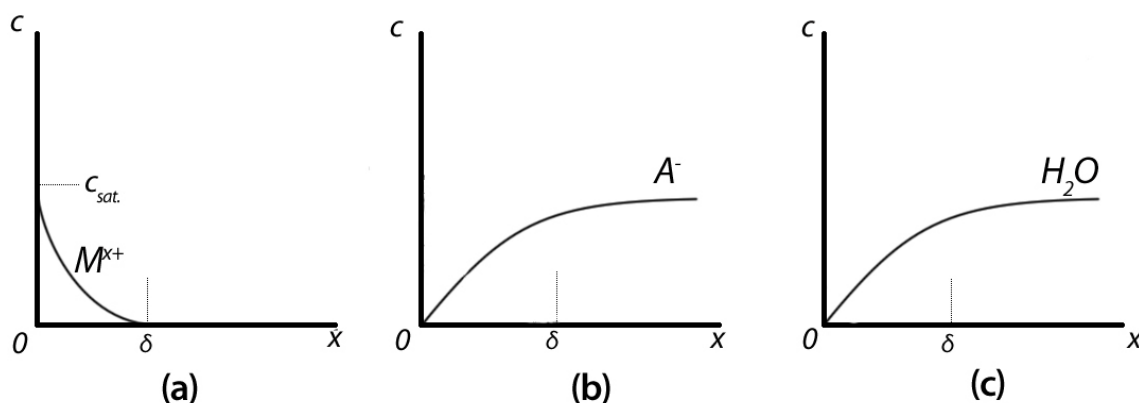


Figure 2.3. Proposed mass transport limiting species: dissolved ions (a), acceptor anion (b), and water (c).

Numerous experimental results¹²³⁻¹³⁰ have shown support for hypothesis 1: during electropolishing, the ion concentration is saturated at the electrode, and a concentration gradient is established within the viscous layer. Further mass transport of dissolved ions through this viscous layer determines the rate of electropolishing, which appears as limiting current in the i - t curve, as discussed below.

2.3. TYPES OF TECHNIQUES

The electrochemical system can be regarded as a ‘black box’ (Figure 2.4). By alternating ‘Input probes’, different ‘Output’ signals are produced, which shall give us a clue about the electrochemical process inside the box.

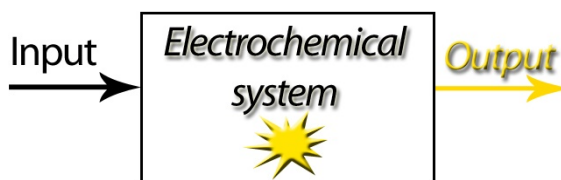


Figure 2.4. Probing the electrochemical system.

‘Input probes’ can be a constant potential signal or a constant current signal or a linear sweep of potential. Corresponding techniques are called chronoamperometry, chronopotentiometry and linear sweep voltammetry, respectively. The output signal could be an electrochemical signal (*e.g.* current in chronoamperometry) or nanopatterns in a pattern formation system.

2.3.1. CHRONOAMPEROMETRY

In chronoamperometry, a constant potential (potentiostatic, Figure 2.5a) is applied on the anode, meanwhile the current is recorded as a function of time, which is called the *i*-*t* curve.

Upon the setup of the electrochemical cell (t_l in Figure 2.5c), the initial spike in the *i*-*t* curve is caused by the charge up of the double-layer. The total charge (*Q*) during this process is equal to the product of the capacitance (*C*) and the voltage across the

double layer (U). As charge-up completes, the current steadily decreases until it reaches the limiting current (t_3 in Figure 2.5c), which is an indication of the mass transport limit: dissolved ions have reached saturation on the electrode surface and the ion concentration gradient is established across the viscous layer (t_3 in Figure 2.5b).

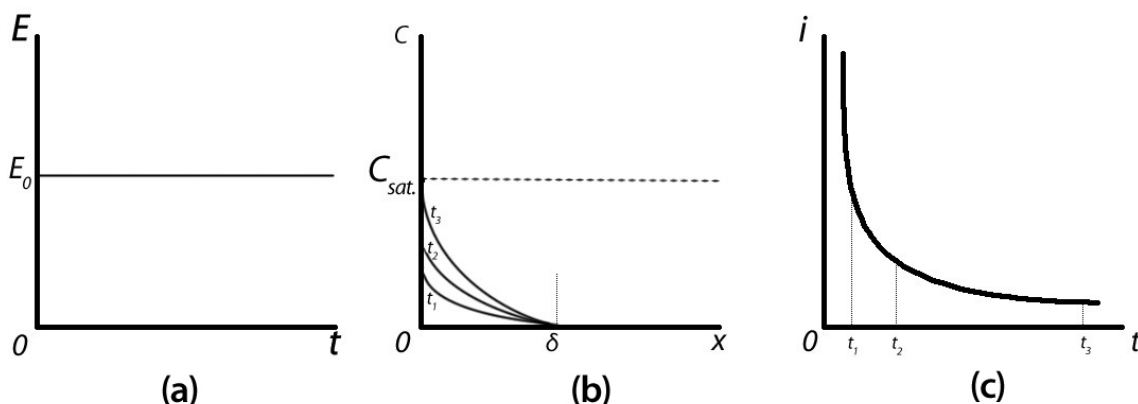


Figure 2.5. In chronoamperometry, the potential is constant(a), the ion concentration gradient profile at different time intervals (b) and the corresponding i - t curve (c).

2.3.2. LINEAR SWEEP VOLTAMMETRY

Instead of being fixed at one value, the potential applied in linear sweep voltammetry is linearly varied (Figure 2.6a). The corresponding current signals, in response to the potential variation, are recorded over time. Since the potential is also a univariate, the current can be plotted against the potential instead, which shows more information, *e.g.* a substantial increase in the current could be attributed to an occurrence of a redox reaction at that specific potential.

A typical i - V curve for electropolishing is shown in Figure 2.6b. Initially, the current increases in conjunction with the potential, until the current reaches a local maximum (branch I in Figure 2.6b), which indicates the end of the active oxide

dissolution. After that, the current decreases due to a buildup of a fresh passive oxide layer (branch II in Figure 2.6b). The limiting current (branch III in Figure 2.6b) corresponds to the mass transport limit of dissolved ions, where electropolishing is achieved. Further increasing potential causes gas bubbling on the surface, which leads to the formation of surface pits and sponges.¹³¹

As indicated above, linear sweep voltammetry can be used to study the redox reaction at the anode and identify the region for electropolishing.

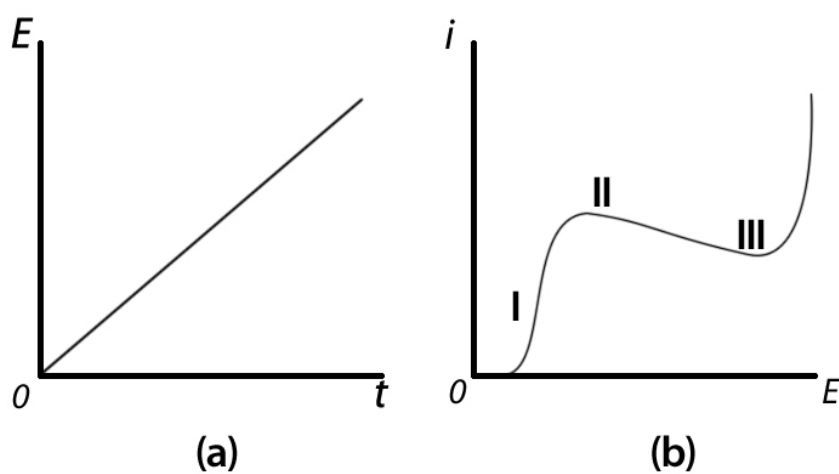


Figure 2.6. Linear potential sweep (a) and resulting i - E curve (b).

2.3.3. CHRONOPOTENTIOMETRY

In chronopotentiometry, the input signal is switched to current and the corresponding output signal is potential. A constant current, galvanostatic, is applied between the working electrode and the counter electrode (Figure 2.7a). Potential between them is recorded over time (Figure 2.7c).

The total charge, Q , correlates with the amount of ions dissolved during electropolishing. Current, which is defined as charge (Q) over time (t), is an indicator of

the rate of electrochemical reactions at the electrode. Galvanostatic means the rate remains constant.

To maintain this constant reaction rate, a potential is applied between the two electrodes (plateau region in Figure 2.7c). However, as dissolved ions at the electrode reach saturation (Figure 2.7b), the potential needs to be increased substantially to keep up with the reaction rate at the electrode (Figure 2.7c). The time elapsed, τ , denotes the time required to reach this mass transport limit stage.

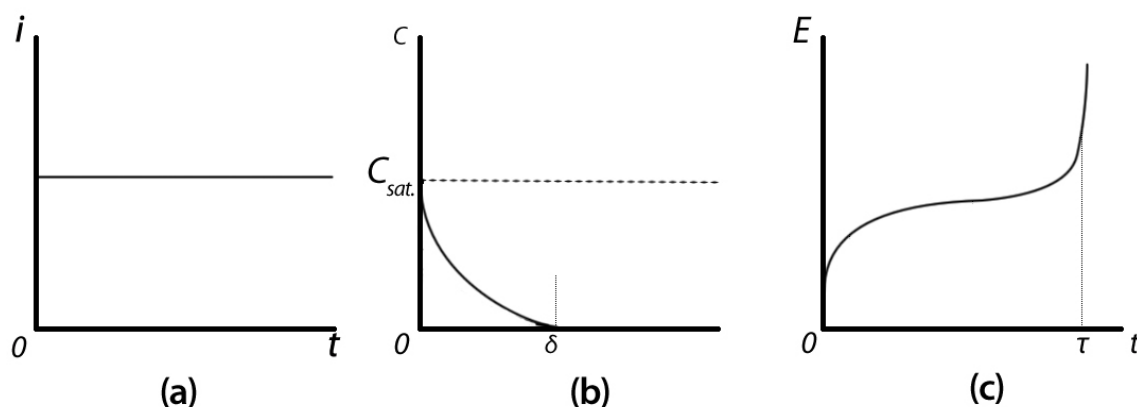


Figure 2.7. The E - t curve in galvanostatic study.

As mentioned above, chronopotentiometry can be used to study the electrochemical reaction rate on the electrode surface. The biggest disadvantage, though, is that the charge-up of the double-layer can occur throughout the whole experiment, which interferes with the current contribution from the reaction.

CHAPTER-3

CHARACTERIZATION TECHNIQUES

With advancements of nanotechnologies, various characterization techniques have been developed to image the surface at nano scale and/or to analyze the surface chemical compositions.

3.1. ATOMIC FORCE MICROSCOPY (AFM)

AFM is developed to overcome STM's limitation on non-conductive materials.¹³²

The prototype of the first AFM bears a lot of resemblance to STM; in fact, it is an STM with a conducting cantilever, which contains an AFM tip at the top. The sample contour induces upward and downward movement of the AFM tip, which is measured as tunnelling current in the STM.

STM-based AFMs have same intrinsic disadvantages as STMs, such as drifting and difficulty in aligning both tips. To overcome these disadvantages, Wickramasinghe¹³³ *et al.* introduced a light lever (Figure 3.1) to replace the STM component.

Any displacement of the AFM tip in the z-direction is 'magnified' by the light lever and projected onto a photodiode. Nowadays, most commercial AFMs are based on this design, with laser as the light source.

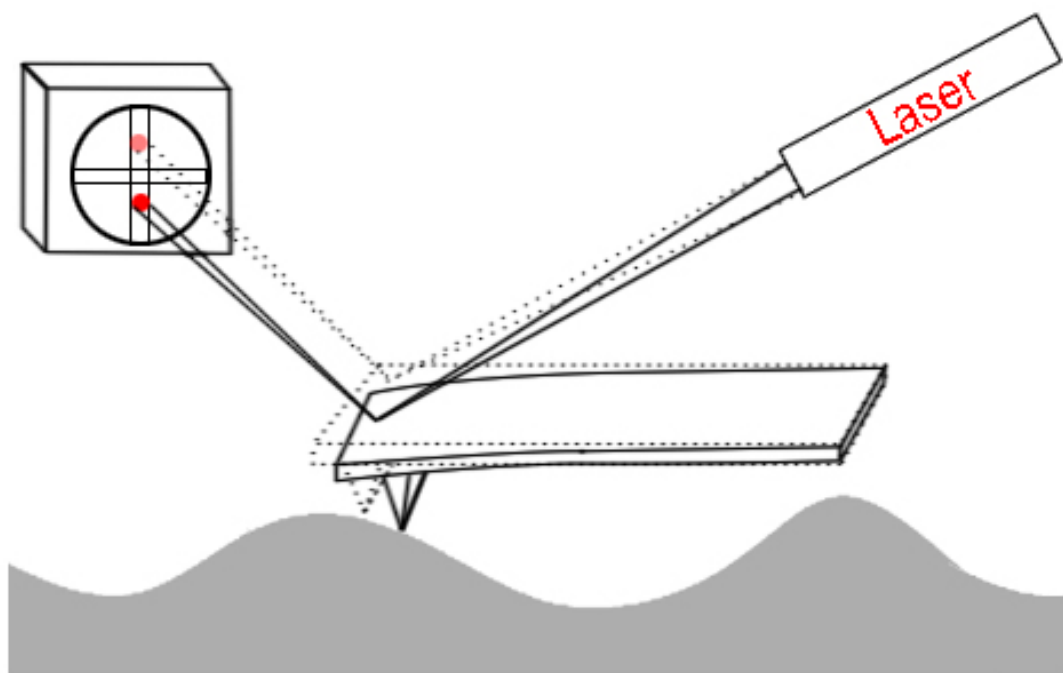


Figure 3.1. The light level system in AFM.

After aligning the laser spot with the AFM cantilever and photodiode, the AFM cantilever is brought close enough to the sample surface to ‘feel’ the atomic force. Possible atomic interactions are summarized in Figure 3.2. If the tip is too close to the sample surface, a strong repulsive force appears between the sample and the tip. If the tip and sample is too far, van der Waals force acts as the attraction force to draw them close.

Depending on the distance between the tip and the sample during scanning, the AFM operating modes can be divided into *Contact* mode (measuring repulsive force at the red branch in Figure 3.2), *Non-contact* mode (attractive force blue branch in Figure 3.2), and Tapping mode.

In the tapping mode, which is used throughout this thesis, the cantilever is vibrating at an optimized frequency to ‘tap’ the surface. The value of this optimized frequency can be obtained by ‘Tuning the tip’ *via* the AFM software.

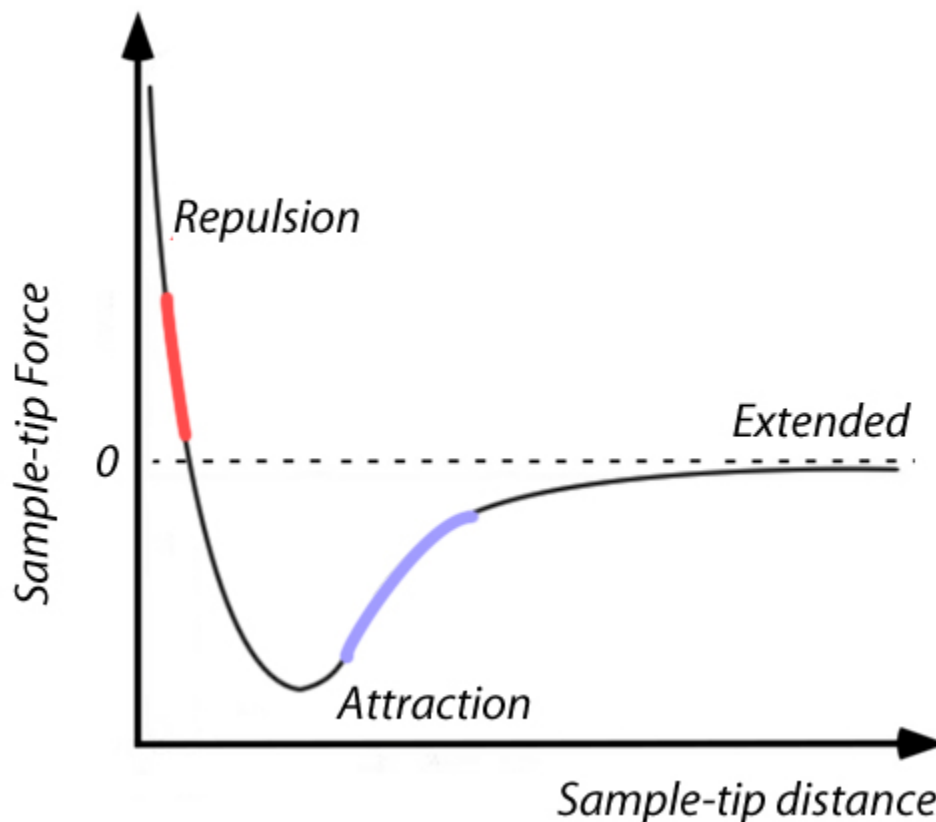


Figure 3.2. The atomic force interaction between the sample and the tip.

During the AFM raster scanning, a piezoelectric tube controls the movement of the sample stage in the x and y direction. During each line scan, say x -direction, the height of the scanner can be held constant. In the *Constant Force* scanning mode, the scanner moves up and down to maintain a constant force between the tip and sample. The z -direction movement of the scanner directly gives the topographic information. The *Constant Force Mode* reduces the likelihood of damaging the sample.

The disadvantage of AFM is the limit on the scanning size and scanning speed. Besides that, AFM is extremely sensitive to environmental disturbances, such as vibration and humidity.

3.2. SCANNING ELECTRON MICROSCOPY (SEM)

For high-resolution SEM, a medium vacuum ($\sim 10^{-5}$ torr) is required, with a Mean Free Path (MFP) between 0.1 and 100 mm. The Mean Free Path is defined as the average distance a particle (electron in this case) can travel before the next collision. A 100 mm MFP ensures that the electron can reach the detector safely.

In SEM, electrons are generated and accelerated to desired energy level (several KeVs to tens of KeVs) in the electron gun. After passing a series of focusing lenses and aligning apertures, the electron beam is focused on the sample surface. The incident angle between the electron beam and the sample surface can be adjusted by tilting the sample stage.

Interactions between the electron beam and the sample are summarized in Figure 3.3. (NB: For simplicity, only relevant interactions are shown in the figure.)

In the case of elastic interactions (*e.g.* Coulomb interaction), no energy or a negligible amount of energy is transferred from the electron to the sample, *i.e.* electrons leaving the sample have the same amount of energy as incident ones, *e.g.* backscattered electrons (Figure 3.3).

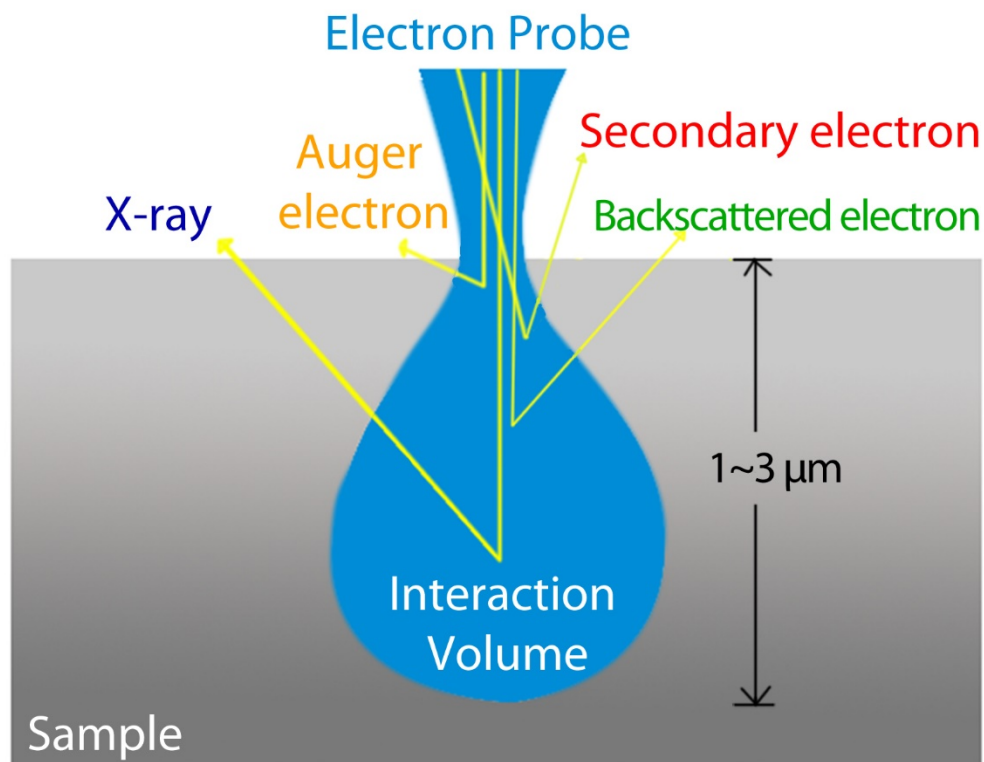


Figure 3.3. Interaction volume

In the case of inelastic interactions, the energy is transferred from the incident electrons to the sample to generate secondary electrons, Auger electrons, X-rays, *etc.*

3.2.1. SEM IMAGING

Ejected by the primary electron beam or backscattered electrons, secondary electrons originate from the conduction band and valence band of the specimen. These electrons normally carry energy around 50 eV. Within an escape depth of 10 nm or less, secondary electrons contain topographic information, thus are the main group of electrons captured for SEM imaging.

The contrast of the SEM image comes from topographic contrast (Figure 3.4). Only electrons, indicated by yellow arrows, can reach the detector.

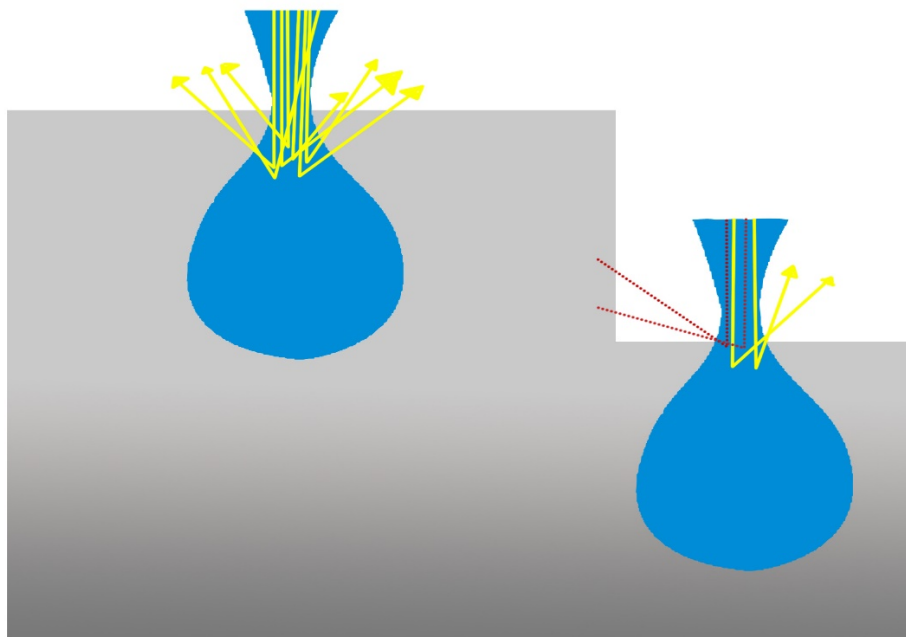


Figure 3.4. Topographic contrast in SEM due to the loss of secondary electrons (red dashed).

According to De Broglie equation, low-energy electrons (several KeVs) behave more like wave than high energy electrons (several tens of KeVs). As a result, low energy electrons can't penetrate deep into the sample. Thus, low KeV electrons are chosen for imaging surface topography.

An SEM image file is a 2-dimensional array stored with 'brightness' data, compared to 'height' data in AFM file. Due to the difference in their imaging mechanism, SEM image is two dimensional, whereas AFM data is three dimensional, with extra height information.

3.2.2. CONTAMINATION

Hydrocarbon contamination on sample surface or in the vacuum can leave a dark area on the SEM image (Figure 3.5). This is because high-energy electron beam can deposit carbon onto the sample during imaging.¹³⁴ To avoid this darkened area in imaging, one could reduce the probe current or simply image an adjacent area which has not been exposed to the electron beam.

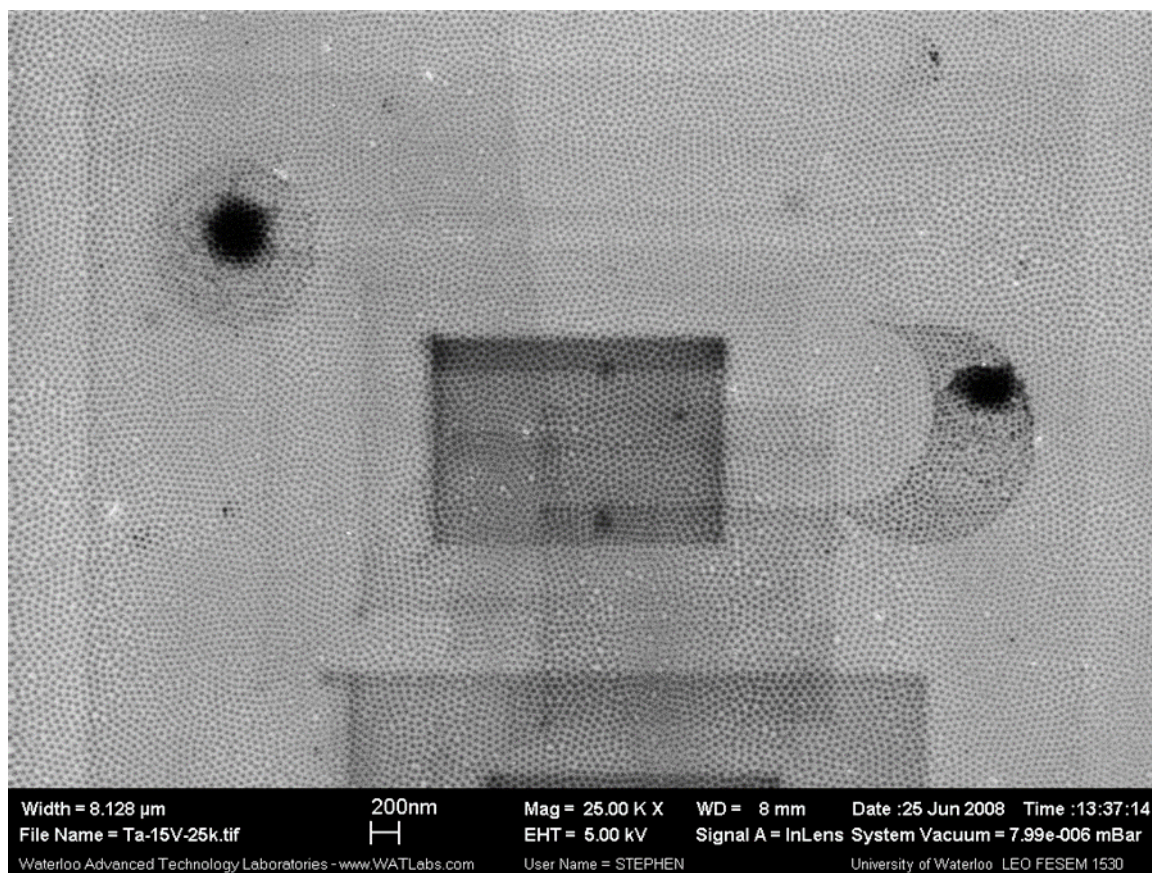


Figure 3.5. Example of poor-quality SEM image due to surface contamination.

3.2.3. CHARGING

Surface charging is a serious issue when imaging a non-conductive surface, *e.g.* oxide. Excessive electrons are stored inside the non-conductive oxide and appear as a

“glow” in the SEM image (Figure 3.6). Coating the sample with a thin layer (several nanometer) of metals (Au or Ag) can significantly reduce this effect.

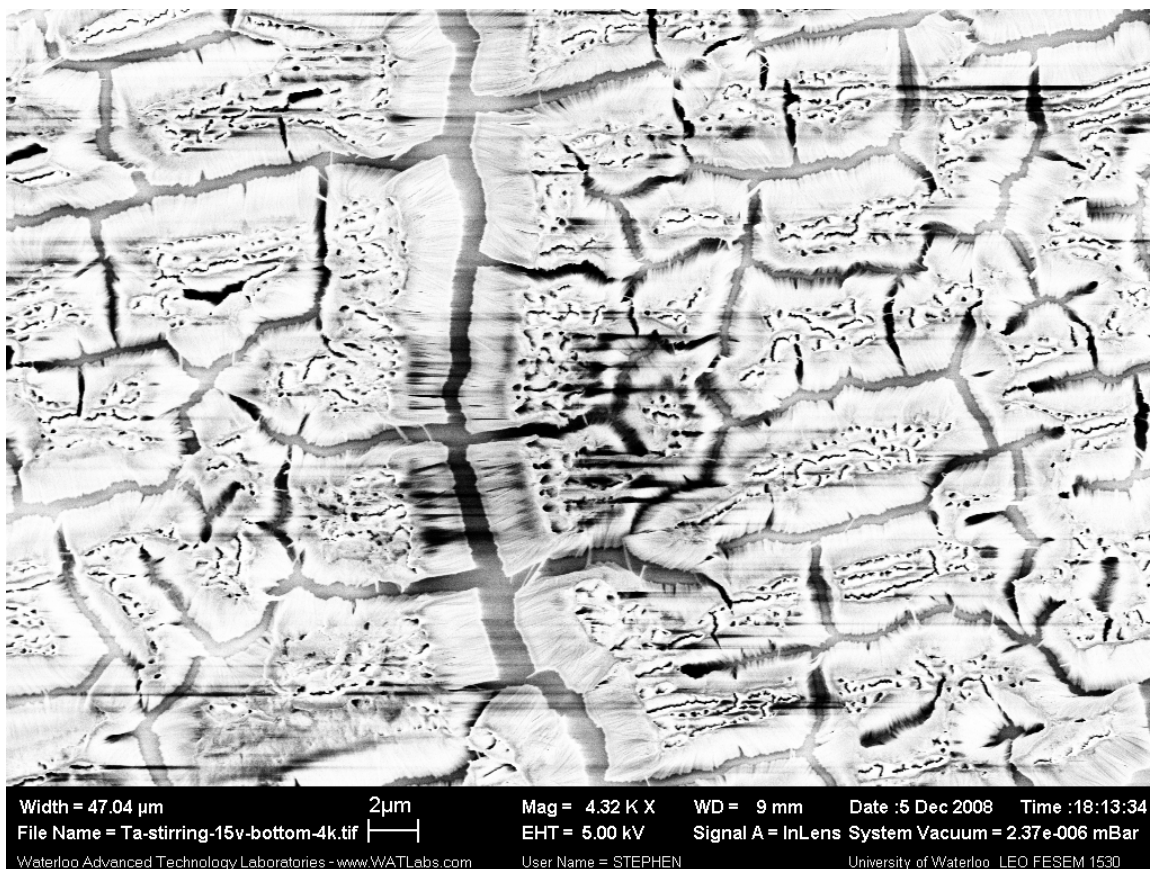


Figure 3.6. Example of poor-quality SEM image of tantalum nanotube due to charging.

3.2.4. ENERGY-DISPERSIVE X-RAY SPECTROSCOPY (EDX)

When SEM is equipped with EDX, it can give additional information on the surface composition.

As indicated by the Interactive volume (Figure 3.3), high energy (tens of KeVs) electrons can penetrate up to several micrometers into the specimen and have enough energy to remove a core electron (Figure 3.7). Electrons from higher levels will jump to

fill in this vacancy, accompanied by the emission of an X-ray photon. Since each element has its own characteristic X-ray fingerprint, EDX can be used to identify surface compositions and quantify their concentrations.

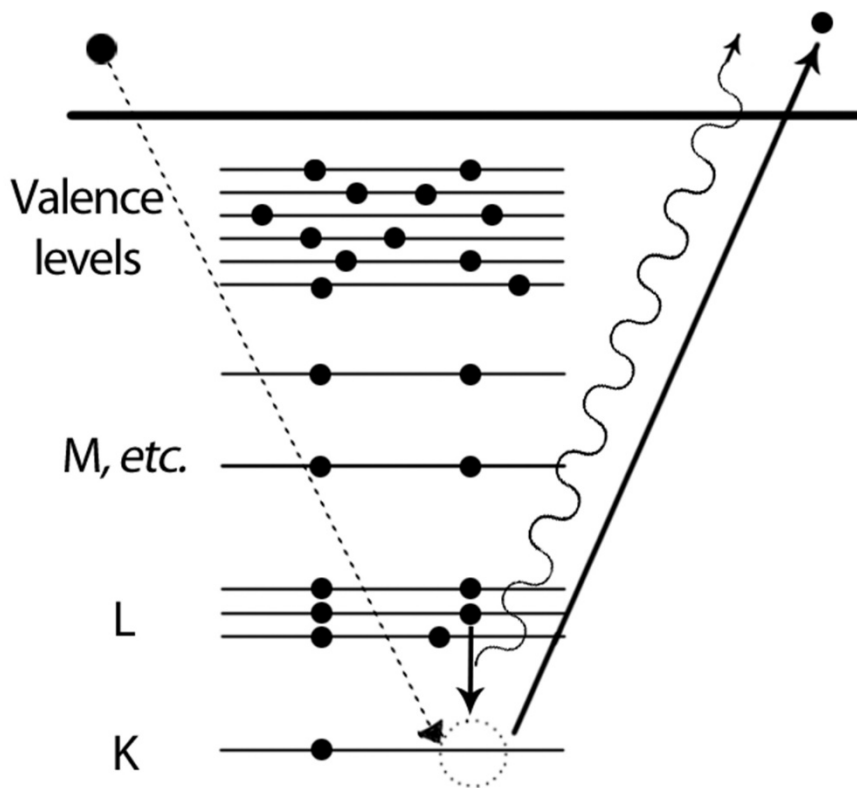


Figure 3.7. The origin of the X-ray photon formed in EDX.

Figure 3.8 is the result of a typical EDX spectrum, which includes thumbnails of the SEM image and area of interest (within red box), a spectrum of various elements present on the surface and normalized counts, and a summary of element compositions, shown in weight percentage as well as in atomic percentage.

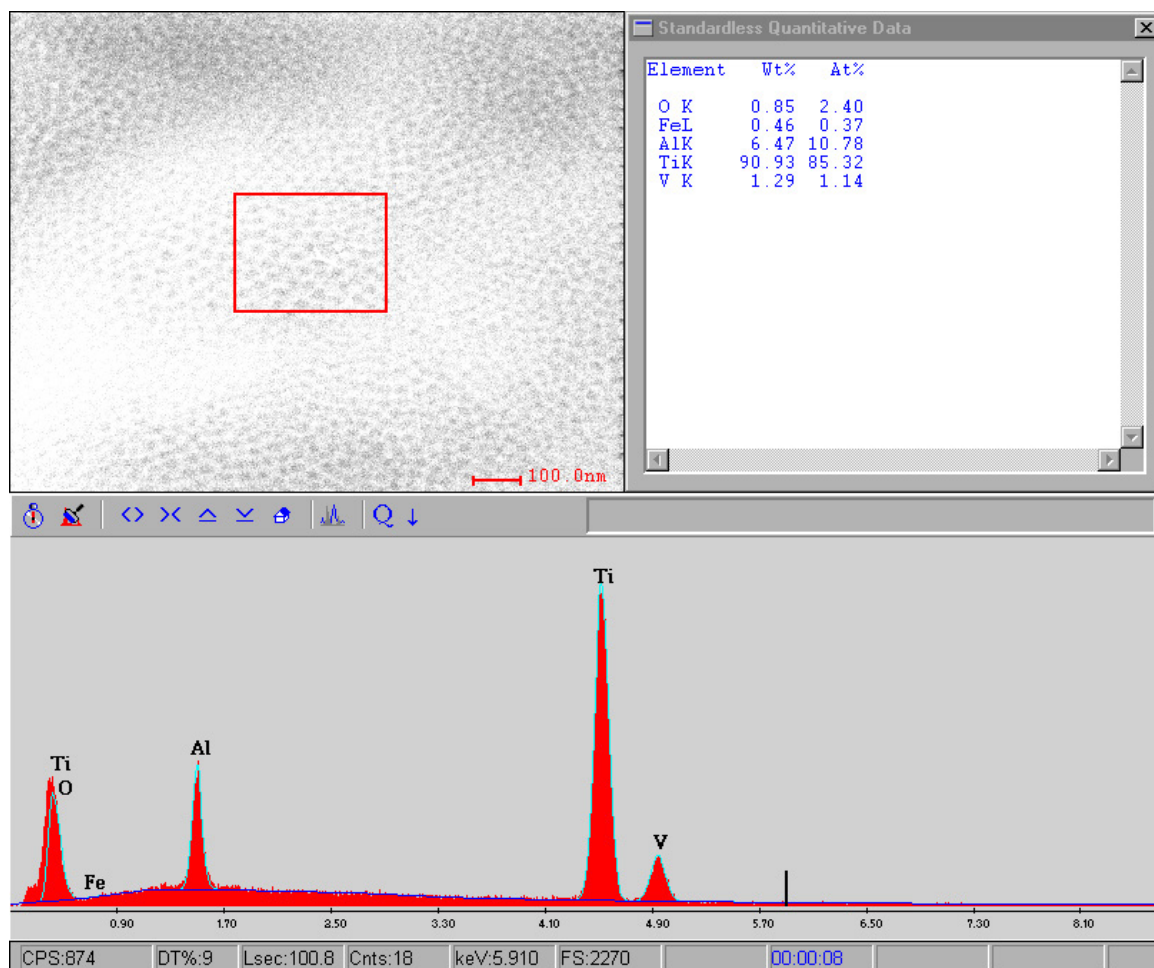


Figure 3.8. EDX of dimple pattern on biomedical alloy (Ti-6Al-4V)

One drawback of EDX is the overlap of peaks, *e.g.* Ti and O at low energies in Figure 3.8, which can distort the result of elemental analysis. Another inherent shortcoming of SEM-EDX is that the photon signals may come from several micrometers beneath the sample surface, which disqualifies EDX as a surface-sensitive technique.¹³⁵

3.3. PHOTOEMISSION ELECTRON MICROSCOPY (PEEM)

Compared to photons, electrons have a much smaller mean free path (Figure 3.3). If electrons from the *Interaction Volume* are detected and analyzed, the result obtained

should be more surface sensitive. This goal can be achieved with the Photoemission Electron Microscope (PEEM).

Many metals can emit photoelectrons after absorbing photons, which is called *Photoelectric effect*. The equation for the *photoelectric effect* is given in Equation 3.1. The kinetic energy of the emitted electrons is equal to the energy difference of the incident photon and the work function of the electron.

$$K = h\nu - W \quad (\text{Equation 3.1})$$

A Hg lamp can be used as the light source in PEEM. In X-PEEM, the source is soft X-ray. In order to achieve a tunable X-ray range and desirable brightness, X-PEEM uses a synchrotron as the light source.

After being excited by photons, photo-emitted electrons are extracted at high voltage and pass through a system of electrostatic and magnetic lenses before captured by the CCD camera. Synchrotron photon energy is scanned to generate the X-ray Absorption Spectrum (XAS). By taking the ratio of the images captured at the peak and the baseline of XAS, a surface composition map is generated.

3.4. ABSORPTION SPECTROSCOPY (VIS)

Visible light contains all the photons with wavelengths from 300 nm to 770 nm. When the light passes through a solution, photons of a certain wavelength are absorbed by ions to excite their d-orbital electrons to a higher energy state. The light, coming out of the solution, is missing photons of that specific wavelength. The colour of the light will be the complimentary colour of the missing photons.

The Vis-spectrum can be used to identify ions in the solution and their oxidation states. It can also quantify the concentration of ions by comparing with a calibration curve (Beer-Lambert Law). The absorption of the solution is calculated as the negative log of transmittance, and it is also equal to the product of concentration (c), molar absorptivity (b), and the path length of the solution (L) (Equation 3.2).

$$Abs = -\log_{10} T = cbL \quad (\text{Equation 3.2})$$

CHAPTER-4

NANO-PATTERNING VANADIUM VIA ELECTROPOLISHING

4.1. INTRODUCTION

Nanofabrication is the art of producing materials with features smaller than a hundred nanometer.²³ These novel materials exhibit distinct properties from bulk materials, which promises them great application in booming nanotechnology.²⁴ To this end, various types of techniques have been proposed.⁶²

Among these techniques, the electrochemical method has emerged as an indispensable tool, due to its low cost and time-efficiency. Porous anodic aluminum oxides (PAAs) have been extensively studied and widely used as templates to build other nano materials⁶⁴; nano-porous anodic titanium oxide has shown greater cell affinity, consequently this material may evolve as a new substrate for implants.¹⁵³ The successful extension of the dimple pattern from tantalum to titanium, tungsten, and zirconium indicates that the electrochemical pattern formation is a universal process. It opens the door to generate an ordered nanopattern on different metals *via* electropolishing under optimized conditions.⁶² However, the mechanism for the pattern formation *via* electropolishing is still not fully understood.

The study of electropolishing and pattern formation on vanadium is of great interest and enormous application value, because vanadium is largely regarded as the ‘inactive’ component in the biomedical implant alloy, due to its poor biocompatibility.⁶¹

Poor biocompatibility is mainly attributed to the lack of nanoscale surface features to accommodate cells.⁶¹

In this chapter, we discuss the formation of different types of nanopatterns on vanadium *via* electropolishing. The window for the formation of these patterns is far away from conventional electropolishing conditions. The formation of these patterns is extremely sensitive to electropolishing conditions, such as electrolyte composition, electropolishing potential, and time. Both qualitative and quantitative experimental results are scrutinized in the context of existing models on pattern formation.

4.2. EXPERIMENTAL

Vanadium, named after Scandinavian goddess *Vanadis*, is known for the colourfulness of its ions at different oxidation states (Table 4.1).¹³⁶ Pure vanadium has a bright refractory white colour and is soft and ductile with a melting point of 1887°C.¹³⁶

Table 4.1. The different oxidation numbers of vanadium and colours

Oxidation Number	State in solution	Colour
V	VO_2^+ (pH < 1.8)	Yellow
V	Polymerized (pH > 2)	Orange-yellow
V	VO_3^- (pH > 10)	Colourless
IV	VO^{2+}	Blue
III	V^{3+}	Green
II	V^{2+}	Violet

Prior to electropolishing, vanadium wire (99.92%, 1/4 mm in diameter, Alfa Aesar) is cut into 2.5 cm long pieces and ultrasonicated in acetone (HPLC, Caledon), methanol (HPLC, Caledon) and Millipore water (18.2 M Ω •cm), respectively.

The electrolyte is prepared using 48.5% HF (wt. %, EMD), 96.2% H₂SO₄ (wt. %, Caledon) and oleum, which contains 20% free SO₃ (Sigma Aldrich). All apparatuses in contact with the electrolyte are made of PTFE.

Nominally 0%-water electrolyte is prepared in this way: after mixing HF with H₂SO₄, the ‘free’ water in the electrolyte further reacts with equal moles of SO₃ from oleum. The electrolyte is stirred vigorously overnight in a sealed PTFE container with little trapped air. However, due to the dimerization of H₂SO₄, the actual water concentration in the electrolyte will not be zero.

The electrochemical setup is shown in Figure 4.1. For each experiment, 4mL of fresh electrolyte is used, unless otherwise specified. The counter electrode is a Pt/Ir wire loop (3cm in diameter), attached to the cathode alligator clip. The vanadium wire is attached to the anode alligator clip, the vertical position of which is precisely controlled by a stage controller. Initially positioned at the center above the cathode loop, the vanadium sample is perpendicularly brought down to touch the bottom of the PTFE beaker. By taking this extra step, the length of the wire (anode) dipped in the electrolyte is exactly equal to the height of the electrolyte. Since the volume of the electrolyte is fixed (4 mL), the surface area of the anode is fixed as well. The surface area of the cathode is

about twenty times larger than that of the anode to minimize interference from the cathode, because the anode is the working electrode (*Cf.* 2.1).

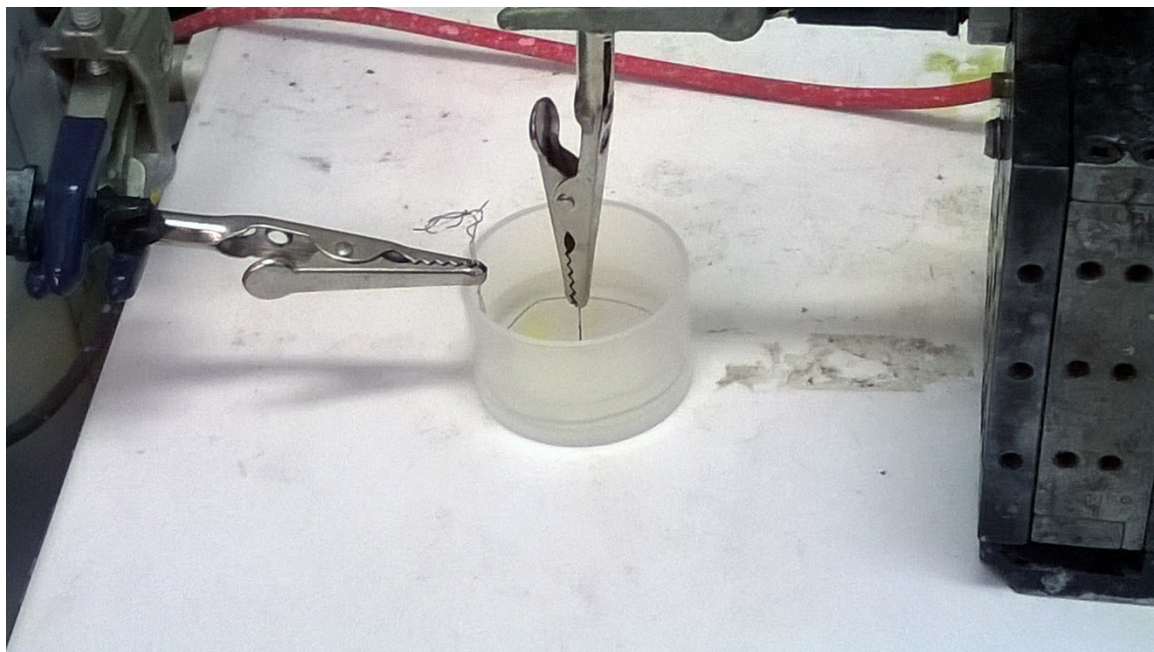


Figure 4.1 The electrochemical setup during electropolishing.

During the experiment, the electrolyte is kept stationary, without stirring. All the experiments are performed at room temperature. No attempt is made to thermostat the electrolyte.

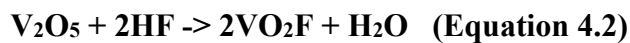
The power supply is Agilent E3617A and the multimeter is HP 34401A. Immediately after electropolishing, the sample is thoroughly rinsed with Millipore water and dried in air.

UV-vis spectra are taken using a BioChem 105 spectrometer, SEM imaging is done using a JOEL-7000F, and AFM imaging is performed on a Veeco Enviroscope with

a Nanoscope IIIa controller and Veeco TRESP p-doped Si tips with a nominal radius of less than 10 nm.

4.3. RESULTS

During electropolishing, the vanadium metal is first oxidized (Equation 4.1) and then dissolved by HF in the electrolyte (Equation 4.2). The formation of VO_2^+ is confirmed by the yellow-brownish colour observed at the anode (Figure 4.1) and *Vis* spectrum¹³⁷ (Figure 4.2).



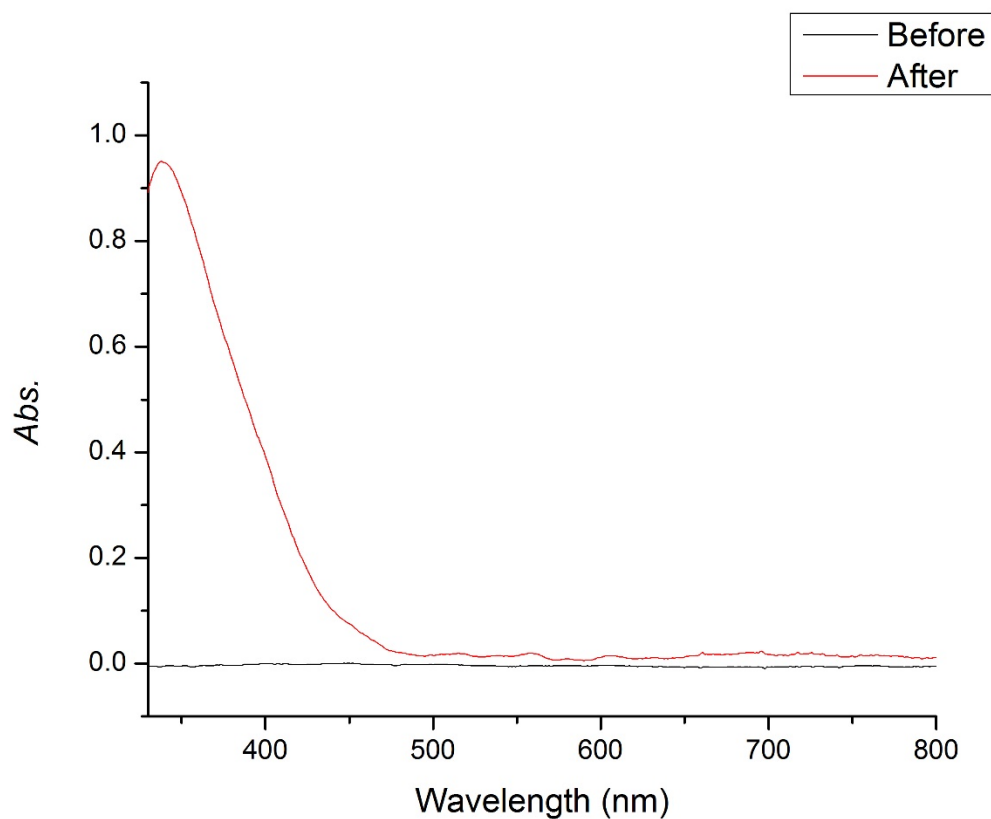


Figure 4.2. The *Vis.* Spectra taken before and after electropolishing confirms the formation of VO_2^+ during electropolishing.¹³⁷

4.3.1. THE FORMATION OF PATTERNS

When vanadium wires are electropolished in the $\text{HF}/\text{H}_2\text{SO}_4$ electrolyte, a flat surface (Figure 4.3a), pimple (Figure 4.3b), labyrinth (Figure 4.3c) and dimple (Figure 4.3d) patterns have been observed. All samples have been electropolished at 20V for 5 minutes, but in different electrolytes (Table 4.2). All the patterns are uniformly distributed across the sample surfaces.

Table 4.2. The detailed breakdown of electrolytes for flat surface, pimples, labyrinths, and dimples on vanadium during electropolishing.

		Flat Surface	Pimples	Labyrinths	Dimples
HF	wt. %	0.7%	0.7%	0.7%	0.7%
H₂O	wt. %	0	0.1%	0.3%	0.6%
H₂SO₄	wt. %	99.3%	99.2%	99.0%	98.7%

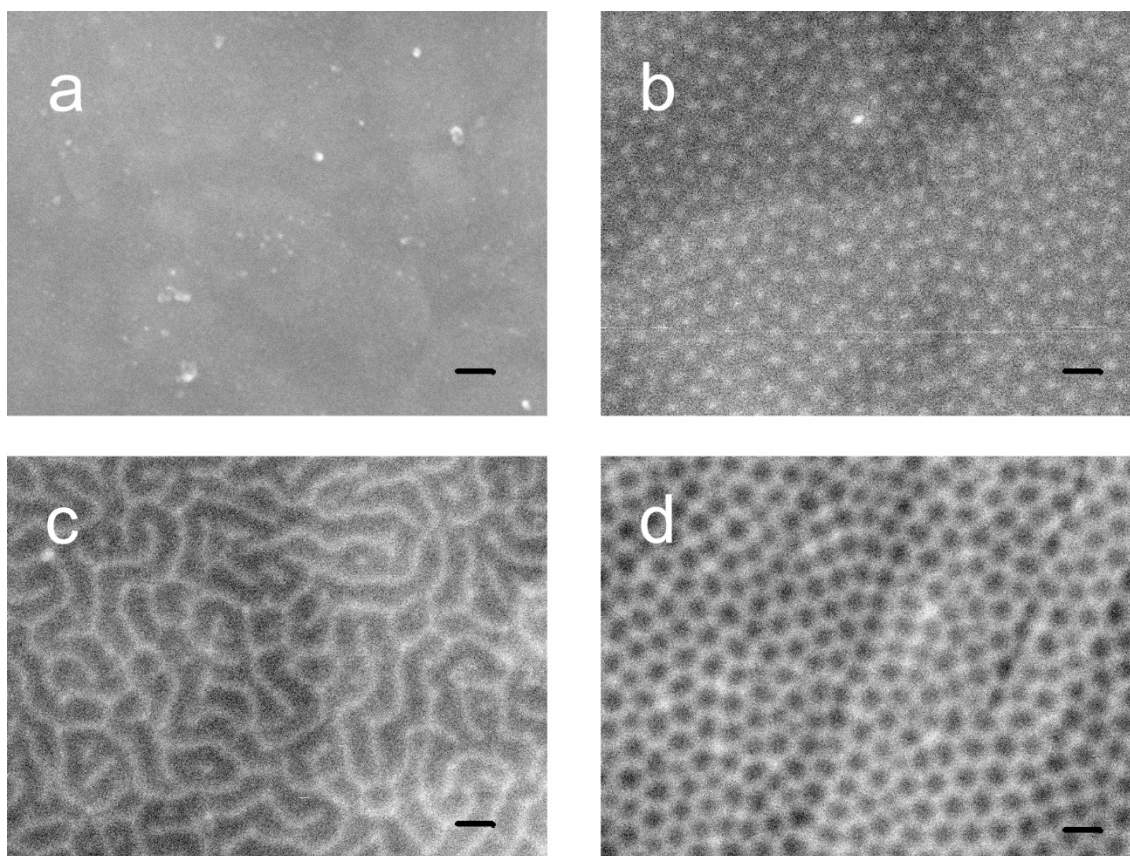


Figure 4.3. SEM images of the electropolished vanadium surfaces. a) Flat surface, b) Pimple pattern, c) Labyrinth pattern, and d) Dimple pattern (Scale bar 100 nm).

AFM can reveal the depth/height of each pattern. Samples used for AFM measurements are the same from Table 4.2, as shown in Figure 4.3.

A cross-sectional profile of dimples (red line in Figure 4.4) shows that the dimple pattern is approximately 7 nm in depth. Compared to that, the pimple pattern is more subtle, with an average height of 4 nm (green line Figure 4.4).

What's more, the average spacing of the dimple pattern is also larger than that of the pimple pattern. This phenomenon is caused by the addition of extra water into the electrolyte (Table 4.2), which increases the conductivity of the electrolyte and the current density during electropolishing. The higher the current density, the larger the periodicity of the pattern.

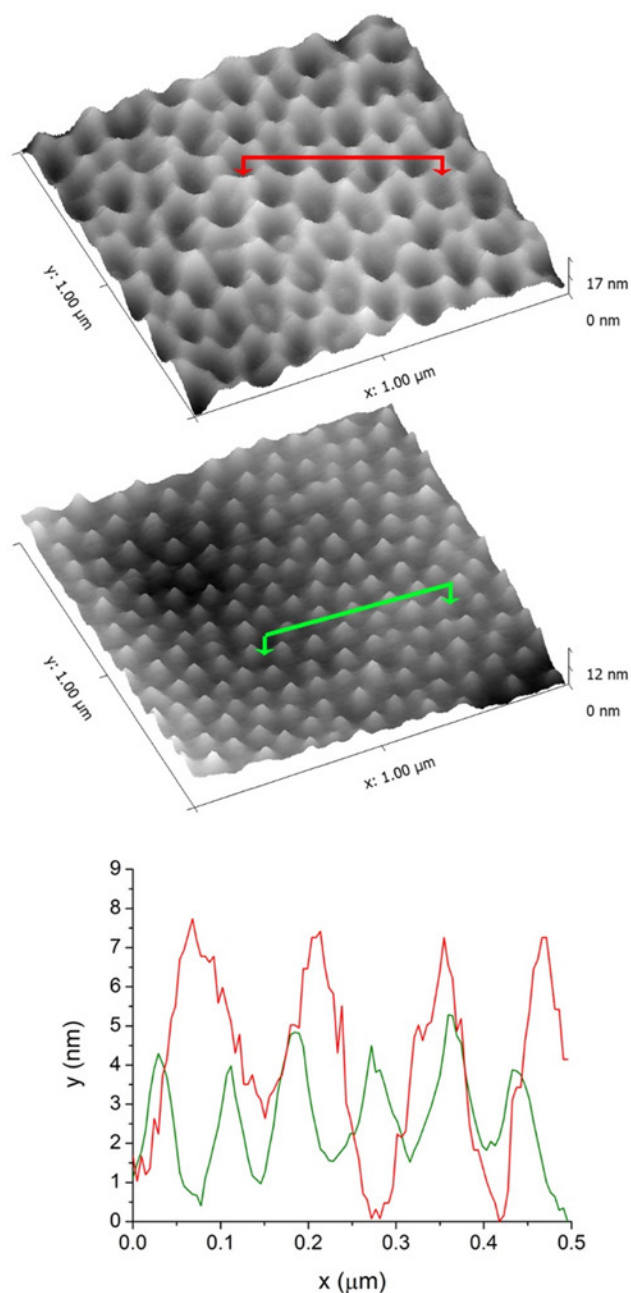


Figure 4.4. 3D AFM images of the dimple and pimple pattern and cross section profile of each pattern. The average depth of dimple is about 7nm and the average height of pimple is about 4nm and dimple is wider than pimple. (NB: the y-scale difference in the 3D AFM images and the cross-section profile AFM images.)

4.3.2. WHAT MATTERS?

The formation of these nanopatterns occurs only within a small set of conditions. Outside of this window, the electropolished samples are normally featureless.

The pattern formation is highly sensitive to the specific electropolishing arrangements. Systematic analyses have been carried out to study each parameter's impact on the pattern formation, which include electrolyte compositions, the applied potential, the electropolishing time, the aspect ratio of the electrode over the electrolyte, and the native oxide before electropolishing. The detailed impact of each parameter on the pattern formation is studied below.

4.3.2.1. WATER IN THE ELECTROLYTE

A small variance ($\sim 0.1\%$) in the water concentration of the electrolyte results in a pattern transition on vanadium (Figure 4.5).

The detailed composition of electrolytes is summarized in Table 4.3. The concentration of HF is kept constant in all trials. The concentration of water increases from 0% to 1.05% with a step of 0.15%, at the expense of sulphuric acid.

Table 4.3. The composition (wt. %) of electrolytes in the water concentration varying experiment. The number of samples correspond with the image number in Figure 4.5.

	a	b	c	d	e	f
H ₂ SO ₄	99.3%	99.15%	99.0%	98.7%	98.4%	98.25%
HF	0.7%	0.7%	0.7%	0.7%	0.7%	0.7%
H ₂ O	0%	0.15%	0.3%	0.6%	0.9%	1.05%

The first sample (Table 4.3a / Figure 4.5a) produces a nanoscale flat surface with no patterns. With increasing water concentration, a transition from the pimple pattern (Figure 4.5b), to a mixture of the pimple and labyrinth patterns (Figure 4.5c), to the labyrinth pattern (Figure 4.5d), finally to the dimple pattern (Figure 4.5e, f) has been observed on electropolished vanadium samples.

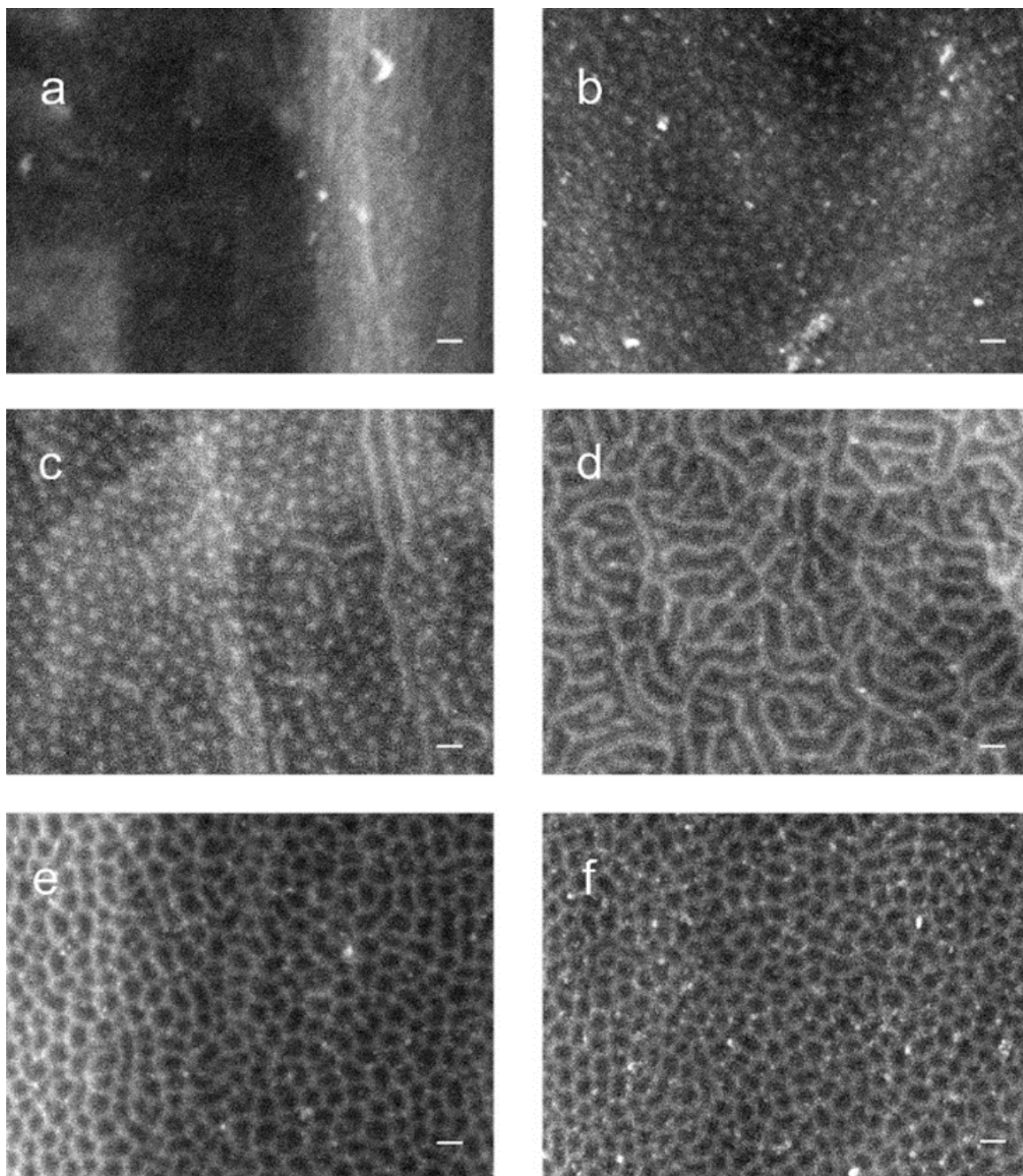


Figure 4.5. The transition of patterns due to the water concentration variance in the electrolyte. Each sample (a ~ f) is electropolished at 20V for 5 minutes, but in different electrolytes, as listed in Table 4.3. (Scale bar: 100 nm)

4.3.2.2. HF IN THE ELECTROLYTE

A similar trend is observed when keeping the water concentration constant at 0.3%, while increasing the concentration of HF in the electrolyte (Table 4.4).

Table 4.4. The composition (wt. %) of electrolytes in the HF concentration varying experiment. The number of samples correspond with the image number in Figure 4.6.

	a	b	c	d	e	f
H ₂ SO ₄	99.2%	99.1%	99.0%	98.8%	98.7%	98.2%
HF	0.5%	0.6%	0.7%	0.9%	1.0%	1.5%
H ₂ O	0.3%	0.3%	0.3%	0.3%	0.3%	0.3%
Pattern	Flat	Pimple	Pimple/ Labyrinth	Labyrinth/ Dimple	Dimple	Random

Detailed compositions of electrolytes are shown in Table 4.4. A pattern transition is observed from a flat surface (Figure 4.6a), to a pimple pattern (Figure 4.6b), to a mixed pimple and labyrinth pattern (Figure 4.6c), to a mixed labyrinth and dimple pattern (Figure 4.6d), to a dimple pattern (Figure 4.6e), to a random pattern (Figure 4.6f). This random pattern indicates the boundary of the pattern formation.

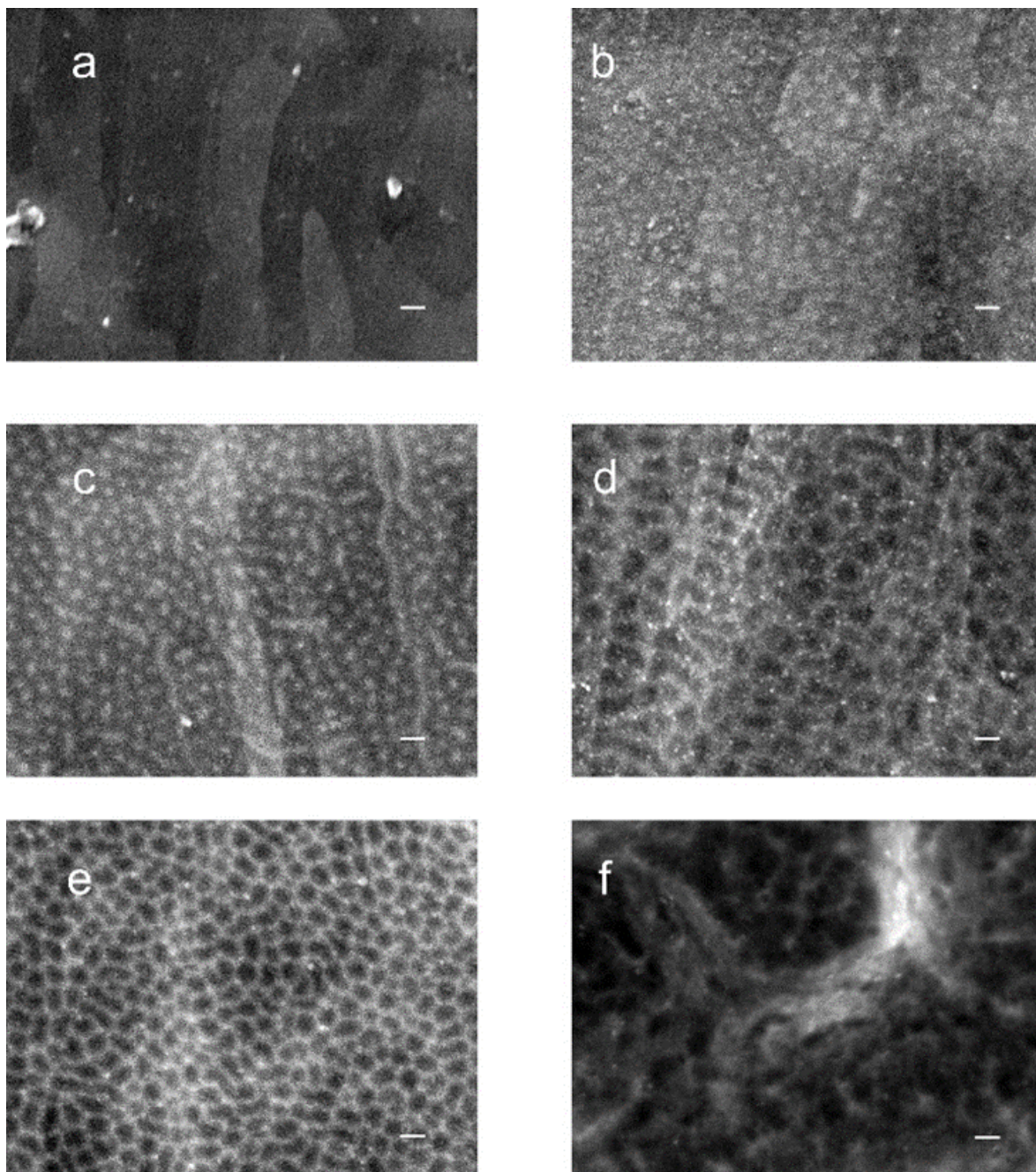


Figure 4.6. Patterns' dependence on the HF concentration in the electrolyte. Each sample (a~f) is electropolished for 5 minutes at 20V in electrolytes listed in Table 2. (Scale bar: 100 nm)

4.3.2.3. WATER-HF BALANCE

The water-concentration-varying study (Figure 4.5) and HF-concentration-varying experiment (Figure 4.6) have shown the impact of electrolyte composition on the pattern formation. Instead of analyzing one parameter at a time, the combined impact of water and HF on the pattern formation is summarised in a phase diagram (Figure 4.7).

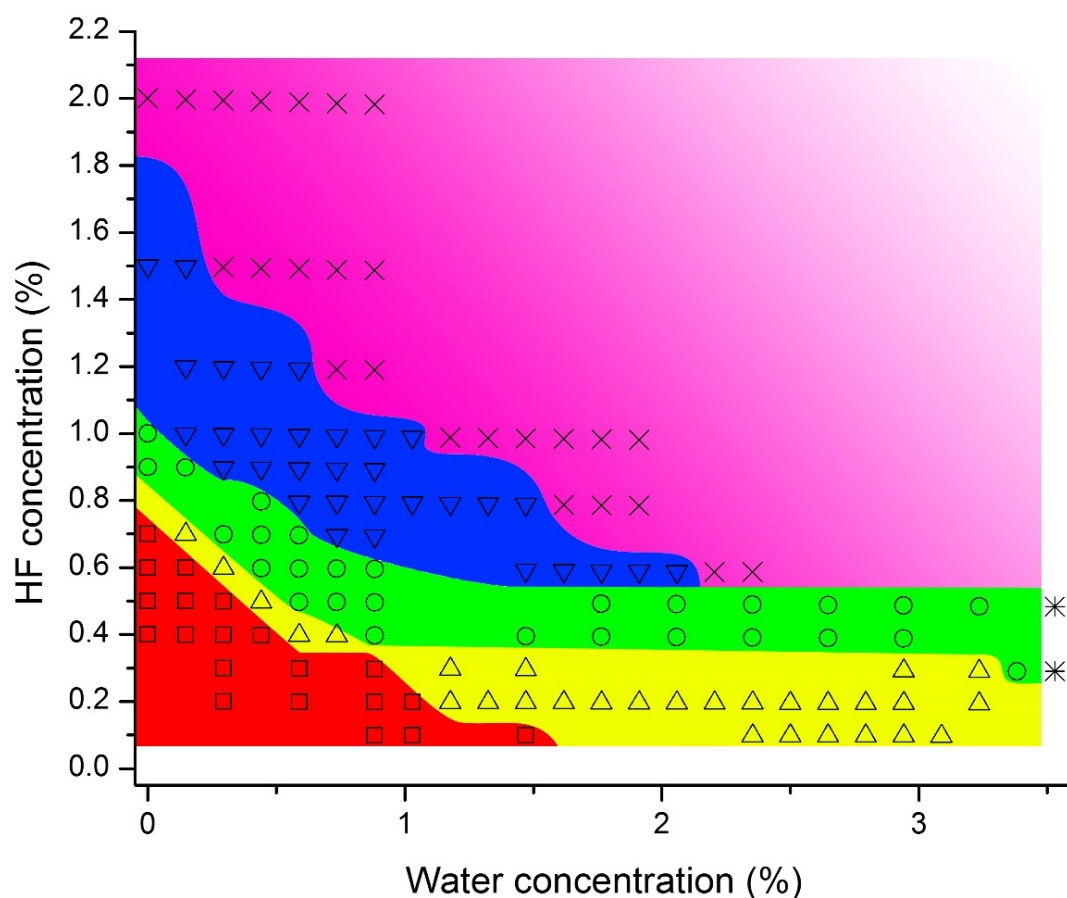


Figure 4.7. Phase diagram of all the patterns on vanadium electropolished in different electrolytes. The flat pattern is highlighted with red colour; pimple yellow colour; labyrinth green colour; dimple blue colour; and random pink collar.

The red shaded area in the phase diagram indicates a nanoscale-flat surface, as shown in Figure 4.6a; colour yellow represents the pimple pattern formation, as shown in Figure 4.6b; colour green stands for the labyrinth pattern, as in Figure 4.5d; colour blue symbolizes the formation of the dimple pattern, as in Figure 4.6e; pink is used when a random pattern, *e.g.* Figure 4.6f, is achieved; * sign and white area mean that the whole wire is completely dissolved in less than 5 minutes, thus no pattern could be identified.

The nanoscale-flat colour red forms a quasi-triangle area, which indicates that concentrations of water and HF are too low to form any pattern during electropolishing. It is also noteworthy that the range of water concentration, which contains no pattern, is wider than that of HF. This phenomenon hints that HF plays a dominant role in the pattern formation. This assertion is consistent with another observation made in the 0% HF experiment (not shown in Figure 4.7). Commercial sulphuric acid contains 3.8% water and 96.2% H_2SO_4 . The vanadium sample, electropolished in this electrolyte, is flat at nanoscale. HF's dominant role in the pattern formation can be explained by the fact that it dissolves the vanadium anodic oxide (Equation 4.2).

As the concentration of HF/water increases, pattern transition starts to occur in the phase diagram. Within the range of 0.1% ~ 0.2% HF, the nanoscale-flat surface is replaced by pimples, as the water concentration increases. Within the range of 0.3% ~ 0.5% HF, the nanoscale-flat surface is first replaced by pimples and then by labyrinths. Within 0.6% ~ 0.7% HF, a full spectrum of pattern transition, from nanoscale-flat surface, to pimples, then to labyrinths, to dimples, finally to random patterns, can be observed with increasing water concentration. Between 0.8%~ 1.1% HF, the full pattern transition

except the flat surface and pimples can be observed, as the water concentration goes up. Between 1.1% ~ 1.8% HF, a dimple pattern to random pattern transition is observed, before random pattern rules at higher HF concentration ($> 1.8\%$).

4.3.2.4. ELECTROPOLISHING POTENTIAL

Compared to the impact from electrolyte concentrations, the electropolishing potential plays a more subtle role on the pattern formation. It alters the spacing (periodicity) of patterns (Figure 4.8).

The following experiment is performed in the 98.65% H_2SO_4 , 0.45% H_2O and 0.9% HF electrolyte, with electropolishing potential ranging from 10 V to 25 V. All the samples have been electropolished for 5 minutes.

At low potentials (*e.g.* 10 V, Figure 4.8a), there is no pattern on the metal surface. Irregular dimples start to appear at 15 V (Figure 4.8b). As the potential increases, the size, order and prominence of dimples exponentially improve (Figure 4.8c) and are optimized at 20V (Figure 4.8d). If the potential is further increased, dimples continue to increase in size, but the ordering deteriorates (Figure 4.8e, f). As a result, 20 V is chosen as the optimal electropolishing potential throughout experiments to maintain consistency and coherence.

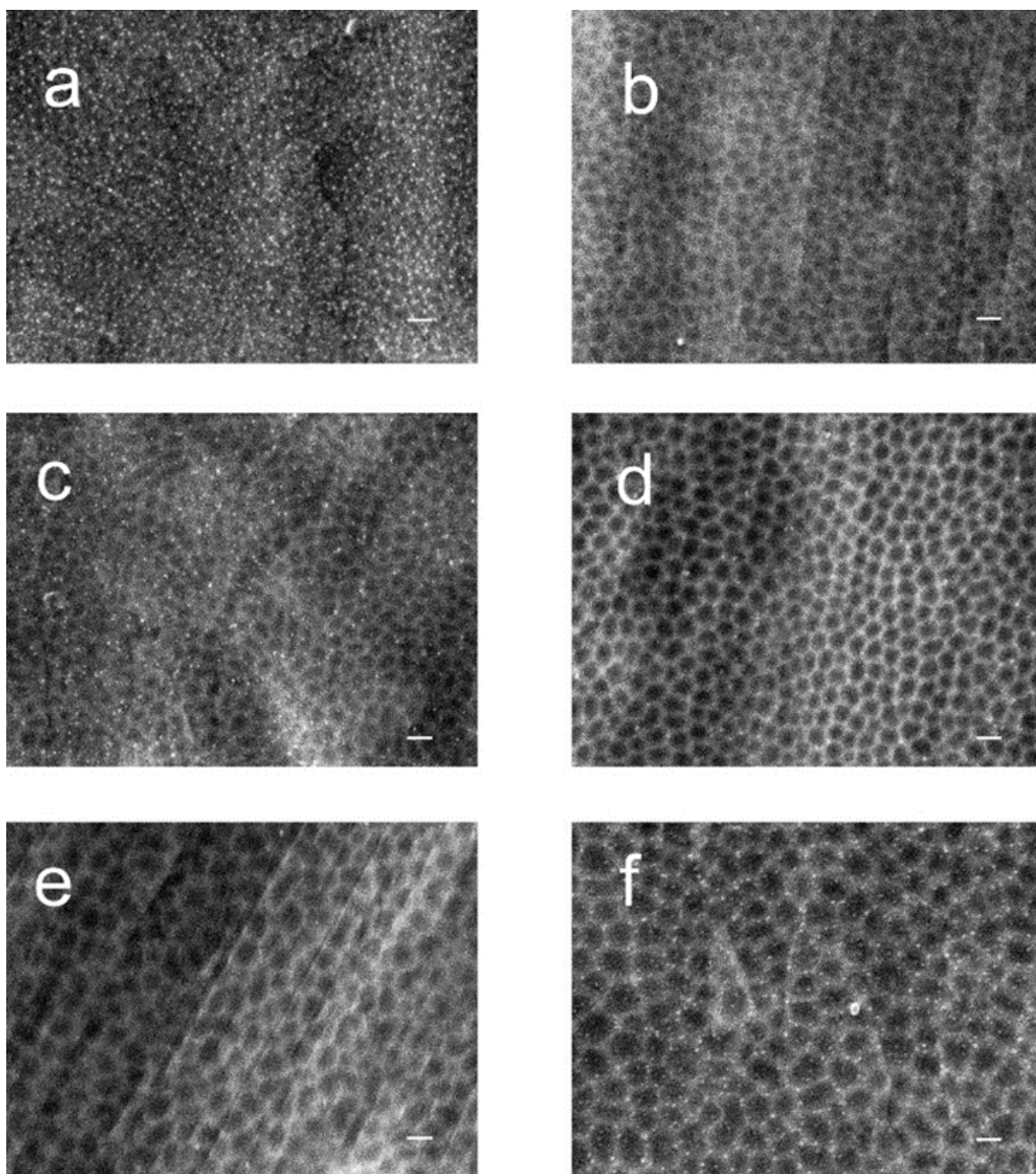


Figure 4.8. Pattern's dependence on potential. Each sample is electropolished in the 98.7% H_2SO_4 , 0.4% H_2O and 0.9% electrolyte for 5 minutes at different potentials: a) 10V, b) 15V, c) 17.5V, d) 20V, e) 22.5V, f) 25V. (Scale bar 100 nm)

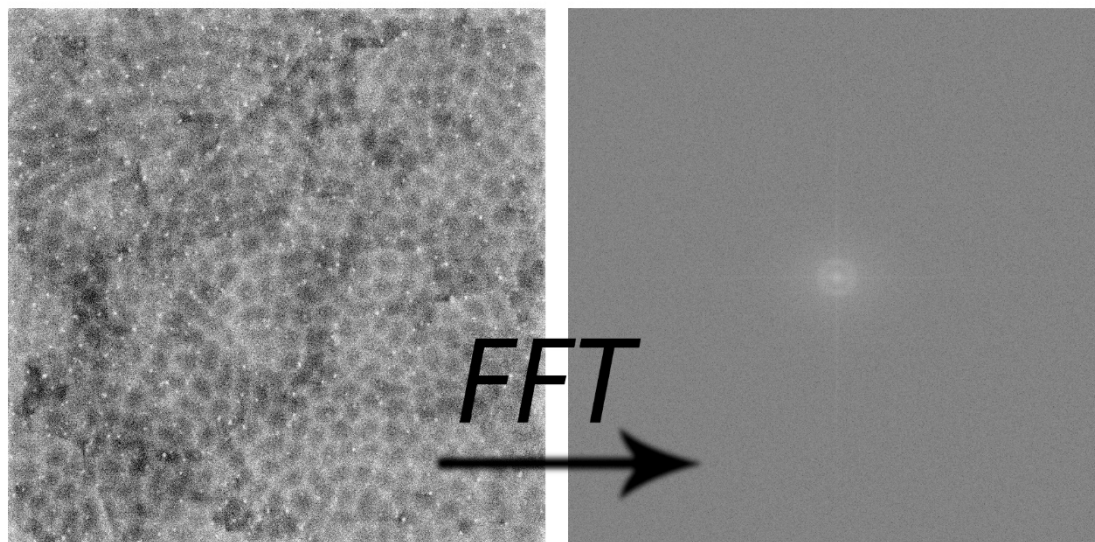


Figure 4.9. Fast Fourier Transform (FFT) of an SEM image (left).

To generate the periodicity of patterns in Figure 4.8, *ImageJ*¹³⁸ is used to first perform Fast Fourier Transform (Figure 4.9) on each SEM image in Figure 4.8, after which, the 2D reciprocal image is converted into one dimensional profile by the ‘*Radial Profile*’ plugin¹³⁹ in *ImageJ*. Then, the one dimensional profile is peak-fitted in Origin. The position of the peak in the one dimensional profile can be used to back-calculate the spacing in real-space, which is the periodicity of patterns. The error bar in Figure 4.10 comes from the full width at half maximum, which originates from the ring width in the 2D reciprocal image as shown Figure 4.9.

The periodicity obtained from each SEM image in Figure 4.8 is plotted against its corresponding potential. It shows a clear correlation between the pattern periodicity and the electropolishing potential. Within a certain range, the periodicity of patterns increases in accordance with the electropolishing potential (Figure 4.10). Electrolyte compositions

are: 0.9% HF/0.6% water/98.5% H₂SO₄ for dimples, 0.4% HF/0.9% water/ 98.7% H₂SO₄ for labyrinths, and 0.5% HF/0.45% water/99.05% H₂SO₄ for pimples.

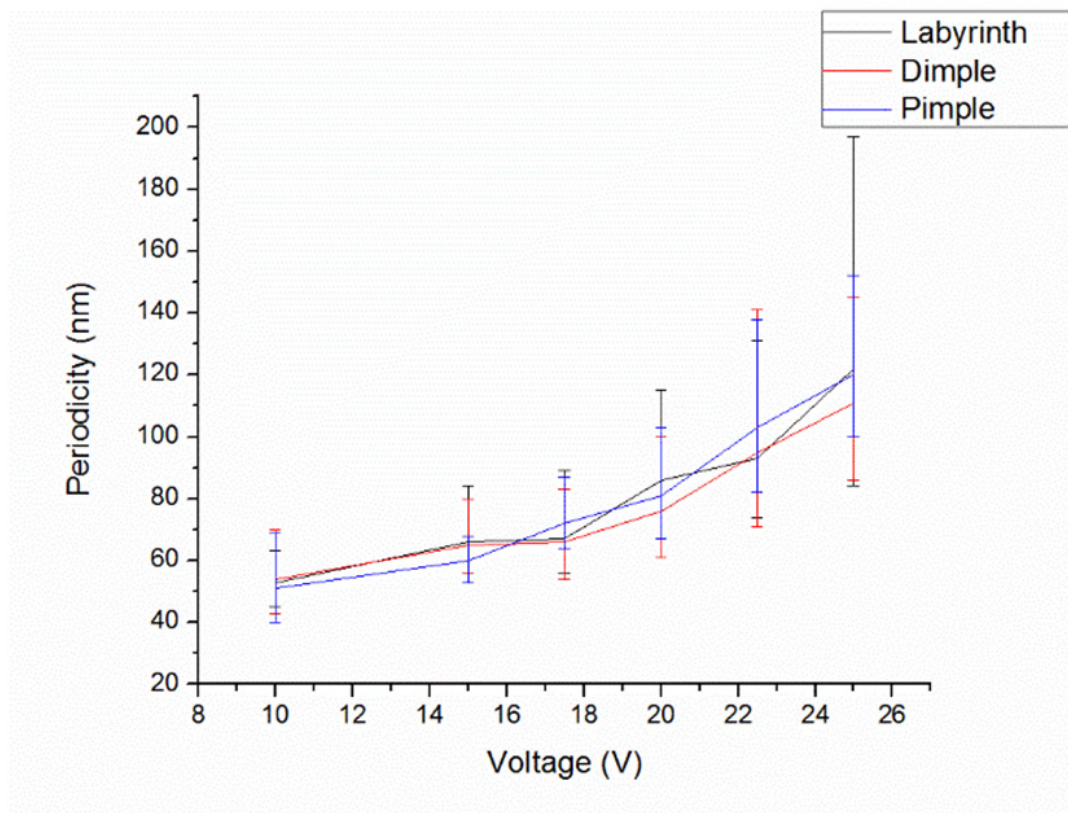


Figure 4.10. Potential's impact on the pattern's periodicity. As the potential increases, the spacing between each pattern also increases.

4.3.2.5. TIME EVOLUTION

The pattern displayed on the electropolished sample is also dependent on the electropolishing time. The following experiment is carried out in the 99% H₂SO₄, 0.6% HF and 0.4% H₂O electrolyte. The electropolishing potential is 20 V.

After 30 seconds of electropolishing, a shallow wave pattern is spotted on the sample (Figure 4.11a). A faint labyrinth pattern can be observed on the sample, which has been electropolished for 2 minutes (Figure 4.11b). Clear labyrinths are developed on the sample, which has been electropolished for 5 minutes (Figure 4.11c). The dimple pattern (Figure 4.11d) replaces the labyrinth pattern on the sample, which has been electropolished for 15 minutes. After 30 minutes of electropolishing or longer, the dimple pattern is erased off the surface, which is covered with some etched pits (Figure 4.11e, f).

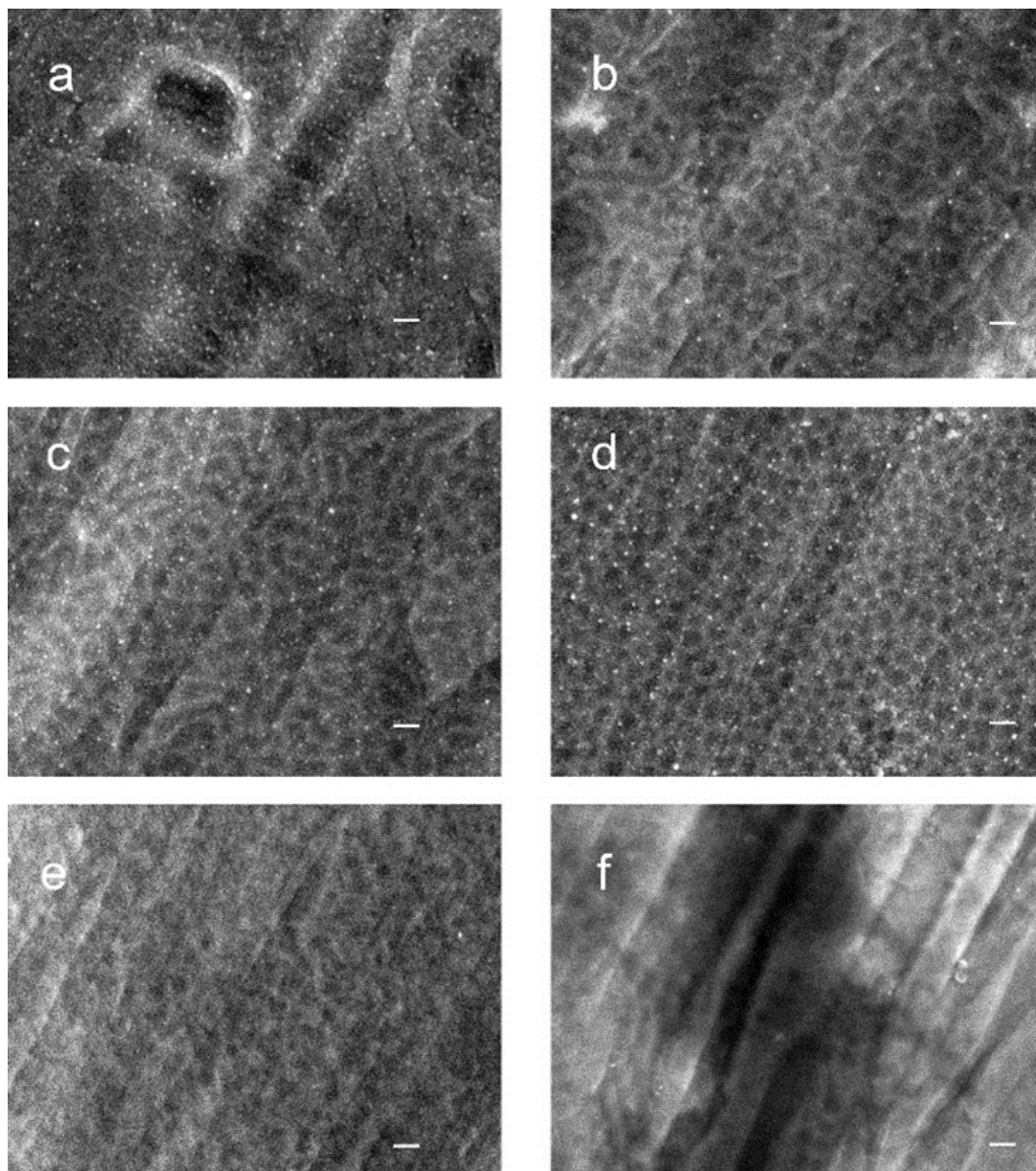


Figure 4.11. The pattern evolution also depends on the electropolishing time. Sample a~f are electropolished in 99% H_2SO_4 , 0.6% HF and 0.4% H_2O electrolyte for a) 30 seconds, b) 2 minutes, c) 5 minutes, d) 15 minutes, e) 30 minutes and f) 120 minutes. (Scale bar: 100nm)

Patterns observed in the evolution experiment are in the same sequence as those in the water/HF concentration-varying experiment.

Results from the evolution experiments suggest that there is a continuous pattern transition occurring on the electrode *in-situ*. Although direct methods for studying this pattern evolution are still lacking, this pattern evolution can be regarded as a calibration curve. *X*-axis is time and *y*-axis is different kinds of patterns. With this calibration curve, it is possible to compare and study other parameters' impact on the pattern formation, such as the electrode area and electrolyte volume during electropolishing.

4.3.2.6. ELECTRODE SIZE VS. ELECTROLYTE VOLUME

To test the impact of the electrode size, together with the electrolyte volume, on the pattern evolution, a unitless ratio *R* is defined first,

$$R = \frac{(\text{Surface Area of the Vanadium Electrode}) / A_0}{(\text{Volume of the electrolyte}) / V_0}$$

A_0 and V_0 are the electrode surface area and electrolyte volume used in the standard experimental setup, respectively.

$R=1/2$ means the volume of the electrolyte stays the same, but the anode is half-dipped into the electrolyte. $R=2$ is achieved by bending the anode and dipping more into the electrolyte, which is equivalent to halve the volume of the electrolyte.

Results of halving anode size or halving electrolyte volume are summarized in Table 4.5 with SEM images in Figure 4.12.

Table 4.5. The impact of electrode surface area and the volume of the electrolyte on patterns' evolution.

	2.5 min	5 min	10 min
R= ½ (<i>Half Electrode</i>)	Flat (<i>sample a</i>)	Flat (<i>sample b</i>)	Pimple (<i>sample c</i>)
R= 1 (<i>Standard Setup</i>)	Flat (<i>sample d</i>)	Flat/Pimple (<i>sample e</i>)	Pimple (<i>sample f</i>)
R=2 (<i>Half Volume</i>)	Flat (<i>sample g</i>)	Pimple (<i>sample h</i>)	Pimple/Labyrinth (<i>sample i</i>)

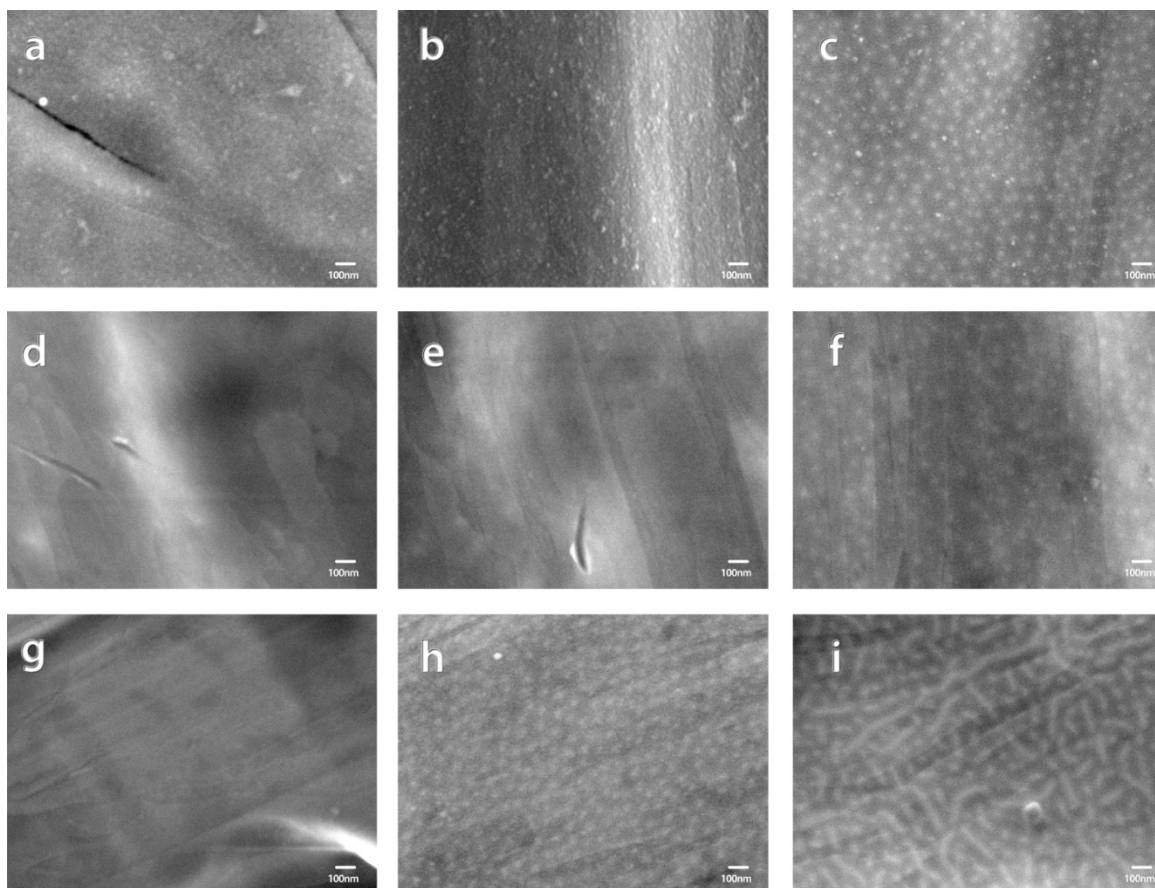


Figure 4.12. SEM images of samples in Table 4.5.

Results from R=1 (standard setup) are used as the controlled reference, against which R=1/2 and R=2 are compared. Figure 4.12a, d, g display flat surfaces. Figure 4.12b has a flat surface, however Figure 4.12e has faint pimple pattern and Figure 4.12h shows

pimple pattern. Although the pimple pattern in Figure 4.12c is more apparent than Figure 4.12f, they are the same pattern. Figure 4.12i is a mixture of pimple and labyrinth pattern.

If the electrode area is halved ($R=1/2$, the first row in Figure 4.12), it takes slightly more time to generate patterns; however, if the volume of the electrolyte is halved ($R=2$, the last row in Figure 4.12), the pattern transition appears on electrode at a much quicker pace.

4.3.2.7. AGING ELECTROLYTE

Smaller volume of electrolyte leads to a faster pattern evolution, because the electrolyte is consumed at a faster rate. To confirm this, an ‘aging’ electrolyte experiment is conducted.

Reference samples are summarised in Table 4.6, which contains two points (samples electropolished under regular conditions for 5 minutes and 10 minutes, respectively). Reference point #1, electropolished for 5 minutes, displays the pimple pattern and reference point #2, electropolished for 10 minutes, shows the labyrinth pattern.

Table 4.6 Reference samples for Aging Electrolyte Experiment

Sample	Treatment	Pattern
Reference Point #1	Electropolished for 5 minutes	Pimple
Reference Point #2	Electropolished for 10 minutes	Labyrinth

The test samples are prepared as follows.

Sample #1 is electropolished for 5 minutes. After that, the power supply is turned off and immediately switched back on. The sample continues electropolishing in the same electrolyte for another 5 minutes.

Sample #2 is first electropolished for 5 minutes as well. Then, the power supply is turned off and the sample is taken out of the electrolyte. The electrolyte is vigorously stirred for 1 minute, after which, the same sample continues electropolishing in this stirred electrolyte for 5 minutes.

Sample #3 is electropolished for 5 minutes in an electrolyte, which has already been ‘aged’ (used for electropolishing another wire) for 5 minutes.

After electropolishing for 5 minutes, sample #4 is immediately transferred into a fresh electrolyte and continues electropolishing for another 5 minutes.

After electropolishing for 5 minutes, sample #5 is thoroughly rinsed, cleaned and dried. It is then electropolished for another 5 minutes in a fresh electrolyte.

Table 4.7. Test samples in Aging Electrolyte Experiment

Sample	Treatment	Pattern
# 1	‘ON’ 5 minutes -> ‘OFF’ -> ‘ON’ 5 minutes in the same electrolyte	Labyrinth
# 2	‘ON’ 5 minutes -> ‘OFF’ 1 minute, Stir electrolyte -> ‘ON’ 5 minutes in the same electrolyte	Labyrinth
# 3	‘ON’ 5 minutes -> ‘OFF’ -> New vanadium wire ‘ON’ 5 minutes in the same electrolyte	Labyrinth
# 4	‘ON’ 5 minutes -> ‘OFF’ -> ‘ON’ 5 minutes in fresh electrolyte	Labyrinth
# 5	‘ON’ 5 minutes -> ‘OFF’, Rinse and clean sample-> ‘ON’ 5 minutes in fresh electrolyte	Labyrinth

In summary, all the test samples exhibit the same pattern (labyrinths) as reference point #2. This phenomenon is discussed below (4.4.1.2).

4.3.2.8. NATIVE OXIDE

Last but not least, the native oxide on vanadium before electropolishing also plays a role in determining patterns.

It is observed that the vanadium sample, which has been oxidized during a 15-minute sonication¹⁴⁰ in water prior to electropolishing, leads to an initial spike in the *i-t* curve (>1000 times larger than normal, Figure 4.13). The dimple pattern is formed much faster in the spike system, on the contrary, the pimple pattern is present on the sample electropolished under normal conditions.

This unwanted native oxide can greatly interfere with the pattern evolution experiment results. However, our result has shown that sonicating the sample for less than 1 minute in water can fulfil the cleaning purpose without generating the spike. Samples, sonicated in water for 1 minute, have the same pattern evolution as samples without sonication.

Sonication in acetone and methanol doesn't result in a spike.

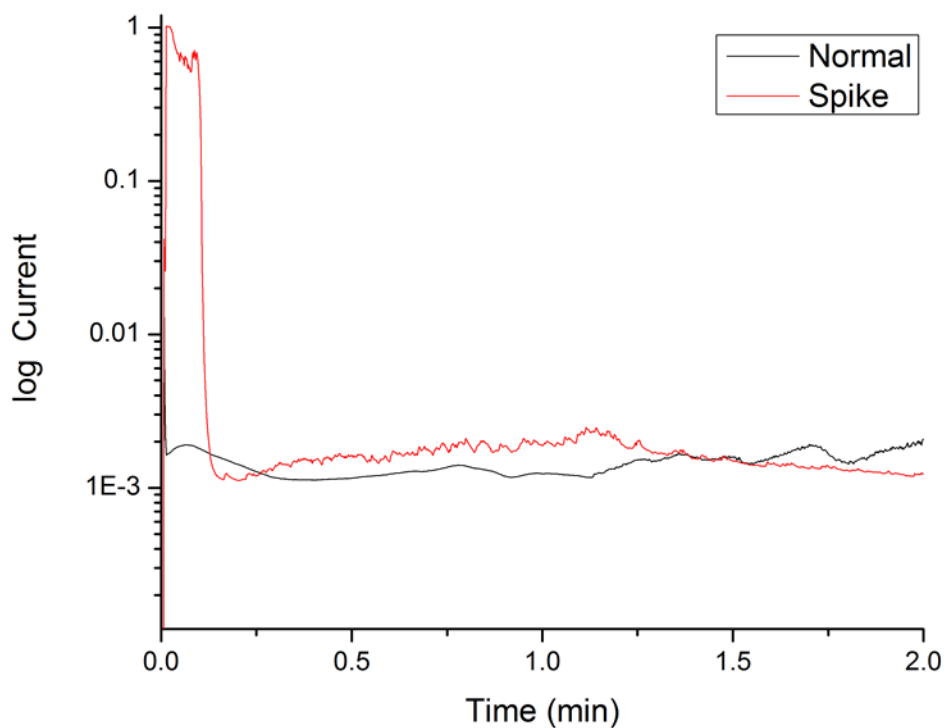


Figure 4.13. The initial current spike compared to normal current during electropolishing. The spike sample have been oxidized during the 15-minute sonication in water before electropolishing.

4.4. DISCUSSION

4.4.1. ON ELECTROPOLISHING

4.4.1.1. THE IONS FORMED DURING ELECTROPOLISHING

Vanadium has multiple oxidation states, each corresponds with a different colour (*Cf.* Table 4.1). A blue colour is observed at the anode when vanadium is electropolished in an aqueous electrolyte, which contains 25% HF, 27% H₂O, and 48% H₂SO₄. The blue colour is an indication of the formation of VO²⁺.

When electropolished in an anhydrous electrolyte, *e.g.* with at least 98% H₂SO₄, the vanadium metal is first oxidized into its highest oxidation state (V). The vanadium oxide is then dissolved into the electrolyte. The yellowish colour, both observed at the anode and detected in the *UV-vis* spectrum (Figure 4.2), confirms the formation of the VO₂⁺ ion.

4.4.1.2. MASS TRANSPORT OF VO₂⁺

At least three hypotheses have been proposed to explain the mass-transport limit during electropolishing, each differing in the mass-transport species during electropolishing: dissolved ions, or acceptor ions, or water.¹¹⁴

During the electropolishing of vanadium, a characteristic yellow colour (VO₂⁺) is observed within the vicinity of the anode. As the reaction progresses, the yellow colour slowly spreads into the bulk electrolyte. It is also noteworthy that the rate of the colour spreading also depends on the water/HF amount in the electrolyte. The higher the water/HF concentration in the electrolyte, the faster the spreading of ions, and the darker the electrolyte at the end of electropolishing. This is because VO₂⁺ is produced at a much higher rate at the anode.

It is generally accepted that dissolved ions are the mass-transport-limiting species during electropolishing.¹¹⁴ Our observation during the electropolishing of vanadium is consistent with this assertion. Due to the high viscosity of the electrolyte, the mass transport of VO₂⁺ towards the bulk solution is greatly hindered; thus, a concentration gradient of VO₂⁺ is established within the ‘viscous layer’ or ion depletion layer (Figure

4.14) adjacent to the anode. The concentration gradient is further enhanced, due to the continuous formation of VO_2^+ on the anode and the hindered diffusion of VO_2^+ into the bulk electrolyte.

During the establishment of this ion concentration gradient, different kinds of patterns, including flat surfaces, pimples, labyrinths, dimples, and random patterns, are displayed and imprinted onto the vanadium electrode surface.

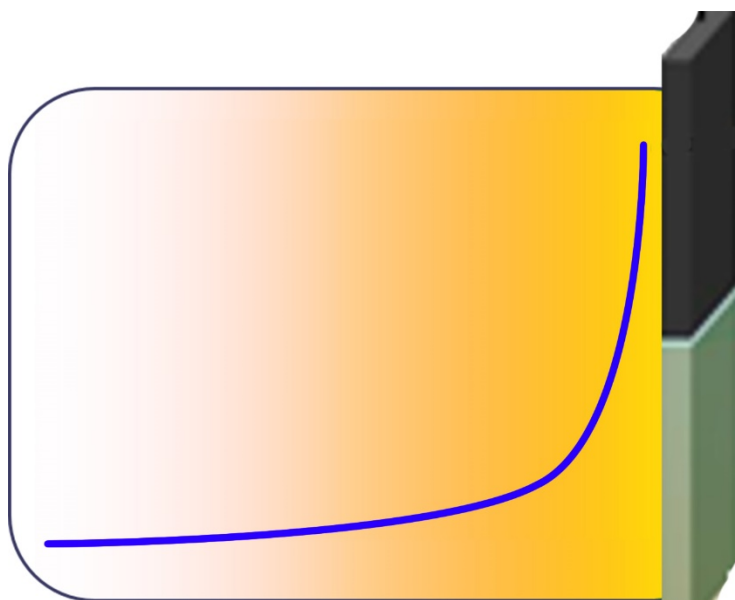


Figure 4.14. The formation of the ‘viscous layer’ during electropolishing. The blue curve indicates the relative concentration of dissolved ions, which decreases as it moves away from the anode towards the bulk electrolyte.

The dissolved-ions hypothesis is also consistent with observations made in the electrode size vs. electrolyte volume experiment, the aging electrolyte experiment, and the native oxide experiment.

In the electrode size *vs.* electrolyte volume experiment, decreasing the electrode size slows down the aging of the electrolyte. It also takes longer to establish the steady-state ion concentration gradient within the viscous layer, which slows down the pattern evolution. If the anode is reduced to a ‘point’, this greatly increases the resistance between the electrode and the electrolyte, thus there is no current. However, as the electrolyte volume decreases, it takes less time to establish the steady-state ion concentration gradient, thus pattern evolution occurs at a faster pace.

This assertion is further confirmed in the aging electrolyte experiment. If a sample, either electropolished or unelectropolished, is electropolished in an aged electrolyte, it displays a pattern which is further down in the transition line. Although electropolished in fresh electrolytes, both sample #4 and sample #5 in the aging experiment display labyrinths. Since sample #4 is not rinsed before putting into the fresh electrolyte, it is possible that it still holds the viscous layer on itself when transferred. That is why a more advanced pattern is observed. Sample #5 seems to contradict our hypothesis so far, however, it makes more sense when it is examined together with the native oxide experiment. The native oxide experiment shows that a relatively thicker layer of native oxide, caused by sonication, leads to a much higher dissolving speed initially and displays pattern evolution faster. It is possible that the oxide, formed on sample #5 after the first electropolishing, has the same poor quality as the oxide, formed after sonication. The oxide, formed after electropolishing, tends to heavily dissolve during the early stage of electropolishing; thus, the system can reach the steady-state concentration gradient faster. It is observed that samples, which have already been

electropolished, have a much higher chance of yielding spike during the second electropolishing.

The native oxide experiment may have excluded the possibility of HF and water being the limiting species, because both of them remain unchanged at the start of experiments, however a quicker pattern evolution is observed on the samples with more native oxide.

4.4.2. ON PATTERN FORMATION

Different kinds of models have been proposed to explain the nanopattern formation in electrochemical systems. A detailed review of these models has been given in Chapter 1.3. In essence, these models can be categorized into two groups, differing on the origin of the pattern formation. Anodic-oxide-based models suggest that the pattern starts within the oxide. Examples of anodic-oxide-based models include PAA, nanotubes, and nanobubbles. Whereas, liquid-phase-based models propose that patterns initiate within electrolytes and are later imprinted onto the electrode surface.

In sections below, we will scrutinize our experimental results and discuss our new findings in the context of existing models on electrochemical pattern formation, in achieving an adequate model for the nanopattern formation on vanadium *via* electropolishing.

4.4.2.1. ANODIC-OXIDE-BASED MODELS

No porous oxide (*Cf.* 1.3.1.1) nor nanotube (*Cf.* 1.3.1.3.2) is observed on vanadium at the end of electropolishing. What's more, there is no obvious charging

(3.2.3) during the SEM measurement, which further attests the metallic nature of the electropolished sample. Based on these observations, it is less likely for the pattern to be based on the anodic oxide, which has been completely dissolved during electropolishing. This seems to contradict the oxide flow model (*Cf.* 1.3.1.3.1), the nanobubble model (*Cf.* 1.3.1.3.2), the OBME model (*Cf.* 1.3.1.3.3), and the FAD model (*Cf.* 1.3.1.3.4).

4.4.2.2. LIQUID-PHASE-BASED MODELS

Liquid-phase-based models include the polar adsorbate model (*Cf.* 1.3.2.1), the crystal orientation model (*Cf.* 1.3.2.2), the reaction-diffusion model (*Cf.* 1.2.3), and the convection model (*Cf.* 1.3.2.3).

Our new findings in the vanadium pattern formation system clearly contradict the crystal orientation model, because grain boundaries have no impact on the morphology of pimples, labyrinths, and dimples. Patterns formed on vanadium are results of isotropic etching, which is typical in electropolishing.

4.4.2.2.1. Polar adsorbate model

The polarized adsorbate model (PAM) is proposed to explain the formation of stripes and dots on aluminum after electropolishing. PAM suggests that a layer of polar molecules exist on the top of the anode during electropolishing. By shielding the electrode, these molecules can modulate the dissolving speed. Due to an even distribution of these molecules (more at the protruding part than the receding part), a pattern is preserved during electropolishing.

Chang *et al.*⁹⁷ postulates that the polar molecule layer is made of organic molecules, namely, alcohols. However, he doesn't rule out the possibility of other molecules. In fact, the electrolyte used for electropolishing vanadium contains various species such as F^- , HSO_4^- , $H_3SO_4^+$, *etc.* Most of the F^- exist in the form of HF, due to the acidity of the electrolyte. As a result, the anode polar molecule layer, if it does exist, could be made of HSO_4^- .

Simulations based on the PAM have successfully validated the formation of dots and stripes on aluminum during electropolishing. The dot pattern on aluminum mimics the pimple pattern on vanadium. However, stripes are missing on vanadium; labyrinths and dimples, observed on vanadium, are missing on aluminum. Besides that, the pattern evolution on aluminum goes from stripes to dots, however, the pattern transition on vanadium occurs in an opposite direction, from pimples to labyrinths.

The PAM assumes that the pattern originates within the electric double layer and the formation of patterns is driven by the potential drop within the double layer. As a result, varying electropolishing potentials lead to pattern transitions. However, this is not the case in the vanadium pattern formation system. Instead of changing patterns, increasing potentials alters the periodicity of patterns. The higher the potential, the larger the spacing between each feature. The transition of patterns on vanadium is controlled by the composition of the electrolyte (water and/or HF) and time.

To sum up, the PAM can successfully explain the formation of various kinds of patterns during electropolishing on aluminum, which could be extended onto vanadium as

well. However, PAM is not fully compatible with the experimental observations on vanadium, largely, time evolution and the impact of potential.

4.4.2.2.2. Reaction-diffusion model

The reaction-diffusion pattern (Turing pattern) in electrochemistry results from the interplay of activators and inhibitors. Since inhibitors diffuse at a slightly faster rate than activators, it can pre-pattern the surface.

However, determined by the diffusion co-efficient of products and reactants, the length scale of the Turing pattern in the electrochemical system should be larger than one micrometer²⁶, which contracts the nano-scale pattern formation in the vanadium system. Besides that, Turing pattern model predicts that patterns, achieved under potentiostatic conditions, may appear differently from galvanostatic-model patterns²⁶, however, this is not observed in the vanadium system. As a result, Turing pattern can explain the formation of micrometer-scale electrochemical patterns. It might be a stretch to explain the pattern formation at nanoscale.

4.4.2.2.3. The convection model

The convection model suggests that during electropolishing, the double layer breaks into small convective cells to assist the mass transport of ions. The size of these convective cells is equal to the thickness of the electrochemical double layer and the size of patterns imprinted on the electrode. Convective cells at the microscale or larger have been observed in electrochemical systems.³⁶ The formation of dimples on tantalum,

titanium, tungsten, and zirconium is due to convective cells formed within the electric double layer.⁶²

The formation of convective cells is governed by the Rayleigh number, a ratio of driving force over retarding force. If driving force is too weak, there is no pattern on the surface. Only when the Rayleigh number falls within a certain range, certain types of patterns occur on the surface. If the Rayleigh number is too large, the system turns chaos.

The Rayleigh number can be used to explain the formation of different types of patterns during electropolishing of vanadium. The VO_2^+ concentration gradient within the viscous layer acts as the driving force for mass-transporting dissolved ions. Different concentration gradients, perceived at different time intervals, leads to different kinds of patterns, from a flat surface (low Rayleigh number), to pimple pattern, to labyrinth pattern, to dimple pattern, and finally to a chaotic random pattern (Rayleigh number is too high). It is possible that different concentration gradients are linked to different arrangements of convective cells, which eventually leads to different patterns.

The ion concentration gradient within the viscous layer is influenced by the chemical composition of the electrolyte. If more HF or water is present in the electrolyte, which means a higher dissolving speed at first, the pattern-forming concentration gradient will be established at a faster pace. This also explains why the pattern evolution is occurring at a quicker pace, if electropolishing is carried out in a small electrolyte volume system (*Cf.* 4.3.2.6) and a spike system (*Cf.* 4.3.2.8), because they accelerate the setup of the ion concentration gradient.

Our experimental results have shown that the electropolishing potential has no impact on the pattern selection, rather it alters the periodicity of patterns. This is because the electropolishing potential can modulate the thickness of the viscous layer and indirectly control the size of convective cells and the size of patterns left on the electrode surface.

In summary, the convection model is largely consistent with our findings in the vanadium pattern formation system. Electrolyte composition, electropolishing potential, and time have impacts on the formation and morphology of patterns. However, a quantitative model for convection-based pattern formation is still missing.

4.4.3. PATTERN FORMATION IN A BASIC ELECTROLYTE

Patterns, discussed above, occur in an acidic and highly viscous electrolyte. Since the pattern formation during electropolishing is a universal process, it should be possible to reproduce patterns in different electrolytes, as long as the requirement on concentration gradient within the viscous layer is satisfied.

A somewhat disordered dimple pattern (Figure 4.15) has been achieved on vanadium after the sample is electropolished at 10V in 2.4M aqueous NaOH for 1 minute. If electropolishing is carried out at higher potentials ($>15\text{V}$), the whole wire dissolves within seconds.

The electropolishing time required in this basic electrolyte is considerably less than that in the $\text{HF-H}_2\text{SO}_4$ electrolyte. Besides that, the electropolishing potential is also lower. This is because 2.4M NaOH is much more conductive compared to $\text{HF-H}_2\text{SO}_4$,

which translates into a much higher current density during electropolishing and a quicker establishment of the concentration gradient within the viscous layer.

It is also noteworthy that in order for the pattern to occur in the basic electrolyte, the vanadium wire needs to be polished with sand paper first to remove the native oxide. This is probably because vanadium native oxide doesn't dissolve in NaOH as well as in HF. Once the native oxide is removed, water can oxidize metal and NaOH can dissolve the anodic oxide at a much higher rate. This is another indication that the dissolution of ions participates in the pattern formation.

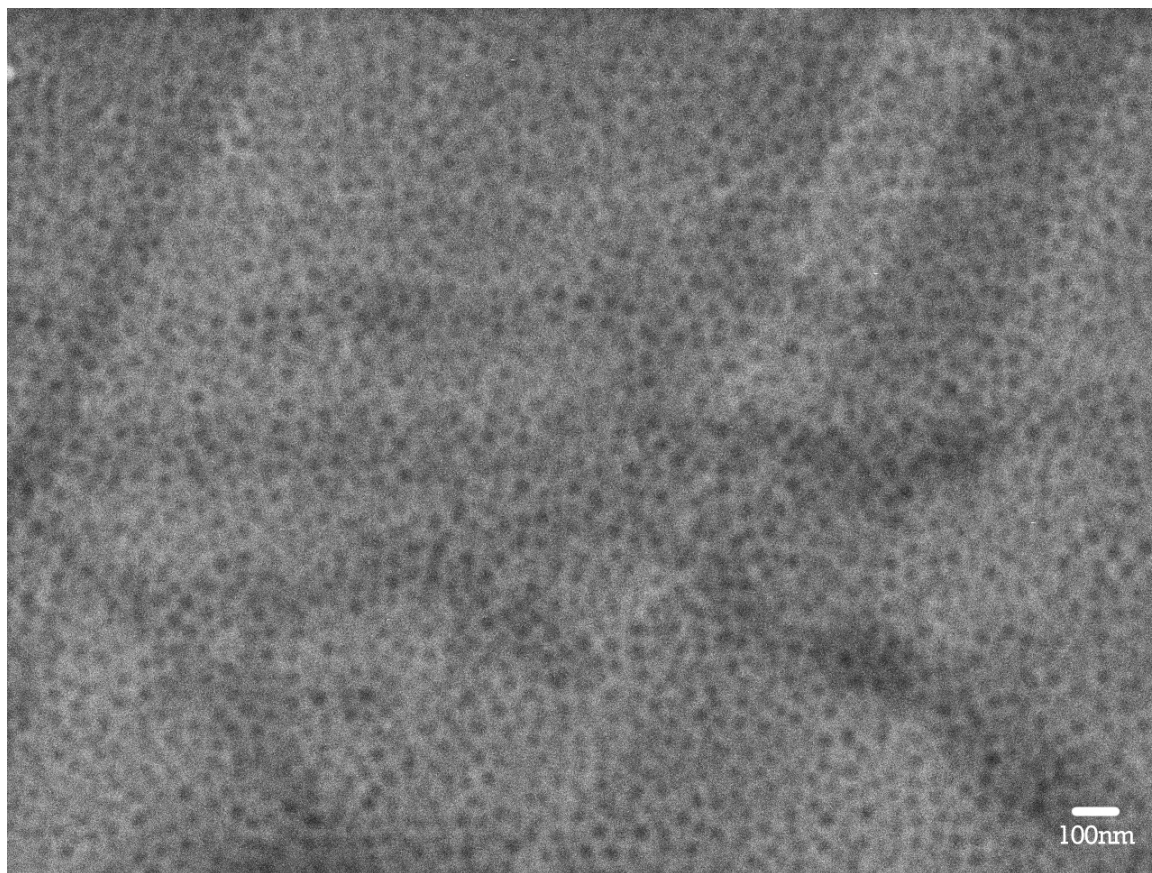


Figure 4.15. The nanoscale pattern formed on vanadium upon electropolishing at 10V in 2.4M NaOH for 1 minute.

4.5. CONCLUSION

Different kinds of patterns at nanoscale (flat surface, pimples, labyrinths, and dimples) have been discovered on vanadium after electropolishing. The formation of these patterns is extremely sensitive to the electrochemical conditions, under which they are prepared, such as electrolyte compositions, electropolishing potential, and electropolishing time. A little variance in the electrolyte composition leads to the pattern transition, until the patterns are replaced with chaotic features. The periodicity of nanopatterns is dependent on the electropolishing potential. The higher the potential, the larger the periodicity.

A time evolution of patterns is also observed on the electropolished samples: from a flat surface to pimples to labyrinths to dimples and finally to random features. The pace of this pattern evolution is impacted by the volume of the electrolyte, the size of the electrode, the aging of the electrolyte, and the amount of ion dissolved initially.

The formation of nanopatterns during electropolishing is a universal process, *i.e.* it is not limited to a specific combination of metal and electrolyte. Disordered dimple pattern has been achieved on vanadium in a basic electrolyte.

Upon comparing our findings with existing models on pattern formation in electrochemical systems, the polar adsorbate and the convection model arise as the best candidates to explain the nanopattern formation, transition, and evolution on vanadium.

CHAPTER-5

FORMATION OF NANOTUBES AND NANOPATTERNS ON TANTALUM

5.1. INTRODUCTION

Nanopatterns achieved *via* electrochemical methods can be mainly divided into two groups: oxide pattern and metallic pattern. Porous anodic alumina⁸⁴ (PAA) and nanoporous anodic titanium⁷¹ are examples of patterns based on oxides, whereas, the dimples^{102, 103}, as well as pimples and labyrinths aforementioned in Chapter 4, belong to the latter. The electrochemical processes, which lead to the oxide pattern and metallic pattern, are also different. The electrochemical treatment for PAA and nanoporous anodic titanium is called anodization. It leaves a layer of anodic oxide on the surface, which is thicker than the native oxide. Unlike anodization, electropolishing dissolves the anodic oxide, ending up with a levelled surface covered with native oxide.

Different kinds of models, either based on anodization or electropolishing, have been proposed to explain the formation of dimple pattern on tantalum. The anodization model suggests that a layer of porous oxide forms on the metal surface at the start of anodization. Due to the field focusing effect^{83, 91}, the oxide formation/dissolving speed is higher at the base of pores than at the top. As a result, pores are etched deeper and deeper, thus creating the nanotube pattern. The incorporation of fluoride ions into nanotubes destabilizes nanotubes, which will detach off the surface. The partial or complete dissolution of these nanotubes exposes the dimple pattern.⁹¹

Electropolishing-based models assume that the pattern formation originates within the electrolyte. The polar adsorbate model (PAM) suggests that the pattern formation is driven by the potential drop within the double layer, because the electric field is higher at the protruding (maximum) part than the receding (minimum) part. A higher electric field means a higher adsorption rate of polar molecules, a condition which can in turn shield the electrode from dissolution. The difference between dissolving speeds leaves the pattern on the metal surface. The convective electropolishing model proposes that ions are depleted (or saturated) within the viscous layer, which will be compensated by the convection of ions from (or into) the bulk solution. The formation of these microscale convective cells has been visualized. Dini *et al.*³⁶ reports the formation of convective cells between the two electrodes kept 60 μ m apart. The size of features imprinted on the electrode is on the same scale as the size of convective cells. It is postulated that the formation of nanoscale convective cells leaves the dimple pattern on tantalum, titanium, *etc. via* electropolishing.

In this chapter, we look into the formation of oxide nanotubes and dimples on tantalum *via* electrochemical methods and confirm the metallic nature of the dimple pattern and oxide nature of nanotubes. The formation of nanotube pattern can be interpreted from the chronoamperometry curve. A quantitative analysis of the nanotube and dimple coverage shows that the formation of nanotubes is dependent on the composition of the electrolyte as well as the time dipped in the electrolyte after electropolishing. A phase diagram is generated to visualize the impact of the electrolyte

and a time series study has been conducted to demonstrate the sensitivity of nanotubes in the HF based electrolyte.

All the experiments in this chapter are carried out by the author, unless otherwise specified.

5.2. EXPERIMENTAL

Tantalum, coming from the Greek *Tantalus*, is a grayish and very soft metal, with a high melting point of 2996°C.¹³⁶ However, tantalum is most famous for its corrosion resistance. Protected by a thin (around 5 nm) layer of passivating Ta₂O₅, tantalum is inert to almost all chemicals at room temperature, except hydrofluoric acid (HF).¹³⁶

As a result, an electrolyte mixed with concentrated sulphuric acid and HF is chosen for electropolishing tantalum. Previous work in our group has shown that if electropolishing is carried out in a 9:1 volumetric ratio sulphuric acid/HF electrolyte, a hexagonally-close-packed nanopattern, dimple pattern, can be achieved on tantalum.¹⁰²

Prior to electropolishing, tantalum wire (99.98%, 0.25mm diameter, Alfa-Aesar) is cut into 2.5 cm long pieces and ultrasonicated in acetone (HPLC, Caledon), methanol (HPLC, Caledon) and Millipore water (18.2 MΩ•cm), respectively. Tantalum wire is chosen as the anode throughout this chapter unless stated otherwise, where tantalum foil (99.99%, 0.127 mm thick, Alfa-Aesar, cut into 0.5 cm x 2 cm) is used.

The electrolyte is prepared by mixing HF (48.5% wt., EMD) with H₂SO₄ (96.2% wt., Caledon) and further with oleum (20% free SO₃, Sigma Aldrich). The electrolyte is

stirred vigorously over night before usage. All apparatuses in contact with the electrolyte are made of PTFE.

The experimental setup is described in Chapter 2 (Figure 2.1). For the tantalum wire experiment, 4mL of fresh electrolyte is used, unless otherwise specified. The counter electrode is a Pt/Ir loop (3cm in diameter) and is attached to the cathode alligator clip. The tantalum wire is attached to the anode alligator clip, the vertical position of which is precisely controlled by a stage controller. Initially positioned at the center above the cathode loop, the tantalum sample is perpendicularly brought down to touch the bottom of the PTFE beaker.

In the tantalum foil experiment, both the Pt/Ir wire cathode and the tantalum foil are dipped 1 cm into the electrolyte. The distance between the working and counter electrodes is kept at approximately 1.5 cm. The volume of the electrolyte is 30 mL.

All the experiments are performed at room temperature. No attempt is made to thermostat the electrolyte.

The power supply is an Agilent E3617A and the multimeter is an HP 34401A. Immediately after electropolishing, the sample is thoroughly rinsed with Millipore water and dried in air.

SEM images are taken by a JOEL-7000F and a Leo-1530. AFM images are taken by a Veeco Enviroscope with a Nanoscope IIIa controller and Veeco TRESP p-doped Si tips with a nominal radius of less than 10 nm.

5.3. RESULTS

5.3.1. FORMATION OF TANTALUM DIMPLE ARRAY AND NANOTUBES

Two types of patterns can be observed, dimple pattern and nanotubes. Dimple patterns are formed *via* electropolishing, whereas nanotubes are products from anodization.

A large-scale SEM image (Figure 5.1a) of the dimple pattern (Figure 5.1c) shows that the substrate is levelled at the micrometer scale after electropolishing with clearly visible grain boundaries. Grain boundaries have no impact on the morphology of dimples, which is called isotropic electropolishing.

Figure 5.1b shows the formation of nanotubes on tantalum. These nanotube arrays start to peel off the surface. Figure 5.1d is a zoom-in image of tantalum oxide nanotubes, which collapse into clusters. In-between the gaps, dimples can be observed.

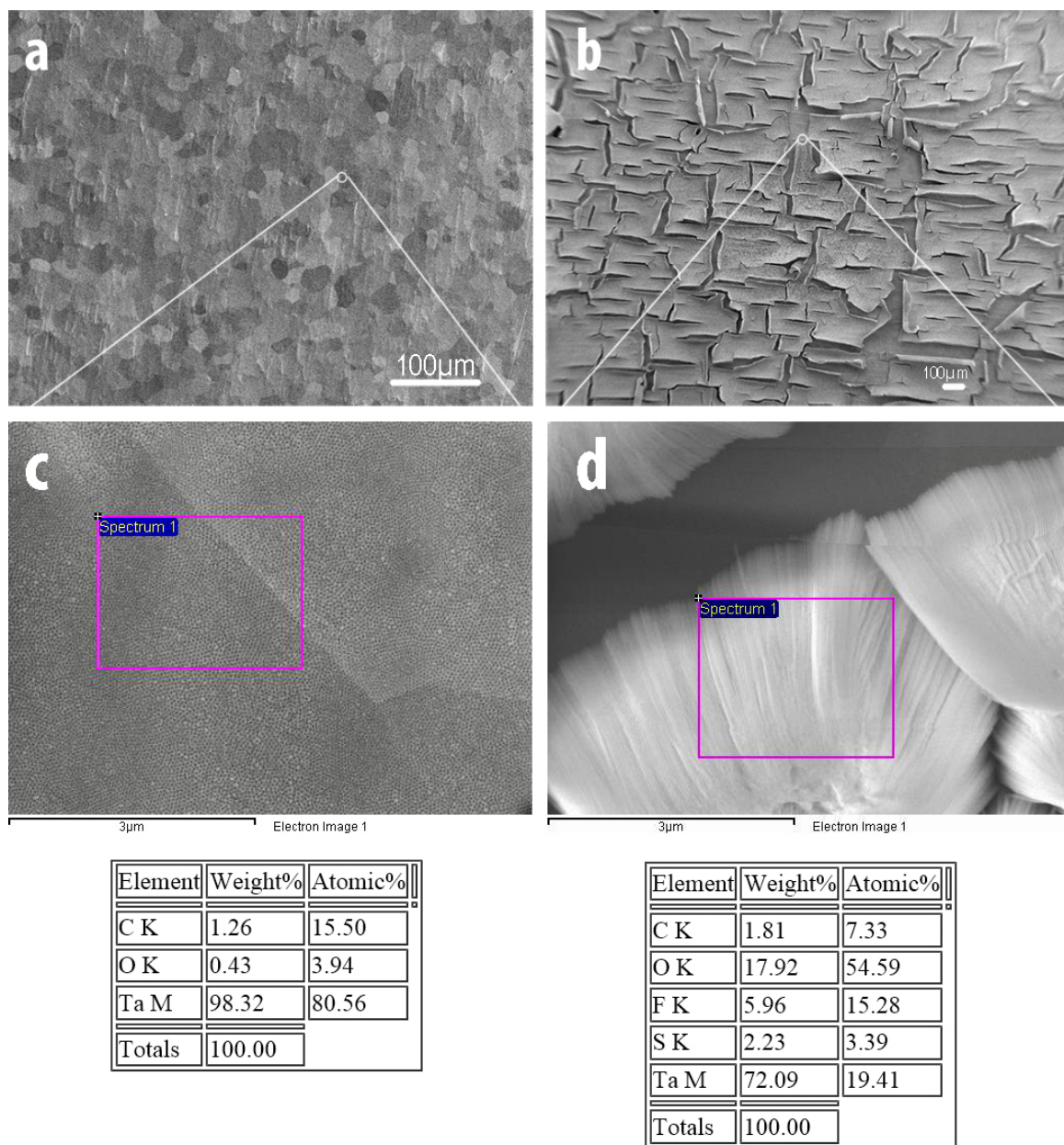


Figure 5.1. Large-scale and zoomed-in SEM images of dimple pattern (a, c) and nanotubes (b, d) and their EDX analyses.

5.3.2. METALLIC DIMPLES VS. OXIDE NANOTUBES

The EDX spectrum of the purple area in Figure 5.1c shows that only a small amount of oxygen (3.94%, atomic percentage) is present on the dimple pattern. In

contrast to that, the EDX spectrum of the purple area on nanotubes shows that nanotubes on tantalum are Ta_2O_5 . The atomic ratio of tantalum over oxygen is roughly 2:5 (Figure 5.1d and accompanying EDX).

However, the EDX technique in SEM imaging is not surface sensitive when it comes to quantifying surface compositions, because the EDX signal could originate up to several micrometers beneath the sample surface (*Cf.* 3.2.4). One could argue that the low oxygen concentration in EDX of Figure 5.1c is artificially caused by the strong tantalum signal from the bulk.

To quantify the oxide amount on dimples, a cross-sectional image of the dimple pattern is taken by transmission electron microscopy (TEM), as shown in Figure 5.2. The high resolution TEM image confirms that each dimple has a depth of 8~10 nm, with a lateral periodicity of about 55 nm. Dimples are covered by a thin layer (4~5 nm) of oxide, the thickness of which doesn't vary for the top and the bottom. Besides that, an electron energy loss spectroscopy line-scan in Figure 5.2a gives the elemental information, which shows that S and F are below the detection limit, whereas there is a brief oxygen signal at the start of the oxide layer. The electron diffraction pattern confirms the metallic crystalline nature of tantalum (Figure 5.2b), whereas the tantalum oxide layer is proven to be polycrystalline (Figure 5.2c).

Results from HR-TEM measurement indicate that the oxide covering the dimple pattern after electropolishing is no thicker than the native oxide, *i.e.*, no additional oxide has been created on tantalum at the end of electropolishing as opposed to anodization.

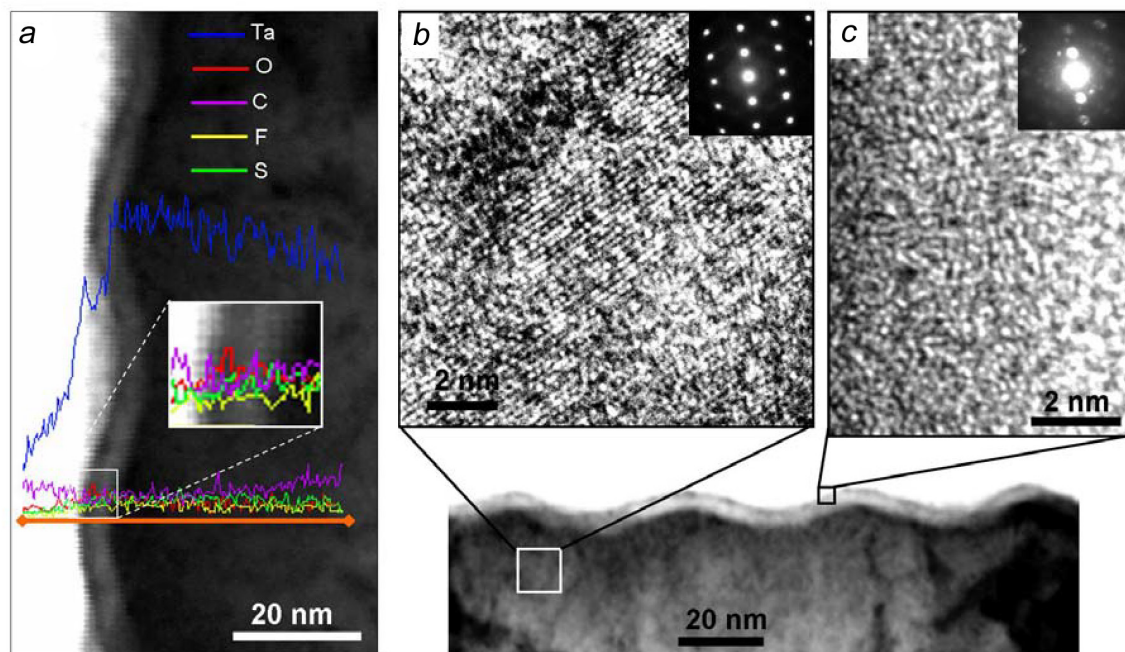


Figure 5.2. TEM images of dimples on tantalum (a) EELS line-scan of dimples on tantalum (b) TEM image of the base of dimples and the electron diffraction pattern (c) TEM image of the oxide layer and the electron diffraction pattern. (Data taken by Dr. Sherdeep Singh)

5.3.2.1. SIZE VARIANCE OF DIMPLES

Large-scale SEM (Figure 5.3) shows that the size of dimples is not uniform across the surface, which range from 10 nm to 60 nm. The periodicity of the size modulation is about 1 micrometer. The grain boundary has no impact on this size variance. The size variance is observed in both potentiostatic and galvanostatic modes.

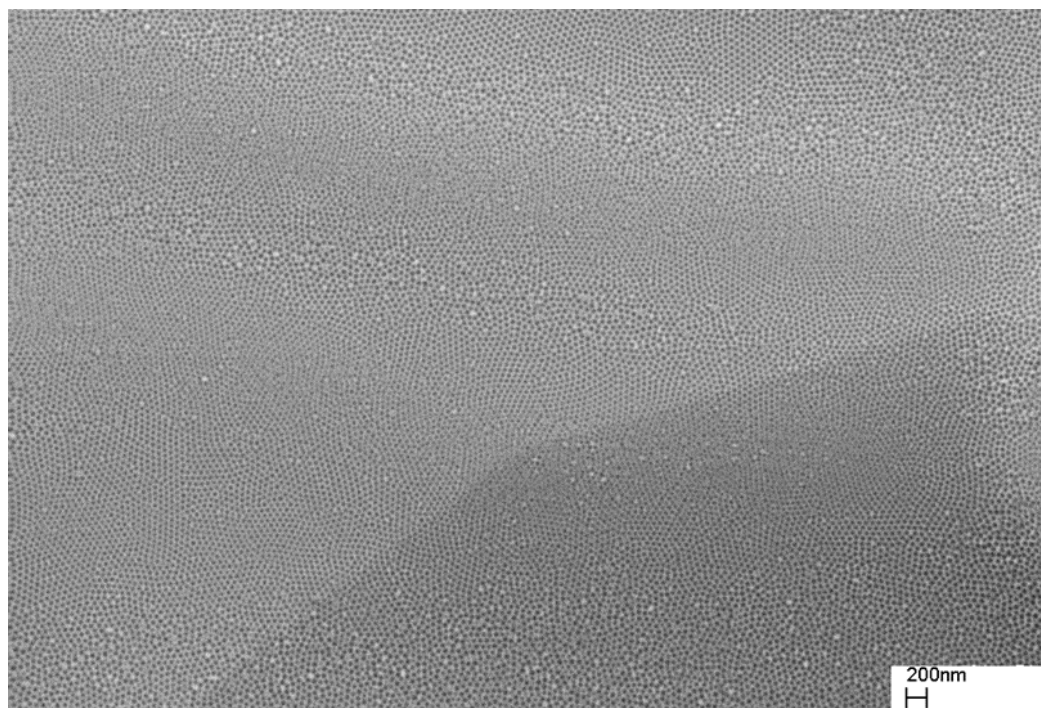


Figure 5.3. Large-scale SEM image shows the size modulation of dimples of tantalum electropolished for 5min.

Height information is missing in the SEM image. The relative height of dimples is revealed by AFM (Figure 5.4), which indicates that dimples are slightly larger at the ‘valley’ than at the ‘top’. A profile of a dimple (Figure 5.4A) at the ‘valley’ shows a radius of 32 nm with a depth of 5.9 nm, while a ‘top’ dimple (Figure 5.4B) has a radius of 26 nm and a depth of 4.5 nm.

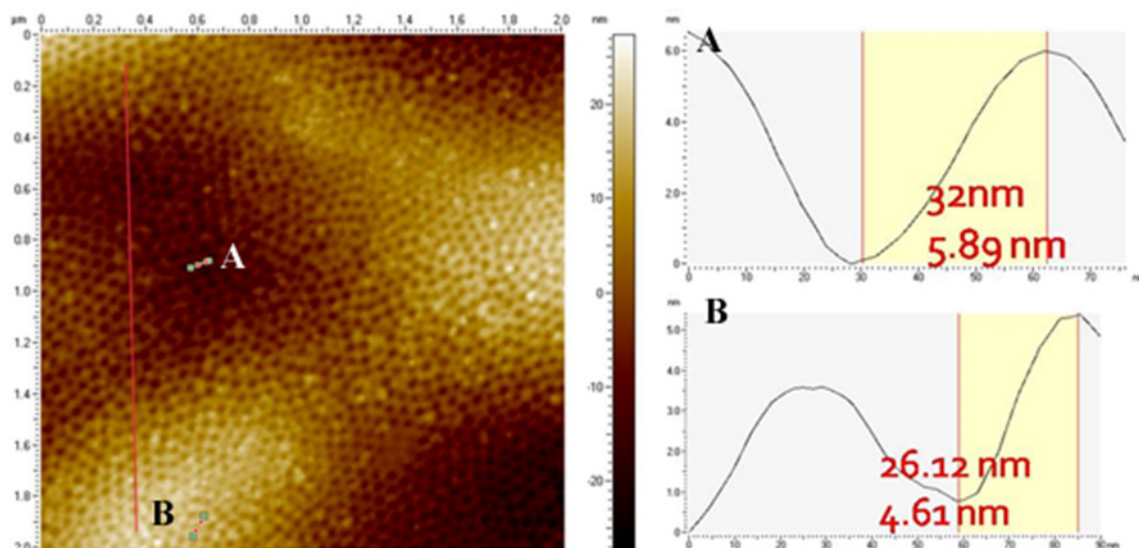


Figure 5.4. AFM image of dimple size variance on electropolished tantalum, with profiling at spot A and B.

Besides the micrometer-scale topography, there are other factors that affect the size of dimples, *e.g.* the electropolishing potential¹⁰³ and the electrochemical reaction rate on the electrode, which can be monitored in a galvanostatic experiment.

This experiment is carried out using tantalum sheet. If the current is too low (Figure 5.5a), there are no nanoscale features on the surface. When the current reaches 40mA/cm² (Figure 5.5b), diffusion is no longer sufficient for the mass transport of ions. As a result, disordered dimples appear on the surface. Dimples continue to improve in shape and order (Figure 5.5c), until an optimum current is reached (Figure 5.5d). If the current density is further increased, dimples become much shallower (Figure 5.5e) or missing (Figure 5.5f), indicating that the oxide dissolving speed falls behind the forming speed. It is also observed that higher current density leads to larger dimples, until the current density reaches the optimal current density (Figure 5.5b, c, d, and e).

It is observed that the dimple pattern only occurs within a small range of current density and potential. The potential for the $100\text{mA}/\text{cm}^2$ sample ranges from 12V to 16V, which is also the optimum potential range for dimple formation under potentiostatic condition. The current density for 15V sample under potentiostatic experiment ranges from $80\text{mA}/\text{cm}^2$ to $120\text{mA}/\text{cm}^2$. There is no visible difference between the dimple patterns produced under potentiostatic and galvanostatic conditions.

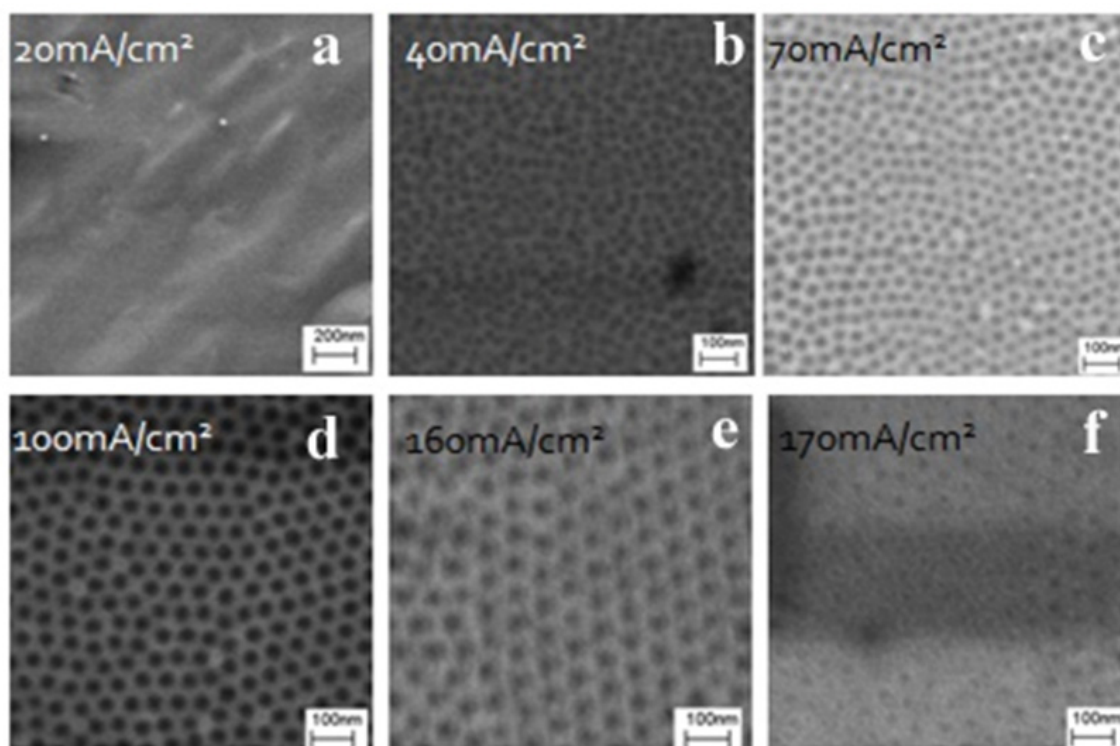


Figure 5.5. SEM images of the surface morphologies on the electropolished tantalum at current density of $20\text{ mA}/\text{cm}^2$ (a), $40\text{ mA}/\text{cm}^2$ (b), $70\text{ mA}/\text{cm}^2$ (c), $100\text{ mA}/\text{cm}^2$ (d), $160\text{ mA}/\text{cm}^2$ (e), $170\text{ mA}/\text{cm}^2$ (f).

5.3.2.2. DIFFERENT PATTERNS?

Vanadium has displayed various kinds of patterns after electropolishing. However, the dimple pattern is dominant on tantalum. Only under certain circumstances

(2% HF and 2% water), is it possible to observe different kinds of patterns (Figure 5.6) on samples electropolished for 1 hour or longer. However, the formation of these patterns lacks reproducibility. It is possible that the formation of various kinds of patterns accompanies the formation of nanotubes. Nevertheless, the formation of nanotubes obstructs the observation of these patterns. With nanotubes dissolved, patterns evolve.

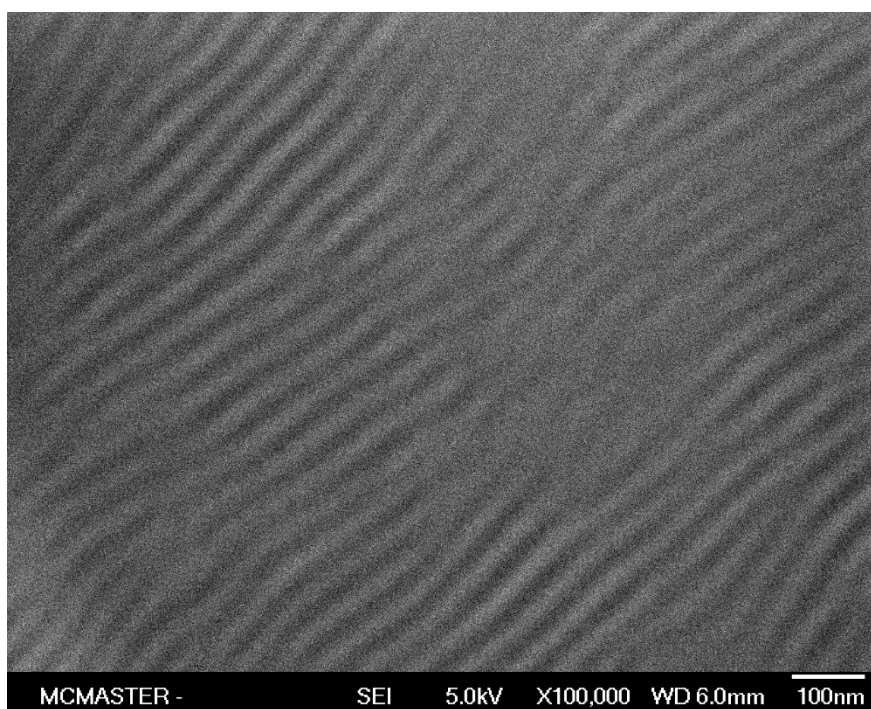


Figure 5.6. The formation of stripe pattern on tantalum.

5.3.3. CHRONOAMPEROMETRY OF DIMPLES AND NANOTUBES

The formation of the dimple pattern or nanotubes can be interpreted *in-situ* from the *i-t* curve (Figure 5.7a). The current density for the dimple pattern is about twice higher than that of nanotubes. The *i-t* curves 1, 2, 3 correlate with sample b (Figure 5.7b), sample c (Figure 5.7c), and sample d (Figure 5.7d), respectively. The mass-transport-limit current of the dimple pattern is twice as much as that of nanotubes (Figure 5.7a). This

phenomenon occurs because the nanotubes, formed between the metal and the electrolyte, are oxide and behave as ohmic resistors, which lowers the overall current density.

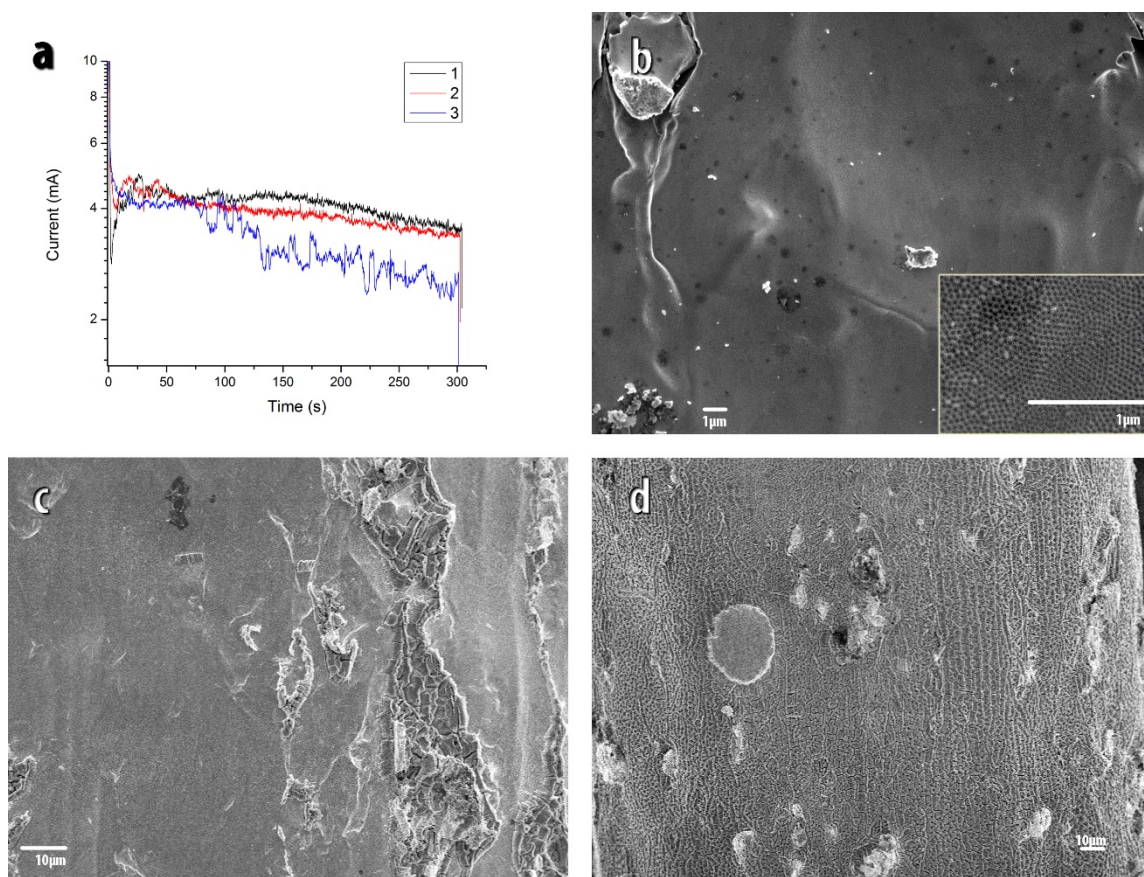


Figure 5.7. The formation of tantalum oxide nanotubes as water concentration increases and their corresponding i - t curve. Curve 1 is for sample b; 2 for c; 3 for d, respectively.

5.3.4. ELECTROLYTE'S IMPACT ON DIMPLES VS. NANOTUBES

5.3.4.1. WATER

The formation of dimples and nanotubes is controlled by the amount of water in the electrolyte (Figure 5.7). Detailed electrolyte compositions for samples in Figure 5.7 are summarized in Table 5.1. The concentration of HF is kept constant in all electrolytes. Water concentration increases from 8% to 9% and finally to 11%, the concentration of

H₂SO₄ decreases in compensation. As the water concentration increases through sample b to d (Figure 5.7), the amount of nanotubes left on the sample increases as well.

Table 5.1. The composition of electrolyte in Figure 5.7

	Sample b	Sample c	Sample d
HF %	8%	8%	8%
H₂O %	8%	9%	11%
H₂SO₄ %	84%	83%	81%

5.3.4.2. HF

Water facilitates the formation of nanotubes, whereas HF dissolves them. To estimate the dissolution speed of nanotubes, samples covered with same amount of nanotubes are left in electrolytes for different lengths of time.

All the four samples in Figure 5.8 have received the same treatment, except that sample a is rinsed immediately, whereas samples b to d are left in the electrolyte for 15 seconds, 4 minutes, and 3 hours, respectively before rinsing. The majority of sample a (Figure 5.8a) is covered with nanotubes; whereas sample b (Figure 5.8b) is mostly covered with dimples with a small amount of nanotubes found in between the ‘cracks’; sample c (Figure 5.8c) has the dimple pattern, but no nanotubes; sample d, after being left in the electrolyte for 3 hours, has neither dimples nor nanotubes.

In summary, HF can dissolve most of the nanotubes within tens of seconds. If time is long enough (>3 hours), HF can etch away the dimple pattern as well.

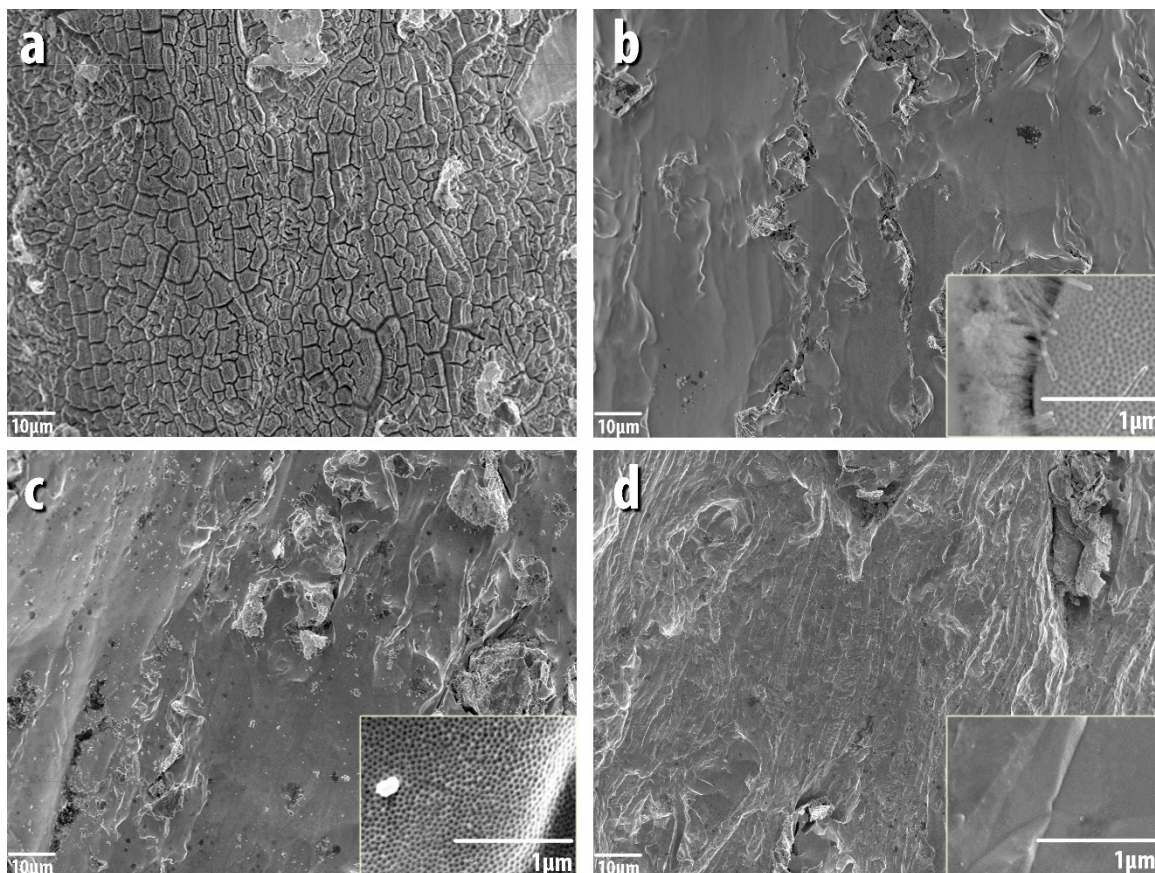


Figure 5.8. Large scale and zoomed-in (inserts) SEM images of samples dipped in electrolyte for 0 seconds (a), 15 seconds (b), 4 min (c), and 3 hours (d) after electropolishing.

5.3.5. QUANTIFYING THE AMOUNT OF NANOTUBES

It is necessary to quantify the amount of nanotubes left on the sample surface after anodization.

To achieve this goal, a large-scale SEM image (Figure 5.9a) is first converted into a binary image (Figure 5.9b), with colour black assigned to nanotubes. ImageJ ‘Area Measurements’ of the binary images conclude that 87.0% of Figure 5.9a is covered with nanotubes whereas in Figure 5.9c, the ratio is 24.7%.

The detailed ImageJ commands used are: ‘Make Binary’ and ‘Analyze Particles’.

The area percentage value is displayed in the ‘Summary’ window.

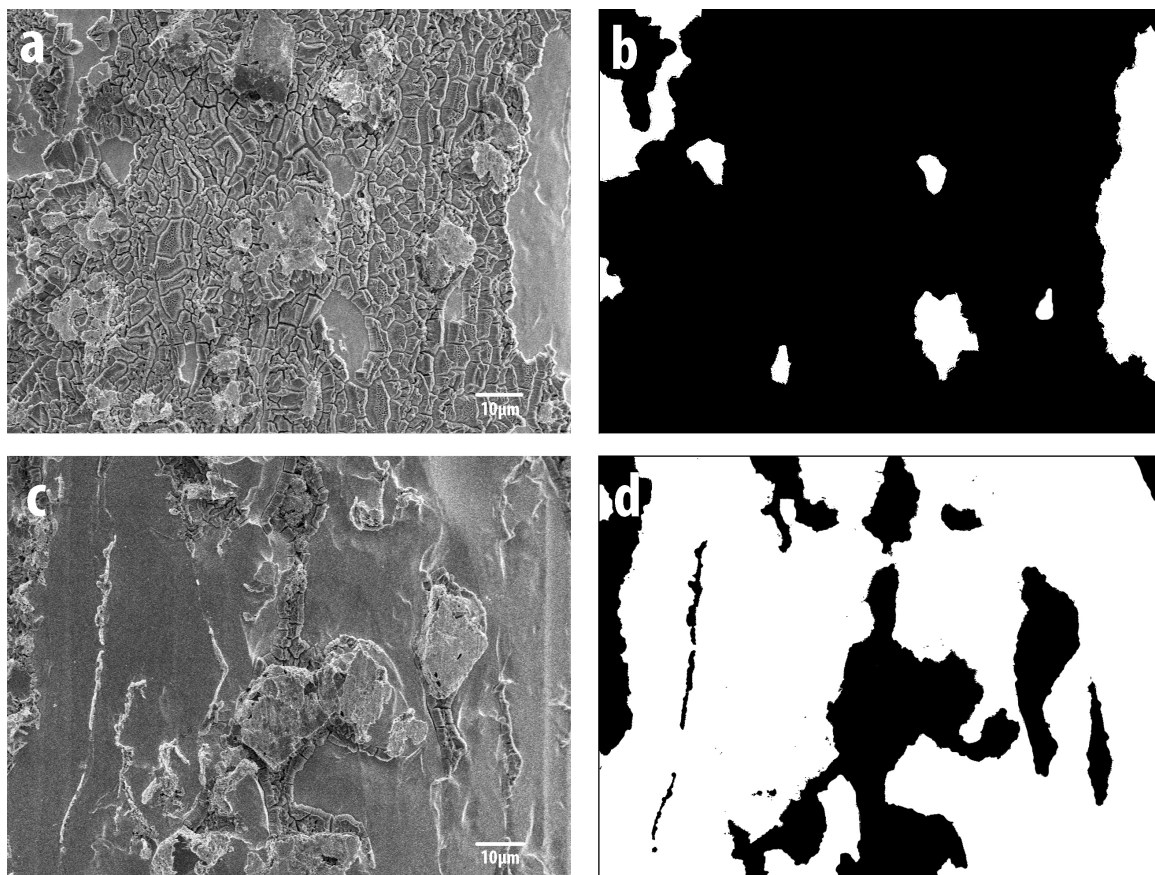


Figure 5.9. SEM images of dimple pattern with nanotubes and their binary figures, black: nanotubes, white: dimple pattern.

5.3.6. PHASE DIAGRAM – H₂O VS HF

After obtaining the surface coverage ratio, it is possible to plot a phase diagram (Figure 5.10) to demonstrate the impact of HF and water on the formation of nanotubes.

The red area in the phase diagram is not accessible with chemicals available. A flat surface is found on samples from the yellow area. The pink area at the top right corner indicates that the whole sample is dissolved in less than 20 seconds, thus no

samples can be studied at 5-minute interval. Three kinds of blue, from lightest to darkest, refer to dimpled surfaces with no nanotubes or with coverage of less than 1% (*e.g.* Figure 5.8*c*), with coverage between 1% and 75% (*e.g.* Figure 5.8*b*), and with nanotube coverage of higher than 75% (*e.g.* Figure 5.8*a*).

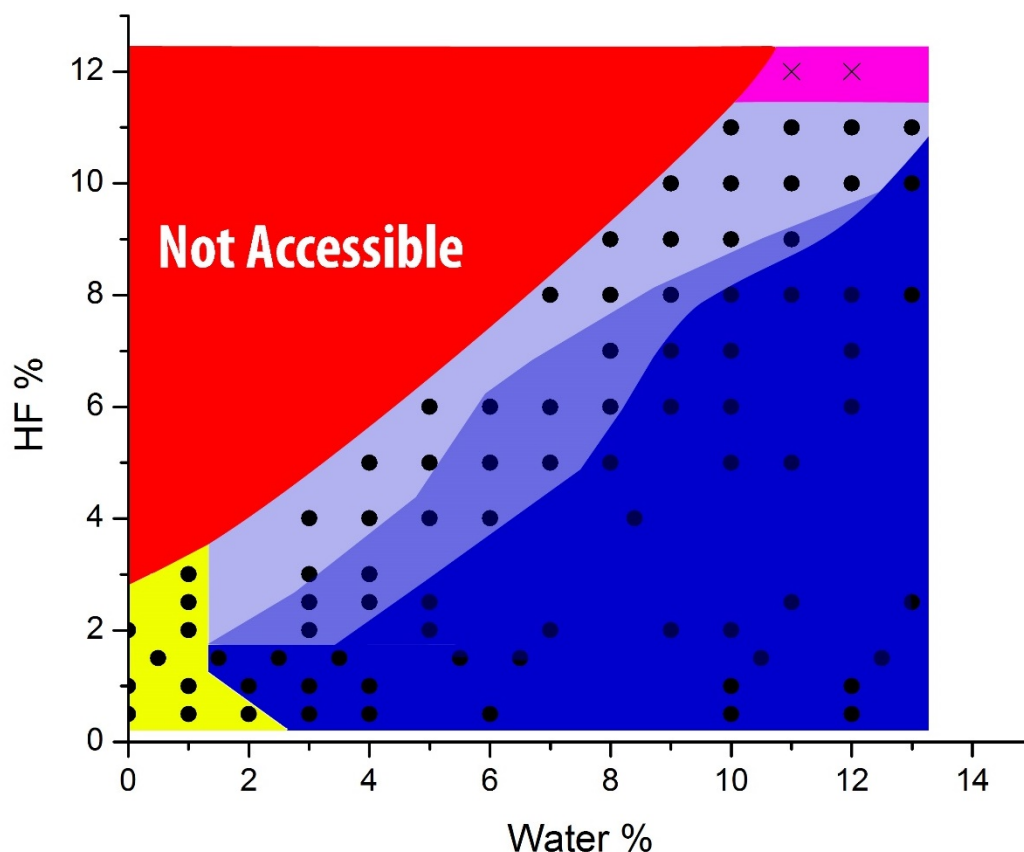


Figure 5.10. Phase diagram showing the formation dimple pattern and nanotube subject to the water and HF concentration in the electrolyte.

A flat surface (yellow in Figure 5.10) is achieved if both the HF and water concentration are low enough (HF less than 3% and water less than 1%). At low HF concentration (less than 1.5%), addition of water in the electrolyte creates nanotubes (dark blue in Figure 5.10). A same trend is observed at high HF concentration; however, a

different phase (dimples without nanotubes, light blue in Figure 5.10) exists before the formation of nanotubes.

5.4. DISCUSSION

5.4.1. COMPARISON WITH THE VANADIUM SYSTEM

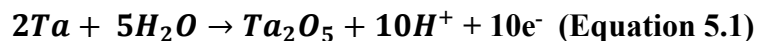
The pattern formation in the tantalum system occurs in a region far from the vanadium system. HF and water concentration in the vanadium system range from 0 to 2 percent. Electropolishing tantalum using the conditions from that region gives no pattern.

The periodicity of patterns on vanadium is consistent across the whole sample. However, the size of dimples varies on tantalum and is subject to microscale surface morphology. Dimples are bigger at the bottom of valleys and smaller at the top.

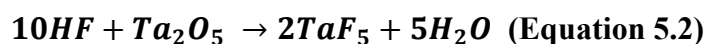
No noticeable difference is observed between the different electropolishing modes: potentiostatic and galvanostatic. The size of dimples is also influenced by the current density at which they are fabricated. If the current density is low enough, there is no pattern on the surface. Dimples occur within a range of current densities. If the current density is too high, the dimple pattern is erased. This observation is consistent with the Rayleigh number in convection model above (*Cf.* 4.4.2.2.3).

5.4.2. PHASE DIAGRAM

However, the nanotube array is only observed in the tantalum system. As shown in the water varying experiment (5.3.4.1), increasing water concentration in the electrolyte leads to the formation of nanotubes.



On the other hand, HF in the electrolyte dissolves the nanotubes formed (Equation 5.2). This is why dimple pattern is observed in low water concentration and from medium to high HF concentration. This is consistent with other researchers' observations that the formation of nanotube depends on the ratio of water and HF in the electrolyte.⁷⁶



5.4.3. DIMPLE OR NANOTUBE?

Whether dimples are the precursor of nanotubes or vice versa remains in question. In light of our new findings, given the high dissolving speed of nanotubes in HF-H₂SO₄, it is likely that nanotubes are also dissolved *in-situ* during electropolishing. The net difference between the nanotube forming speed and dissolving speed determines whether or not nanotubes will be left on the sample. The nanotube forming speed is linked to the water concentration in the electrolyte; whereas the dissolving speed is related to the HF concentration in the electrolyte.

5.5. CONCLUSION

Nanotubes have been found on electrochemically treated tantalum. It is found that the formation of these nanotubes is dependent on the water and HF content in the electrolyte. An HF-water-pattern phase diagram shows that at low-water concentrations, only the dimple pattern is left on the electropolished surface. As the water concentration increases, parts of the dimple pattern is replaced by nanotubes until the whole surface is covered with nanotubes.

The size of dimples is influenced by the local height on samples and the current density during electropolishing. It is also possible to achieve different arrangements of patterns on tantalum, if the sample is electropolished for a longer period of time, given that the pattern is not blocked nanotubes.

CHAPTER-6

NANO-PATTERNING A BIOMEDICAL ALLOY (Ti-6Al-4V) VIA ELECTROPOLISHING

6.1. INTRODUCTION

Due to their superior properties such as low density, corrosion resistance and biocompatibility, titanium and its alloys are extensively used as implant materials in modern medical procedures.¹⁴¹ However, choosing titanium and titanium alloys as implant materials can be problematic¹⁴²; for example, the loose connection between the implant and the newly grown bones can cause discomfort, dislocation, or even the need for a re-implant, creating additional pain to patients.⁶¹ The main reason for this loose connection is found to be the instantaneous formation of a fibrous capsule between the implant and human body fluid after implantation, which shields osteoblasts (bone-forming cells) from the implant.¹⁴² So newly designed materials are targeted at the elimination of the fibrous capsule.¹⁴³ With advancing and integration of nanotechnology and biology¹⁴⁴, this goal is within reach.^{145,146,147}

Recent discoveries show that the process of bone growth itself is nanotechnology.^{148,149} The “bricks of bones” – hydroxyapatite (HA)¹⁵⁰ – are 2- 5 nm wide and 50 nm long, and the “cement of bones” – Type 1 collagen – has fibrils of 300 nm in length, 0.5 nm in width. These fibrils have a periodicity of 67 nm.¹⁵¹ Furthermore, the spacing between each integrin ligand – the ‘arm’ of cells to grab the implant – is 58 nm.¹⁵¹ Based on these new findings, an implant material with surface features at these scales could have a better interaction with cells and improve the quality of implantation.

Numerous efforts have been made to enhance the surface roughness of conventional titanium/alloy implants, including simple chemical oxidation¹⁵², electrophoretic deposition¹⁵³, sputtering or hot pressing.¹⁵⁴ One standard method to evaluate the effectiveness of these surface-modified implants is to test the formation of the HA layer (“bricks of bones”), by dipping implants into a simulated body fluid.^{141,155}

It is found that the surface roughness, fabricated by methods aforementioned, stays at micrometer scale, *i.e.* samples are still featureless at the nanoscale. Recently, it has been discovered that surfaces with nanoscale features, either disordered or ordered (*e.g.* gold nanoparticle array, titanium nanotube array, and nanostructured tantalum surfaces) can greatly improve cell adhesion, proliferation, and differentiation.¹⁴⁵

Our group has devised a generalized method for nanopatterning a metal surface that is inexpensive as well as time-efficient.¹⁰² The generated patterns, which are called dimples, are tens of nanometers wide, six to ten nanometers deep.¹⁰³ Patterns of highly ordered dimple arrays are achieved by electropolishing a piece of metal (as large as several cm²) in an optimized electrolyte at an optimized potential. Windows for the optimized electrolyte and the optimized potential are narrow, and if experimental conditions are not at optimum for the dimple formation, the surface will exhibit random nano roughness. So far, this method has successfully generated dimples on pure metals (tantalum, titanium, tungsten, vanadium, and zirconium).⁶² Here, we demonstrate that the same pattern can be achieved on a titanium alloy (Ti-6Al-4V). We expect that this dimpled titanium alloy will be a perfect substrate for implantation, because the average periodicity of the dimple pattern is about 50nm, which is on the same scale as the spacing

of integrin ligands out of the cell. The morphology and order of dimples are influenced by the local chemical composition of the surface, which is confirmed by Photoemission Electron Microscopy (PEEM). Overall, dimpling conditions for the alloy are similar to those for titanium, which is the main element in the alloy. The dimpling conditions for vanadium, an important minor constituent, are found to be significantly different.

6.2. EXPERIMENTAL

The biochemical alloy (Ti-6Al-4V) from RMI Titanium Company contains 89.56% of titanium, 6.16% of aluminum, 3.92% of vanadium, 0.213% of iron, 0.12% of oxygen, 0.02% of carbon, 0.008% of nitrogen. Prior to dimpling, the titanium alloy samples (20mm × 10mm) are first mechanically ground using silicon carbide paper, then chemical-mechanically polished with a mixture of colloidal silica particles (OP-S) and hydrogen peroxide in a 7:3 ratio. Samples have a mirror finish when viewed with the eye. All samples are then ultrasonicated in acetone, methanol (both semiconductor grade, Fisher Scientific) and Millipore water (18.2 MΩ•cm). Dimpling is carried out in a stirred solution of concentrated H₂SO₄ (95–98%, reagent grade, Fisher Scientific) and concentrated HF (48%, Fisher Scientific). Half of the alloy sample is immersed in the electrolyte. Dimpling is conducted using a conventional two-electrode system connected to a DC power supply (Agilent E3615A, capable of providing up to 1 A at up to 60 V). A Pt/Ir wire is used as the counter electrode (cathode). The working electrode (anode) is a partially immersed alloy sample connected with an alligator clip well above the polishing solution and through a copper wire to the power supply. The distance between the working electrode and the counter electrode is kept at 1.5 cm. During dimpling, the

solution is stirred using a coated magnetic bar. All experiments are performed at approximately room temperature. No attempt is made to thermostat the electrolyte. Immediately after dimpling, the sample is rinsed with deionized water, dried with nitrogen and stored under nitrogen before further characterization with SEM and PEEM.

The PEEM experiments are carried out using an Elmitec PEEM III (Canadian Photoemission Electron Research Spectromicroscope, CaPeRS) attached to the spectromicroscopy (SM) beamline at the Canadian Light Source (CLS) in Saskatoon, Saskatchewan (10ID-1). Photons from the SM beamline, with energies between 130 eV and 2500 eV, are directed onto the sample, which have been brought into focus using a mercury lamp. The projected secondary electrons are analyzed by a hemispherical band-pass electron energy analyzer and recorded by a CCD camera. Stacks of images with an energy resolution of 0.3 eV are obtained for Ti, V, O and V, which are later processed in aXis2000.

6.3. RESULTS AND DISCUSSION

6.3.1. OPTIMUM CONDITIONS TO DIMPLE Ti-6Al-4V

The optimized conditions for dimples on titanium include 8:2 (volumetric ratio) H₂SO₄/ HF electrolyte solution, cell potential of 15 V and electropolishing time of 2 minutes. The optimal conditions for generating dimples on titanium alloy (Ti-6Al-4V) should be close to that for pure titanium, because the alloy contains close to 90% of titanium. In the end, all the parameters, electrolyte composition, electropolishing potential and electropolishing time, are fine-tuned to find the best conditions for producing dimples on Ti-6Al-4V.

6.3.1.1. ELECTROLYTE COMPOSITION

As shown in previous chapters, the composition of the electrolyte plays a crucial role in determining the surface morphology on the electrode after electropolishing.

Disordered dimples are observed on the samples, which have been electropolished in the 10:90 HF: H₂SO₄ (volume ratio) electrolyte (Figure 6.1a). Non-uniform dimple arrays start to form on the alloy surface, after the sample is electropolished in the 15:85 (volume ratio) electrolyte (Figure 6.1b). As the weight of HF in the electrolyte increases, a uniform array of dimples forms in the 20:80 (volume ratio) electrolyte (Figure 6.1c). If the amount of HF is further increased to a 25:75 ratio, most of the ordered dimple array is replaced by random nanoscale roughness (Figure 6.1d).

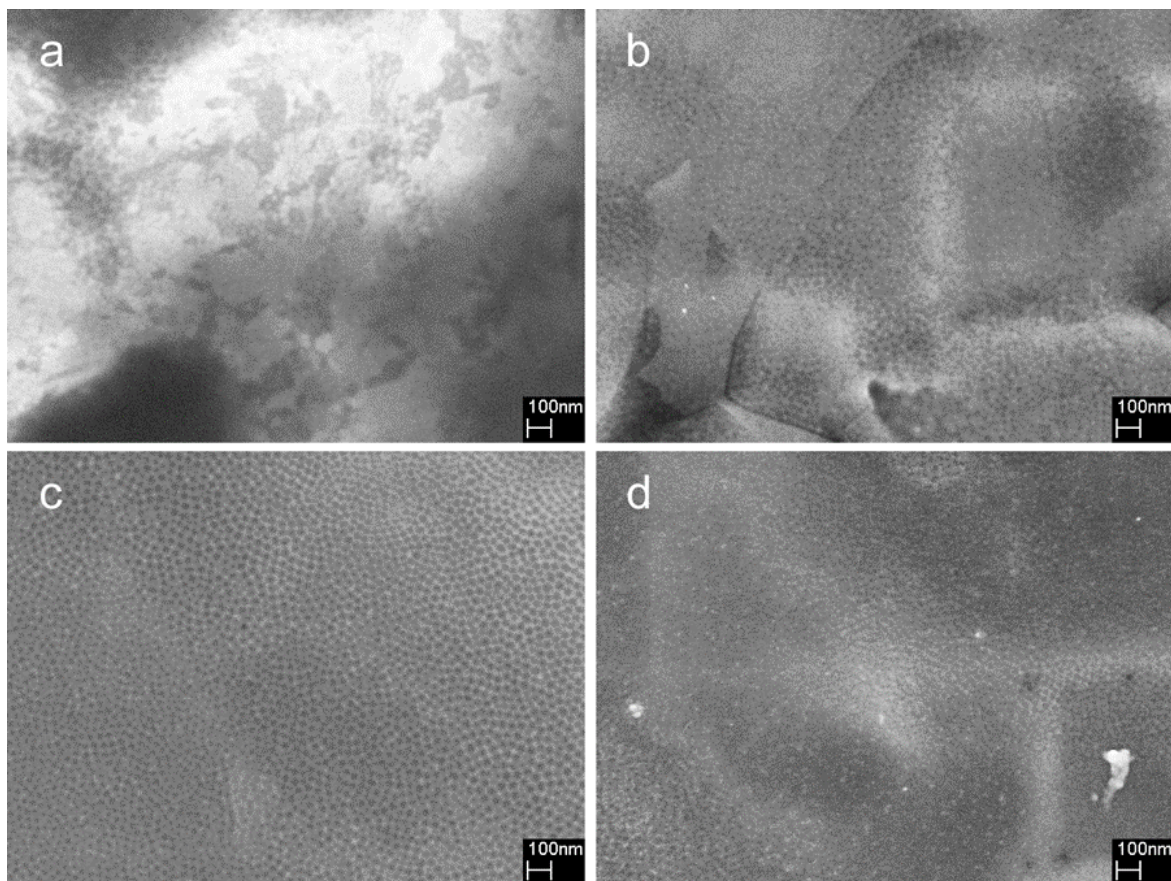


Figure 6.1. SEM images of electropolished titanium alloy surfaces showing the deterioration of the long range order of dimples as one moves away from the narrow electrochemical regime of ordered pattern (dimples) formation by changing the concentration: (a) 9:1 $\text{H}_2\text{SO}_4/\text{HF}$; (b) 8.5:1.5 $\text{H}_2\text{SO}_4/\text{HF}$; (c) 8:2 $\text{H}_2\text{SO}_4/\text{HF}$; (d) 7.5:2.5 $\text{H}_2\text{SO}_4/\text{HF}$. The potential is kept at 15 V through all the samples and the electropolishing time is 300 seconds.

The difference in metal dissolution speed in the different electrolytes plays a predominant role in pattern formation. When a certain balance of oxide formation speed and dissolution speed is reached, ordered patterns can form during electropolishing. With the addition of 48% HF (a source of water as well), the current density also increases, which indicates faster oxidization and dissolution of metals (more HF to attack the oxide formed).

6.3.1.2. POTENTIAL

The potential's impact on the dimple formation is less pronounced than the electrolyte. The suitable cell potentials for dimple formation range from 15 V to 20 V, though slight morphology differences are evident at different potentials. On the 13 V sample, there is surface roughness on the same scale as dimples, but less ordered (Figure 6.2a). Well-ordered dimple arrays are observed at 15 V (Figure 6.2b). At higher potentials, the oxide formation and dissolution reactions become more vigorous, and the dimple pattern becomes less ordered. At 17 V, dimple sizes vary considerably and their arrangement becomes disordered (Figure 6.2c). At cell potential of 20 V, some areas are missing dimples (Figure 6.2d).

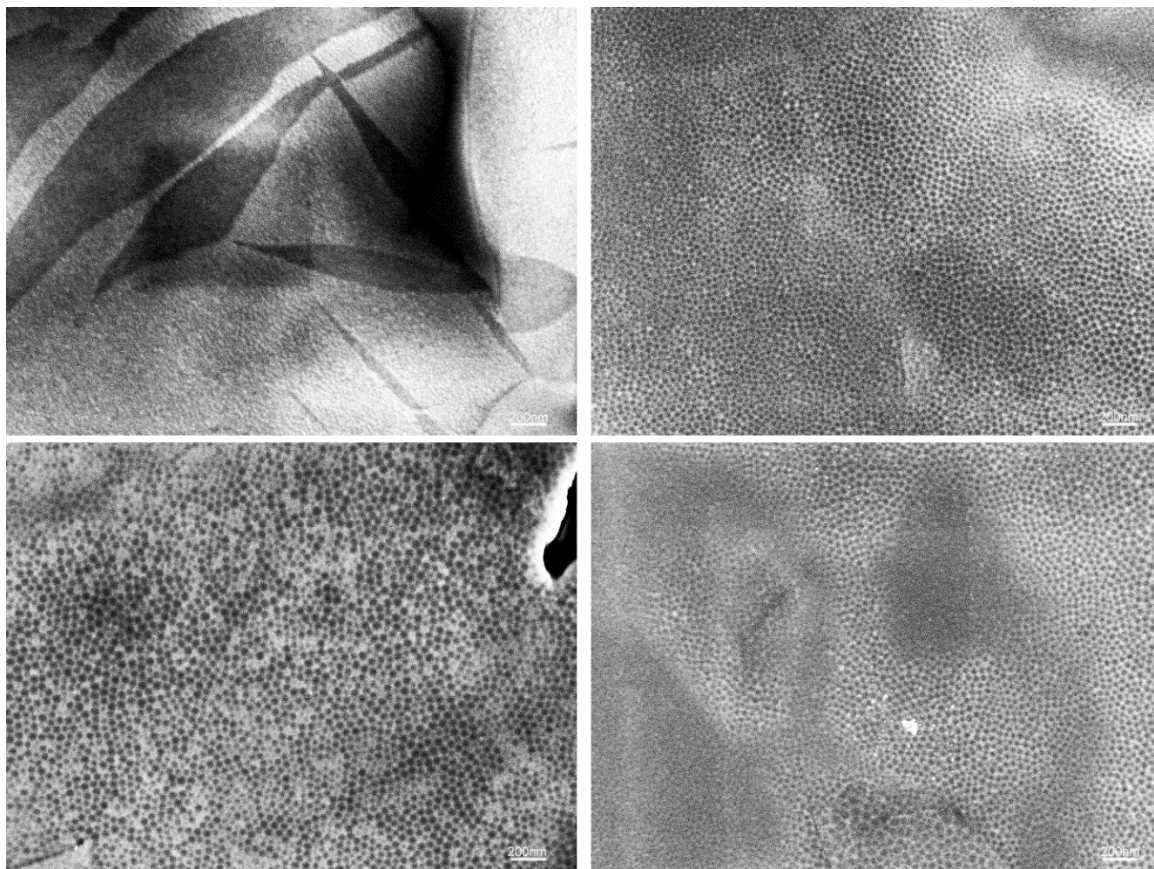


Figure 6.2. SEM images of electropolished titanium alloy surface showing the deterioration of the long range order of dimples as one moves away from the narrow electrochemical regime of ordered pattern (dimples) formation by changing the concentration: (a) 13V; (b) 15V; (c) 17V; (d) 20V. The electrolyte solutions for all samples are 8:2 (volume ratio) $\text{H}_2\text{SO}_4/\text{HF}$, and the electropolishing time is 300 seconds.

6.3.1.3. ELECTROPOLISHING TIME

Once an ordered dimple pattern has formed, longer electropolishing time generally does not change the morphology of dimples on pure metals, because the formation of dimples is based on an isotropic etching. Longer electropolishing time may just lead to a flattened surface at the micrometer scale.

However, electropolishing time is an important parameter in the fabrication of dimples on alloys, because of the preferential etching of different metals on the surface. As a result, long electropolishing times lead to rough surfaces at the micrometer scale (Figure 6.3a, c). Given the fact that the ordering process of dimples is completed within 60 seconds after electropolishing, alloy samples, electropolished for 30 seconds and 2 minutes, are compared. The sample electropolished for 30 seconds is flat at the micrometer scale, but 30 seconds is too short for dimples to arrange themselves in order (Figure 6.3a, b). There is a uniform dimple array on the 2-minute sample, and several plateaus at the microscale are observed (Figure 6.3c, d). The dimple pattern at the nanoscale may be beneficial for cell adhesion and surface roughness at the microscale caused by different electropolishing times gives us further control over the surface morphology to tune cell adhesion. In experiments described hereafter, all samples are electropolished for 90 seconds to ensure the formation of dimples and a relatively flat surface at the microscale.

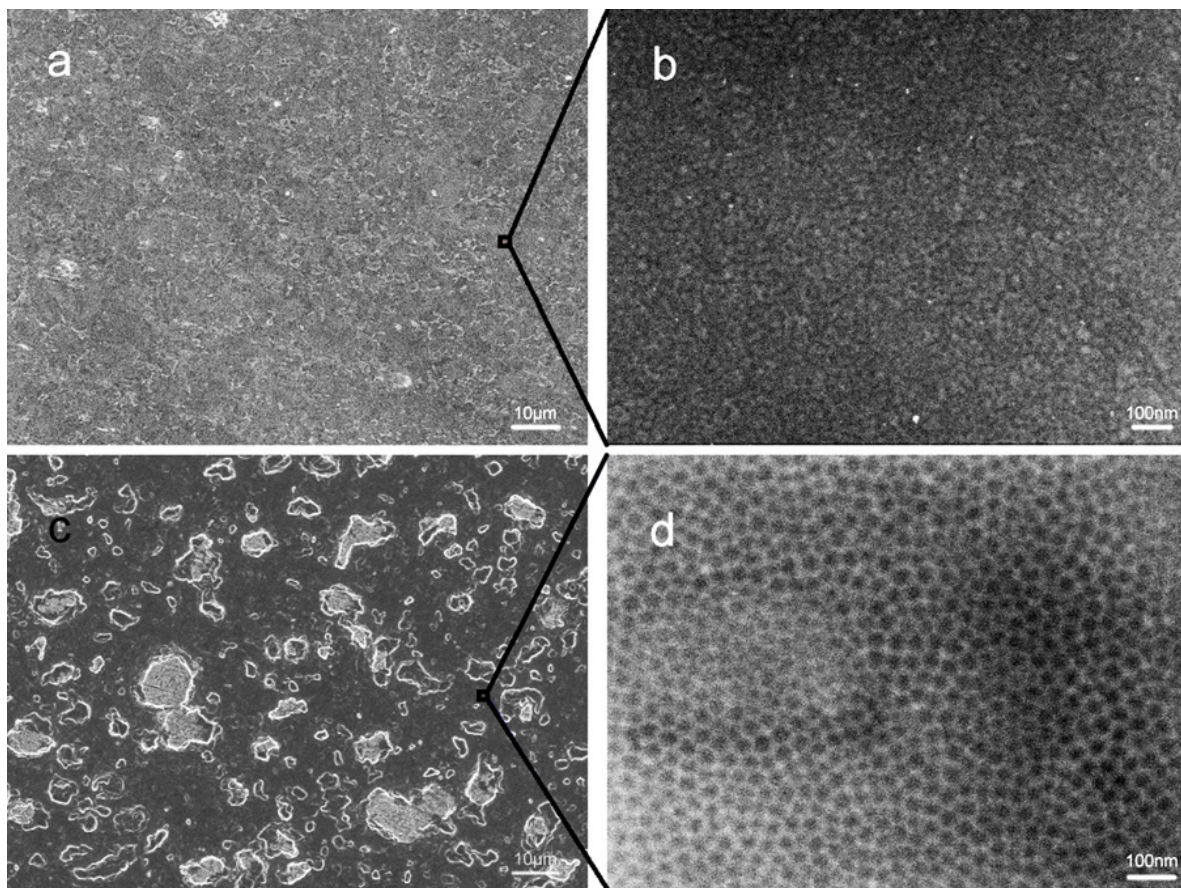


Figure 6.3. Large scale (a) and high resolution (b) SEM images of titanium alloy samples electropolished for 30 seconds; large scale (c) and high resolution (d) SEM images of titanium alloy samples electropolished for 120 seconds. The electrolyte for this time series experiment is 8:2 (volume ratio) H_2SO_4 / HF and the cell potential is kept at 15 V.

6.3.2. EFFECT OF SURFACE COMPOSITION

Even though conditions are optimized, dimples are still not uniform across the whole sample surface (Figure 6.4). There must be some parameters affecting the uniformity of dimples other than the electrolyte concentration, cell potential, and dimpling time.

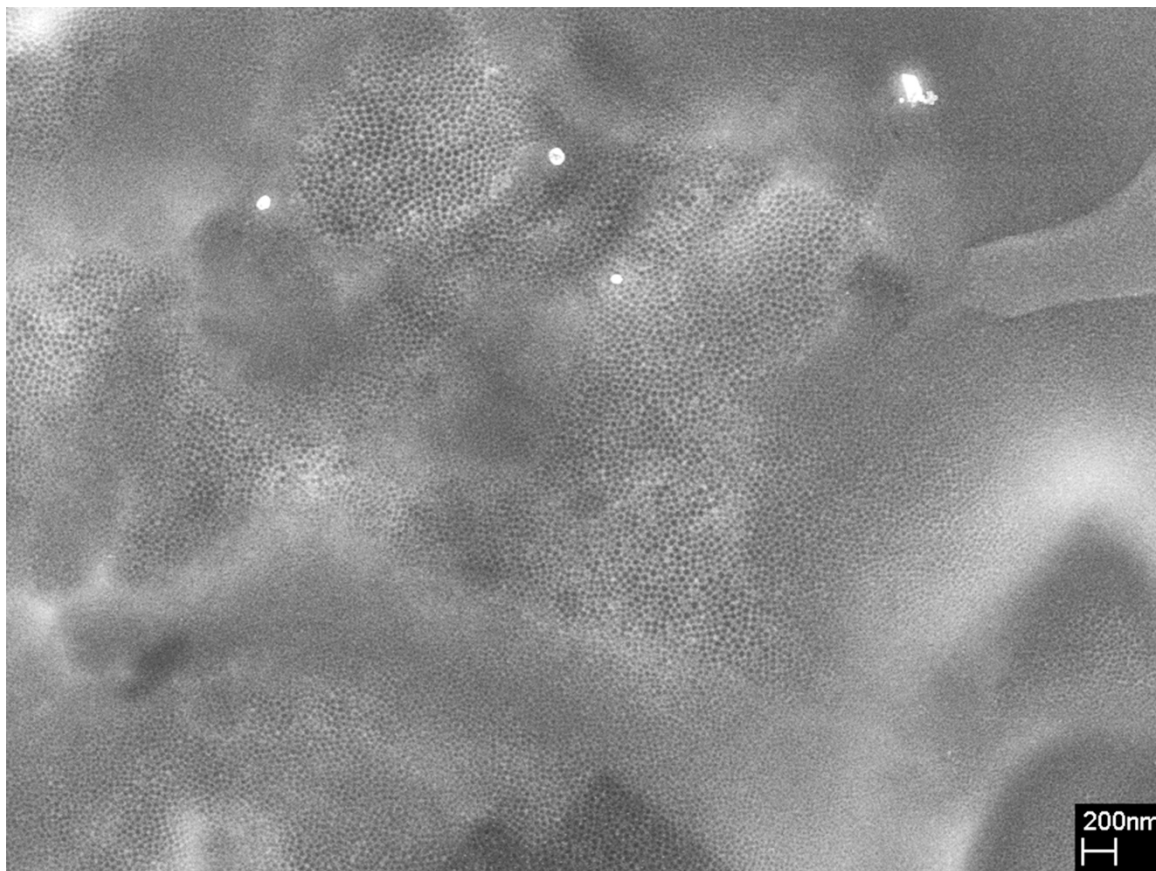


Figure 6.4. Large scale SEM image of titanium sample dimpled under optimized conditions, showing that dimples are not uniform in size across the whole surface.

6.3.2.1. EDX

As indicated in previous chapters (Chapter 4 and Chapter 5), the optimal conditions for making dimples on various metals differ. This assertion explains why there are small areas on the alloy, where dimples are missing. Because these areas contain impurities, which could not be dimpled by the conditions optimized for titanium.

However, EDX cannot confirm this, due to the overlap between the vanadium $K\alpha_1$ (4.952 KeV), $K\alpha_2$ (4.944 KeV) peaks and the titanium $K\beta_1$ peak (4.931 KeV) (Figure 6.5).

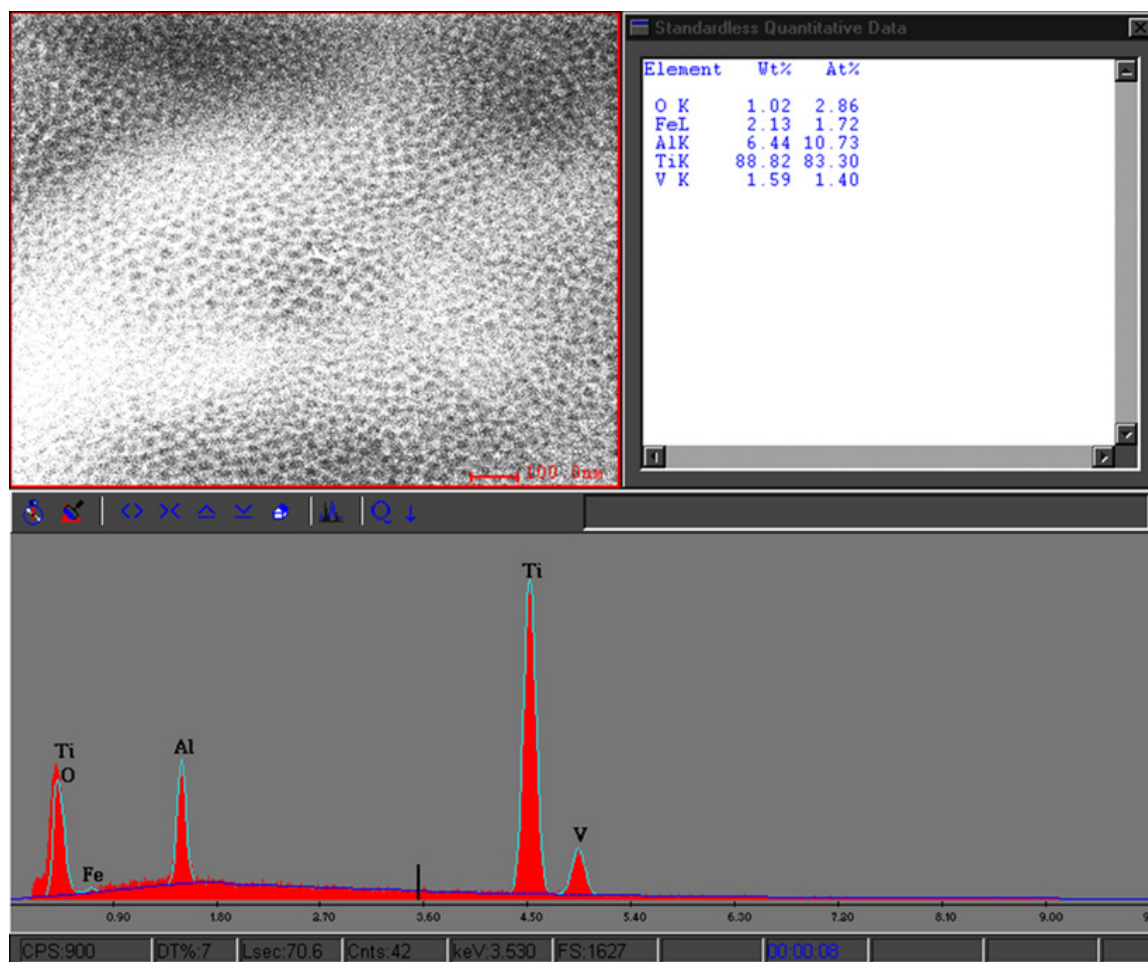


Figure 6.5. EDX of dimpled titanium alloy sample. Titanium K β 1 peak (4.931 KeV) overlaps with vanadium K α 1 (4.952 KeV), K α 2 (4.944 KeV) peaks.

6.3.2.2. PEEM

The overlap issue can be solved using PEEM. In the PEEM experiment, the sample is illuminated using UV (mercury lamp) or X-ray (synchrotron) radiation. The photo-emitted electrons are then extracted at high potential and pass through a system of electrostatic and magnetic lenses while maintaining spatial resolutions of better than 100 nm. Even though it is possible to energy-analyze the photoelectrons and collect a spatially resolved XPS signal, disadvantages of this approach are twofold. Firstly, only very low

kinetic energy electrons can be analyzed in the PEEM microscope, which will render the technique excessively surface sensitive. Secondly, there will be very little signal collected since most of the photoelectrons are discarded in the analyzer. We would give up several orders of magnitude in sensitivity. Therefore, the PEEM is operated in total electron yield mode for the observation of X-ray absorption spectra (XAS), from which the incident photon energy is scanned on the synchrotron beamline. In this mode, photoelectrons are collected from the top few nanometers below the surface.

The energy scanning range for certain elements are determined after consulting the X-ray data booklet.¹⁵⁶ For example, pure titanium has two peaks, one at 460.2 eV, which is L2 2p_{1/2} and the other one at 453.8 eV, which is L3 2p_{3/2}, so the scanning energy range for titanium is from 445 eV to 475 eV. The electron binding energy of titanium captured by CaPeRS is 459.8 eV (L3 2p_{3/2}) and 465.2 eV (L2 2p_{1/2}) (Figure 6.6a). Similarly, the electron binding energies for pure vanadium are measured at 517.0 eV (L3 2p_{3/2}) and 524.0 eV (L2 2p_{1/2}) (Figure 6.6b). For aluminum, K 1s peak is measured at 1567.0 eV instead of L peaks (Figure 6.6c). All the electron binding energy peaks captured by CaPeRS shift approximately 5 eV from those recorded in X-ray data booklet.

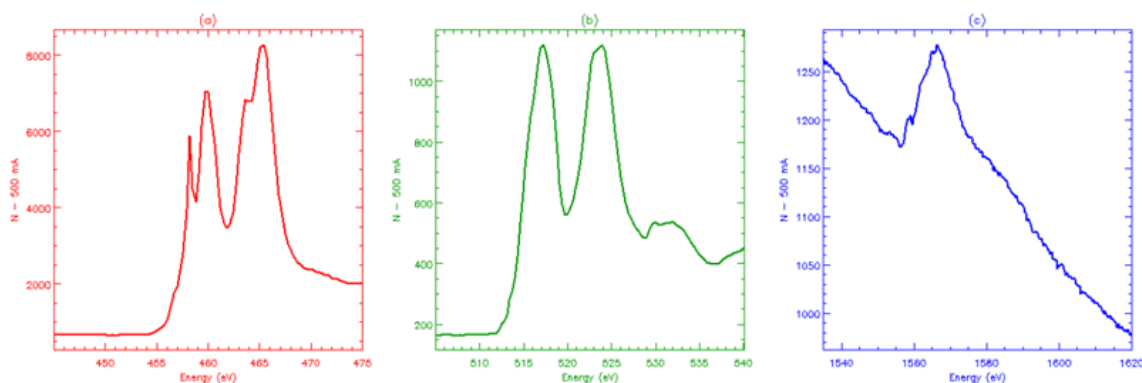


Figure 6.6. X-ray Absorption Spectra (XAS) of titanium (a), vanadium (b), aluminum (c) obtained by PEEM.

In the PEEM experiment, two samples, dimpled and un-dimpled (pre-treated in the same way as the dimpled sample except that it is not electropolished) are compared.

For the un-dimpled sample (control sample), high-resolution images (high dwell time to eliminate noises) are collected at the energy of electron binding energy peaks of each element (Figure 6.7, left column), and baselines (Figure 6.7, central column). The ratio of images in the left column to those in the central column is the distribution of each element on the surface (Figure 6.7, right column). For visibility, the surface element map is coded with colour. (Figure 6.8). An Hg lamp image (Figure 6.8a) shows that there is microscale surface roughness on the sample after mechanical grinding and chemical-mechanical polishing. The surface element map of the un-dimpled sample indicates an uneven distribution of elements on the control alloy sample surface (Figure 6.8b, c, d).

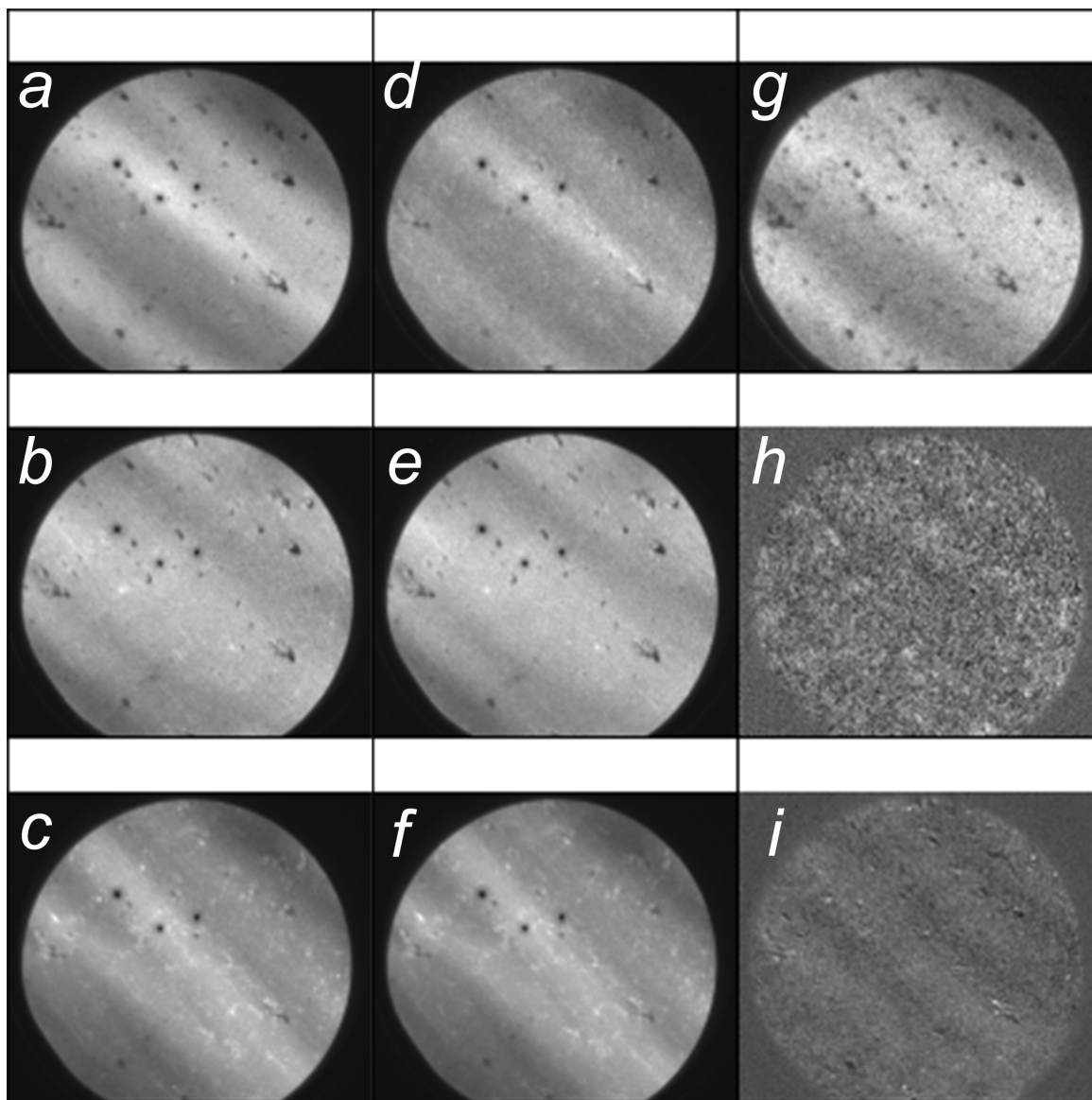


Figure 6.7. High-resolution synchrotron images of control sample. Image *a,b,c* are synchrotron images captured at baseline, images from *d* to *f* are synchrotron images taken at titanium peak (465 eV), vanadium peak (516 eV), Aluminum peak (1566 eV) correspondingly. Image *g* (the ratio of image *d* to image *a*) is the titanium map of the control sample; image *h* (the ratio of image *e* to image *b*) is the vanadium map; image *i* (the ratio of image *f* to image *c*) is the Aluminum map. All images are rescaled for viewing.

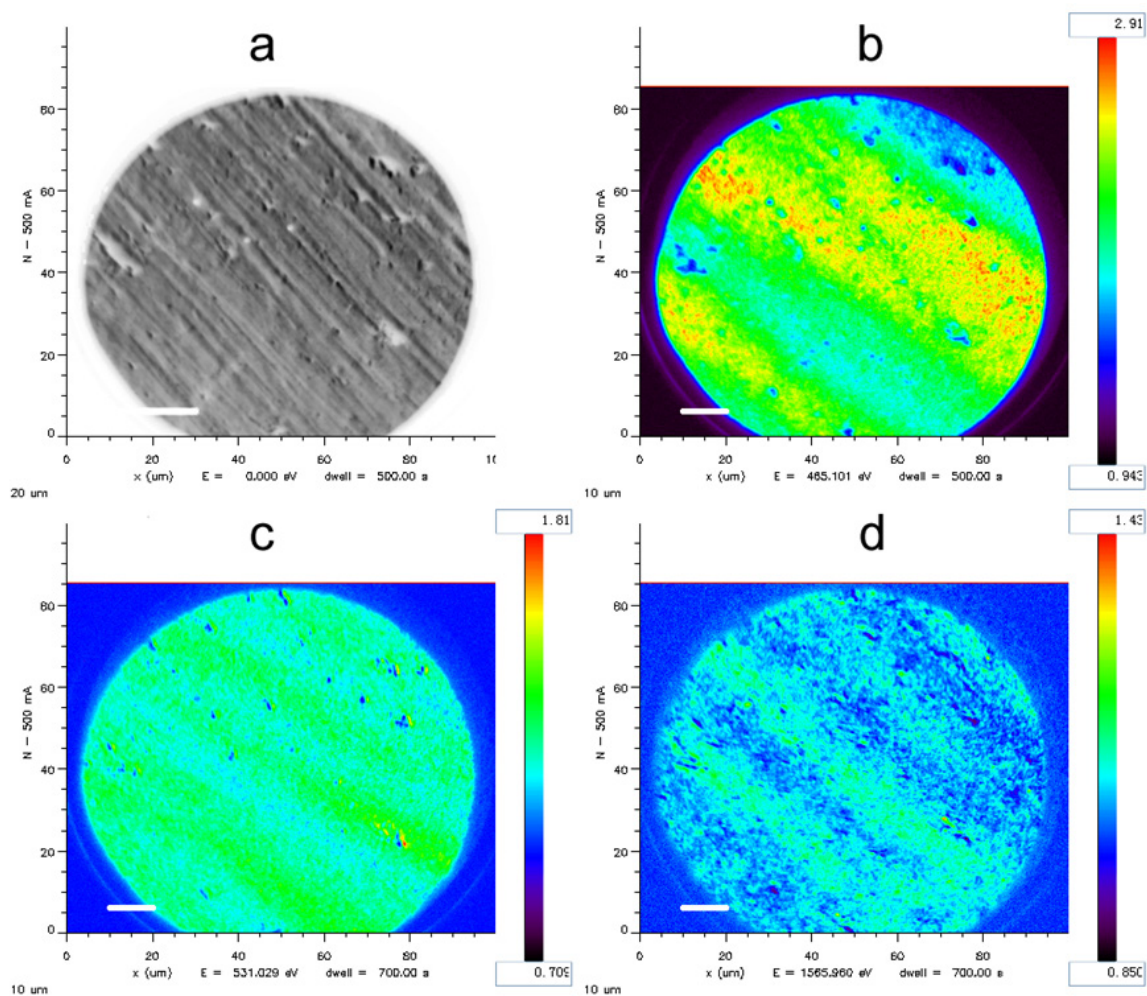


Figure 6.8. The Hg lamp image (a) of the un-dimpled sample (control) and its surface element maps of titanium (b), vanadium (c) and aluminum (d). NB: differences between each colour bar.

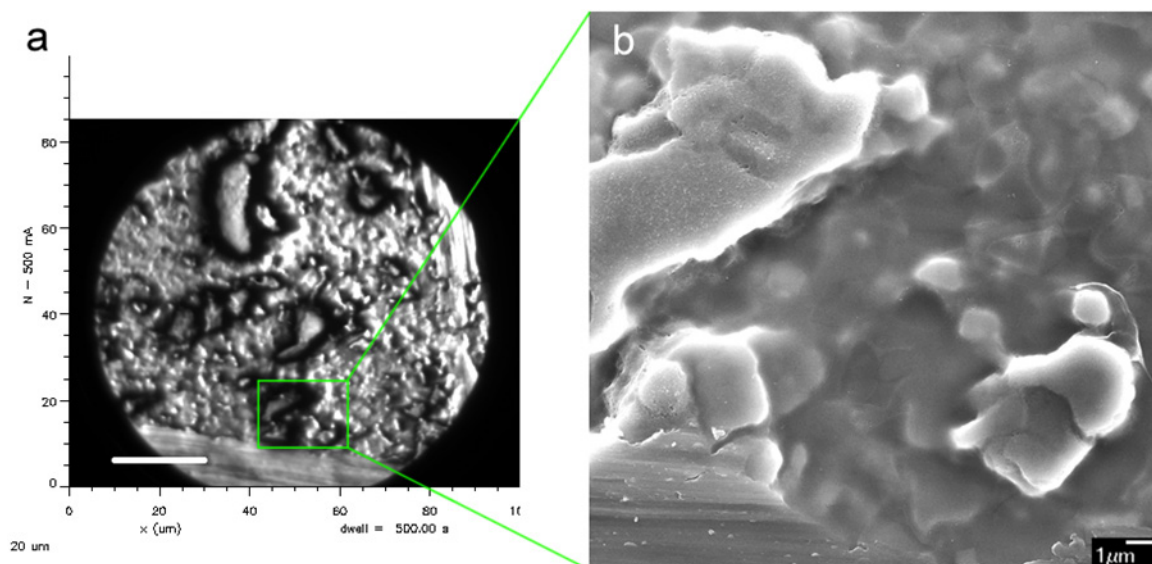


Figure 6.9. The correlation of the PEEM Hg lamp image of the dimpled titanium alloy sample with its SEM image.

The Hg lamp image of the dimpled sample was correlated to its SEM image, with the help of a pre-marked ‘V’ scratch on the sample surface (Figure 6.9). Figure 6.10 is a combination of high-resolution synchrotron images of sample at ‘V’ mark. The surface elemental maps (Figure 6.11b, c, d) of the dimpled sample are taken in the same manner as those of the un-dimpled sample, except that the dwell time spent on the dimpled sample to capture one image is even longer than the control sample. However, the elemental distribution on the “V” shaped scratch should not be taken into account. Because of the deep scratch, it is not showing the chemical composition on the surface. The titanium surface map (Figure 6.11b) shows that the concentration of titanium increases after dimpling. This effect may be caused by the removal of the titanium native oxide after electropolishing (sample is kept under nitrogen before the PEEM experiment), which ends up causing a net increase of the titanium signal. However, the concentration

of vanadium (Figure 6.11c) and aluminum stays approximately the same before and after dimpling (Figure 6.11d).

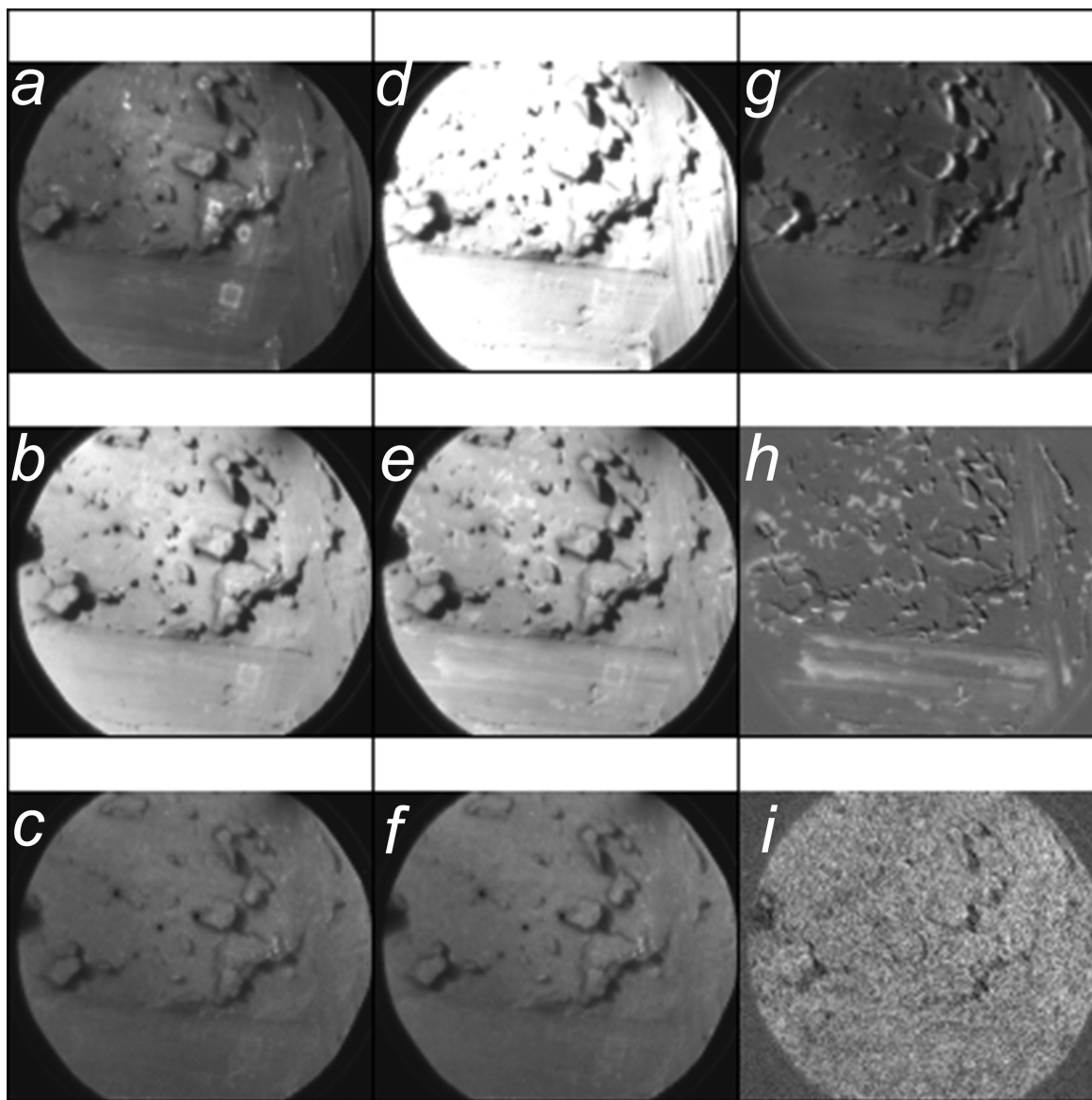


Figure 6.10. High-resolution synchrotron images of dimpled sample. Images (a) to (c) are synchrotron images captured at baseline, images from d to f are synchrotron images taken at titanium peak (465 eV), vanadium peak (516 eV), Aluminum peak (1566 eV) correspondingly. Image (g), the ratio of image (d) to (a) is the titanium map of the control sample; image (h), the ratio of image (e) to (b) is the vanadium map; image (i), the ratio of image (f) to (c) is the Aluminum map. All images are rescaled for viewing.

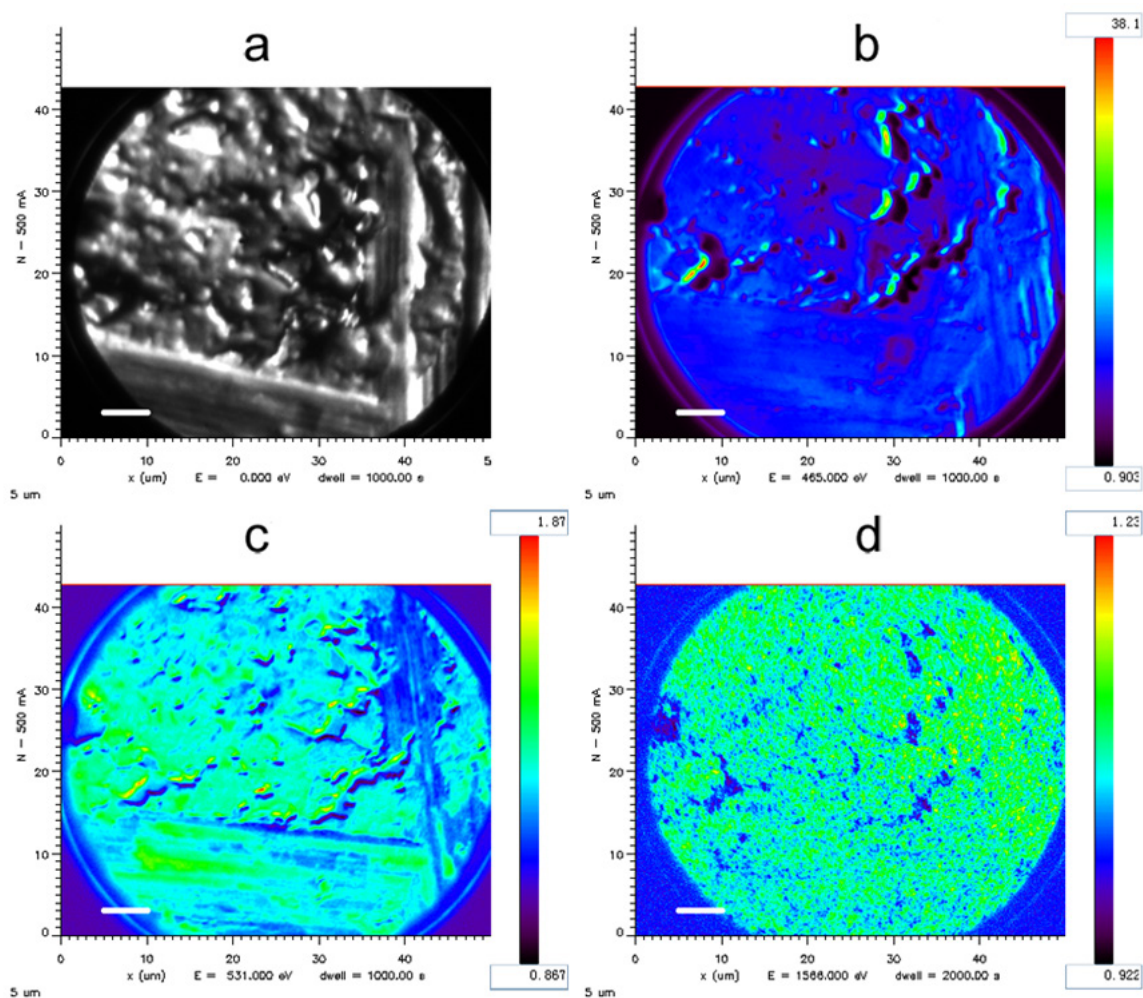


Figure 6.11. The Hg lamp image (a) of the dimpled sample and its surface element maps of titanium (b), vanadium (c) and aluminum (d) at the ‘V’ shape scratch. NB: differences between each colour bar.

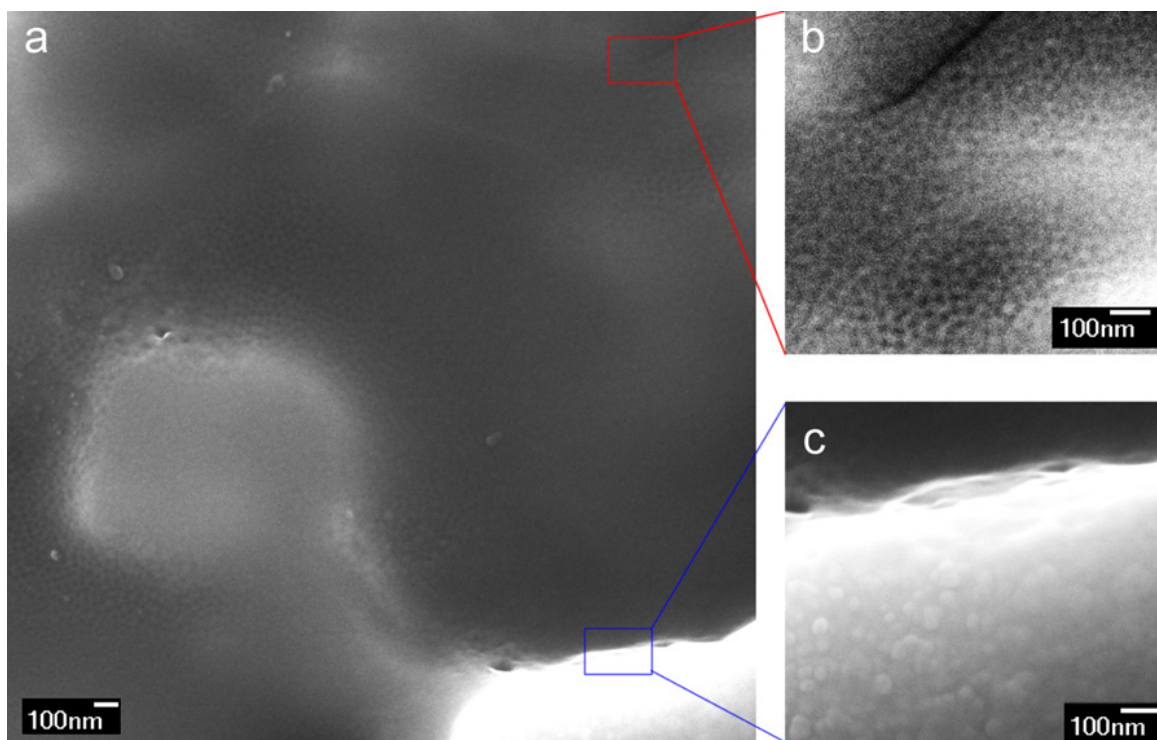


Figure 6.12. (a) High-resolution SEM image of Figure 6.11; there are dimples off the plateau (b); (c) there are no dimples on the plateau, where the concentration of vanadium is relatively higher.

One plateau (in Figure 6.9b) is related to a vanadium-rich area in the surface element map (Figure 6.12c). A zoom-in SEM image of the plateau (Figure 6.12a) shows that there are no dimples on the plateau (Figure 6.12c), where vanadium is rich; off the plateau, where the concentration of vanadium is relatively lower, there are dimples (Figure 6.12b).

Further experiments show that electropolishing vanadium in an 8:2 (volume ratio) $\text{H}_2\text{SO}_4/\text{HF}$ electrolyte solution leads to irregular surface roughness at the microscale level (Figure 6.13). Based on these findings, it is possible to conclude that, due to a slower dissolving speed of vanadium in the 8:2 $\text{H}_2\text{SO}_4/\text{HF}$ electrolyte than titanium, the vanadium-rich area gets etched less, therefore vanadium-rich plateaus start to form on the

surface as dimpling time increases (surface becomes rougher at microscale); since the 8:2 H₂SO₄/ HF electrolyte is not the optimal dimpling electrolyte for vanadium, no dimples are observed on plateaus. The conditions for making dimples on vanadium are summarized in Chapter 4.

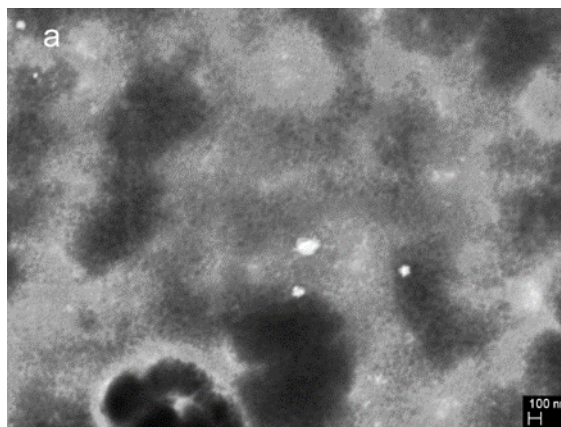


Figure 6.13. SEM image of vanadium electropolished in 8:2 H₂SO₄/ HF (volume ratio) electrolyte at 15 V for 2 min, showing that the surface is rough at microscale.

6.4. CONCLUSION

An ordered nanoscale pattern has been fabricated on a biomedical titanium alloy surface (Ti-6Al-4V) *via* dimpling. Electrolyte composition, cell potential and electropolishing time are found to be important parameters for the ordering of dimples, and a set of optimal parameters have been found. This work is the first demonstration that ordered dimple array can be fabricated on alloy surfaces in addition to pure metal surfaces. The size and spacing of dimples are on the same scale as features embedded on the cell membrane, which allows the implant surface to be tailored for stronger cell adhesion and improved integration between bone and implant. We also find that the uniformity of the nanoscale dimples is subject to the surface chemistry. Due to a slower

dissolution rate in the specific electrolyte, vanadium is enriched at the surface, and there are no dimples in these areas. This observation gives us further control to tune the spacing of the dimple array, for the best matrix for cell adhesion. Besides that, longer dimpling time leads to the formation of the vanadium rich plateau, which adds tunable microscale roughness to the implant surface for desired cell adhesion.

CHAPTER-7

NANO-PATTERNING SILICON VIA ELECTROPOLISHING

7.1. INTRODUCTION

Single-crystalline silicon and doped silicon have been widely used in integrated circuits¹⁵⁷ and in photovoltaic applications.¹⁵⁸ Nanopatterning silicon is of great interest and different kinds of techniques have been developed to make patterns on silicon, *e.g.*, laser induced field oxidation¹⁵⁹, soft-lithography¹⁶⁰, pattern transfer from PAA template¹⁶¹, near-field enhanced laser irradiation¹⁶², and Dip-pen nanolithography.¹⁶³

Electrochemical methods offer a less expensive and time-efficient alternative to nanopattern silicon.¹⁶⁴ Under specific circumstances, porous silicon, fabricated by anodization, can emit visible light.⁶⁰ L. Canham¹⁶⁵ explains that the emitted light is due to the quantum confinement effect of nanopores on the porous silicon. However, pores on silicon are not well-ordered.

As demonstrated in previous chapters, electropolishing can generate various kinds of nanopatterns on metal surfaces. These patterns possess greater order than the porous silicon. It would be of great interest to extend the dissipative nanopatterning technique from metals to semi-conductors.

7.2. EXPERIMENTAL

The silicon wafers (p<100>, 375 micrometer thick, 100mm diameter, Resistivity: 0-100Ω·cm from Silicon Inc. Boise, Idaho USA) are cut into 20mm x 5mm in size. All

samples are sonicated in acetone, methanol and Millipore water, respectively, prior to electropolishing. Electropolishing is carried out in a stirred solution of concentrated H_2SO_4 (95–98%, reagent grade, Fisher Scientific) and concentrated HF (48%, Fisher Scientific) or a mixture of ethylene glycol (98%, Fisher Scientific) and HF (48%, Fisher Scientific). Half of the silicon sample is immersed in the electrolyte. Electropolishing is conducted using a conventional two-electrode system connected to a DC power supply (Agilent E3615A, capable of providing up to 1 A at up to 60 V). A Pt/Ir wire is used as the counter electrode (cathode). The distance between the working electrode and the counter electrode is kept at 1.5 cm. During electropolishing, the solution is stirred using a PTFE-coated magnetic bar. All the experiments are performed at approximately room temperature. No attempt is made to thermostat the electrolyte, which slightly warmed during the experiment. Immediately after dimpling, the sample is rinsed with deionized water, dried with nitrogen, and stored under nitrogen before further characterization with microscopes.

7.3. RESULTS

7.3.1. POROUS SILICON AND YELLOW SILICON OXIDE

Silicon and its oxide can only be etched by HF or hot alkali (*e.g.* KOH at 70°C¹⁶⁶). The difference between them is that HF etches silicon isotropically, while OH^- etches certain crystal orientation preferentially. Since the electropolishing pattern formation is an isotropic process, HF is superior to KOH.

The electrolyte for dimpling tantalum (98% sulphuric acid and 49% HF, in 9:1 volume ratio) is first chosen to electropolish silicon. At low potential ($< 15\text{V}$, the corresponding current density is less than 300 mA/cm^2), the surface is porous at the nano scale; at high potential ($> 15\text{V}$), a layer of white oxide is left on the surface, which indicates that the sample has been anodized, instead of electropolished.

In the 8:2 volume ratio electrolyte, which makes dimples on Titanium, the same nanopores as aforementioned are observed at 15 V (Figure 7.1). At higher potential (20V), yellow oxide begins to detach off the surface during experiment (Figure 7.2).

Similar observations are made from experiments with electrolyte from: 7:3 to 6:4 and to 5:5 (98% sulphuric acid to 48% HF, volume ratio).

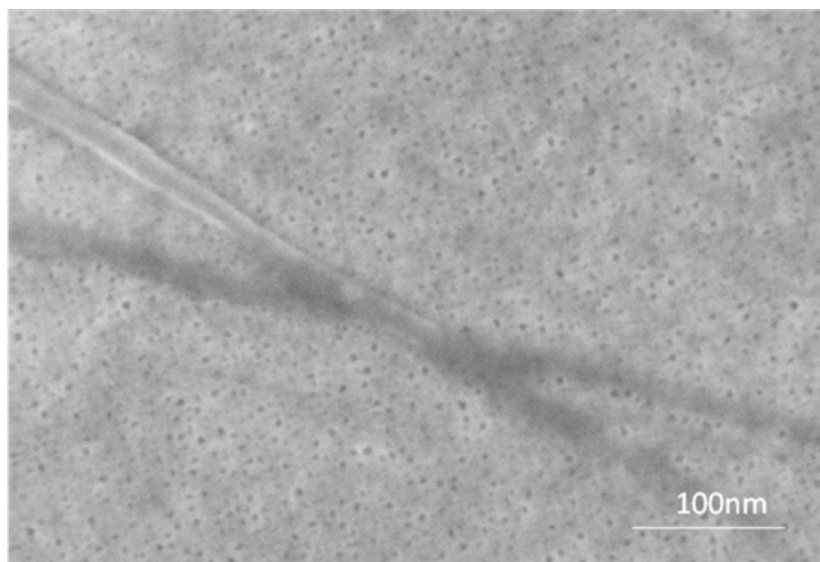


Figure 7.1. SEM image of the porous silicon, electropolished in 8:2 (98% sulphuric acid to 48% HF, volume ratio) at 15V .



Figure 7.2. Anodized in the 8:2 (volume ratio of concentrated sulfuric acid to concentrated HF) at 20V, a layer of yellow oxide is formed on the surface and began to detach off the surface.

A detailed study is carried out on the origin of this yellow oxide film. A low-resolution optical image (Figure 7.3) captured by a camera inside an AFM shows that there may exist a multi-layer structure on the anodized silicon surface.

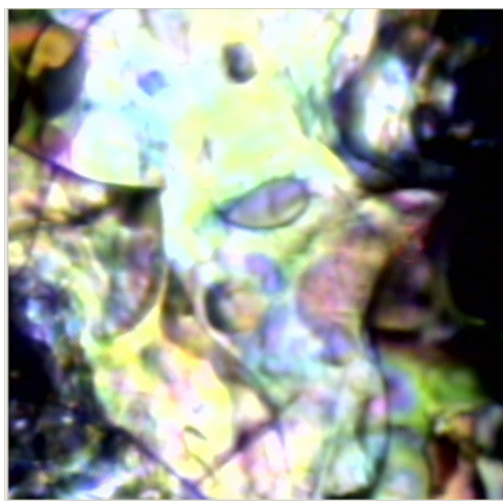


Figure 7.3. An optical image captured by an AFM camera shows the coloured layer-type structures on the surface.

A better-quality image (Figure 7.4) shows that the surface is not uniform at large scale, but covered with holes as large as one millimeter. There are regions showing

different colours, which are dominated by yellow-brown. This is the source of the yellow colour during electropolishing.

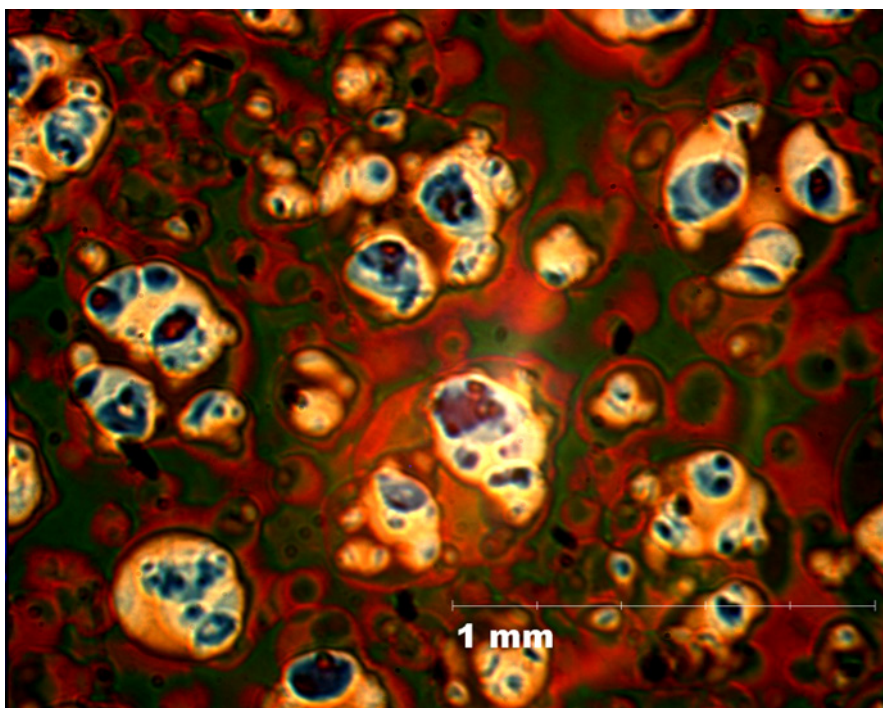


Figure 7.4. Optical microscope picture of sample shown in Figure 7.1.

A cross-sectional SEM image (Figure 7.5) captures the yellow oxide layer detached off the surface. However, due to the charging of the non-conducting oxide layer, higher resolution SEM image could not be obtained. The yellow colour, in the end, could originate from these detaching layers or embedded silicon nano crystals.¹⁶⁷

The oxide, left on samples, indicates that this process is anodization, not electropolishing.

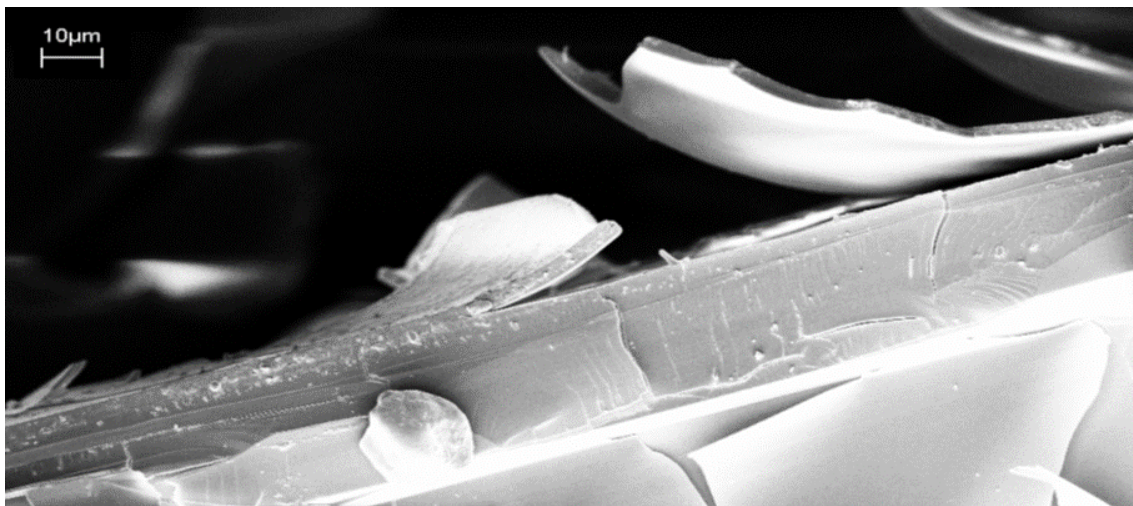


Figure 7.5. SEM image of the sample with covered by the yellow oxide. The yellow colour originates from structures on the peeling surface.

7.3.2. ‘FENCE’ AND DISORDERED NANOPATTERN IN DILUTE HF

Samples, electropolished in 1% HF solution at low potentials (< 15 V), are featureless at the nanoscale. If it is electropolished at high potentials (>15 V, *e.g.* 30V in Figure 7.6), the originally mirror-like surface changes into a milky one. SEM images of the sample surface show that the milky appearance is caused by the white ‘fence’ structure on the sample surface. Cross-section SEM (Figure 7.7) shows that the height of the ‘fence’ is about 100 nm and EDX (Figure 7.8) shows that the white ‘fence’ structure contains 3.38% oxygen (atomic %) and 94.5% silicon (atomic %), which indicates it is not based on oxide.

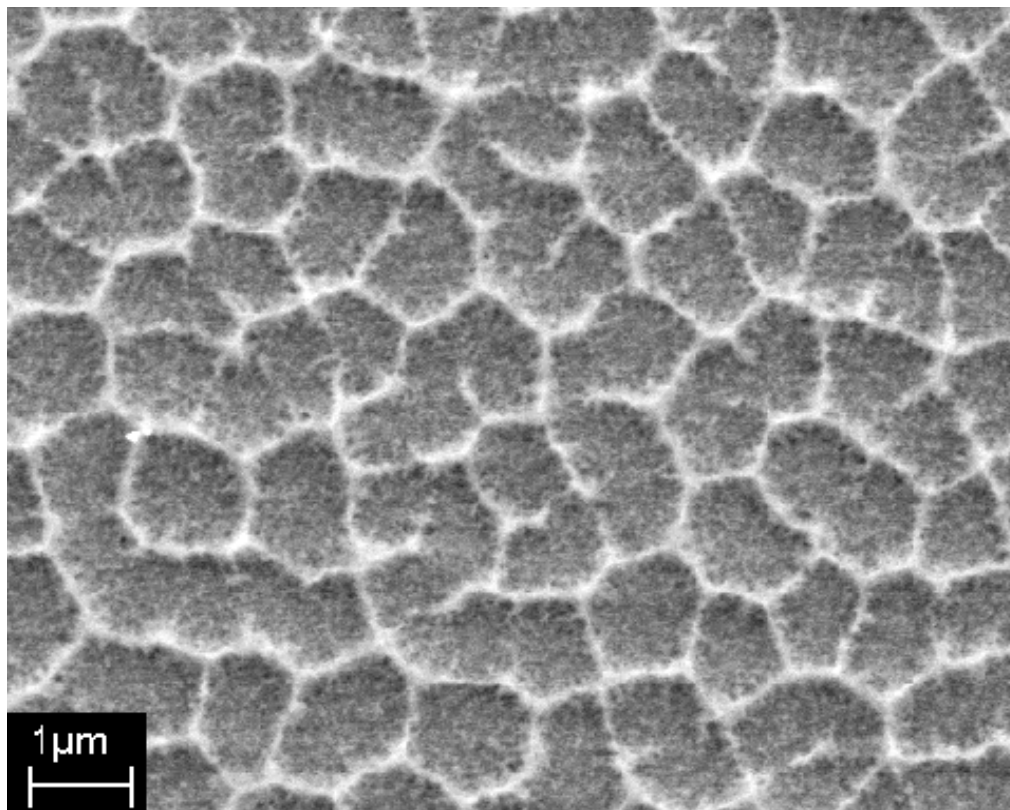


Figure 7.6. SEM image of the ‘fence’ structure formed on silicon sample, which have been electropolished in 1% HF at 30V.

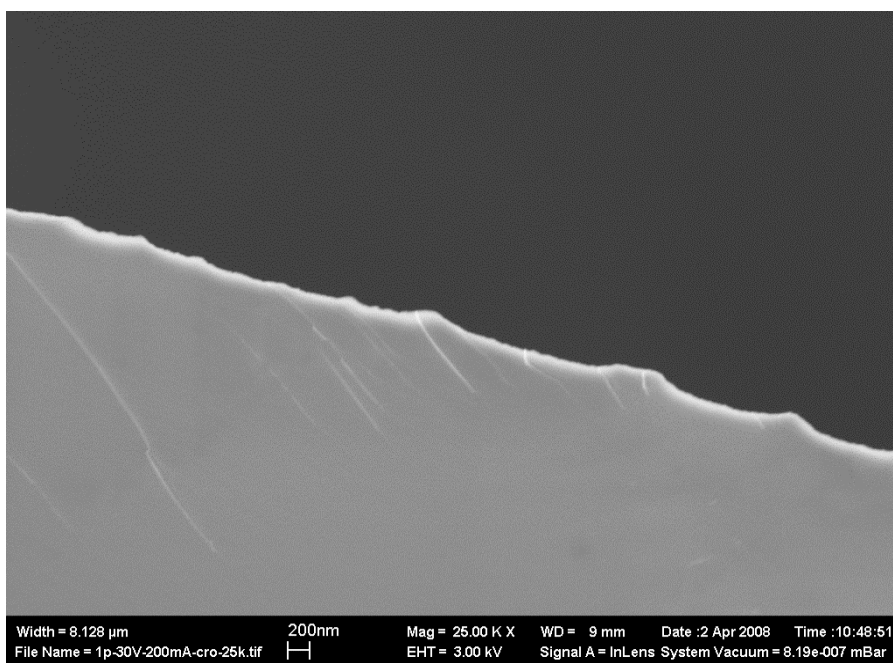


Figure 7.7. Cross-section SEM image of sample in Figure 7.6.

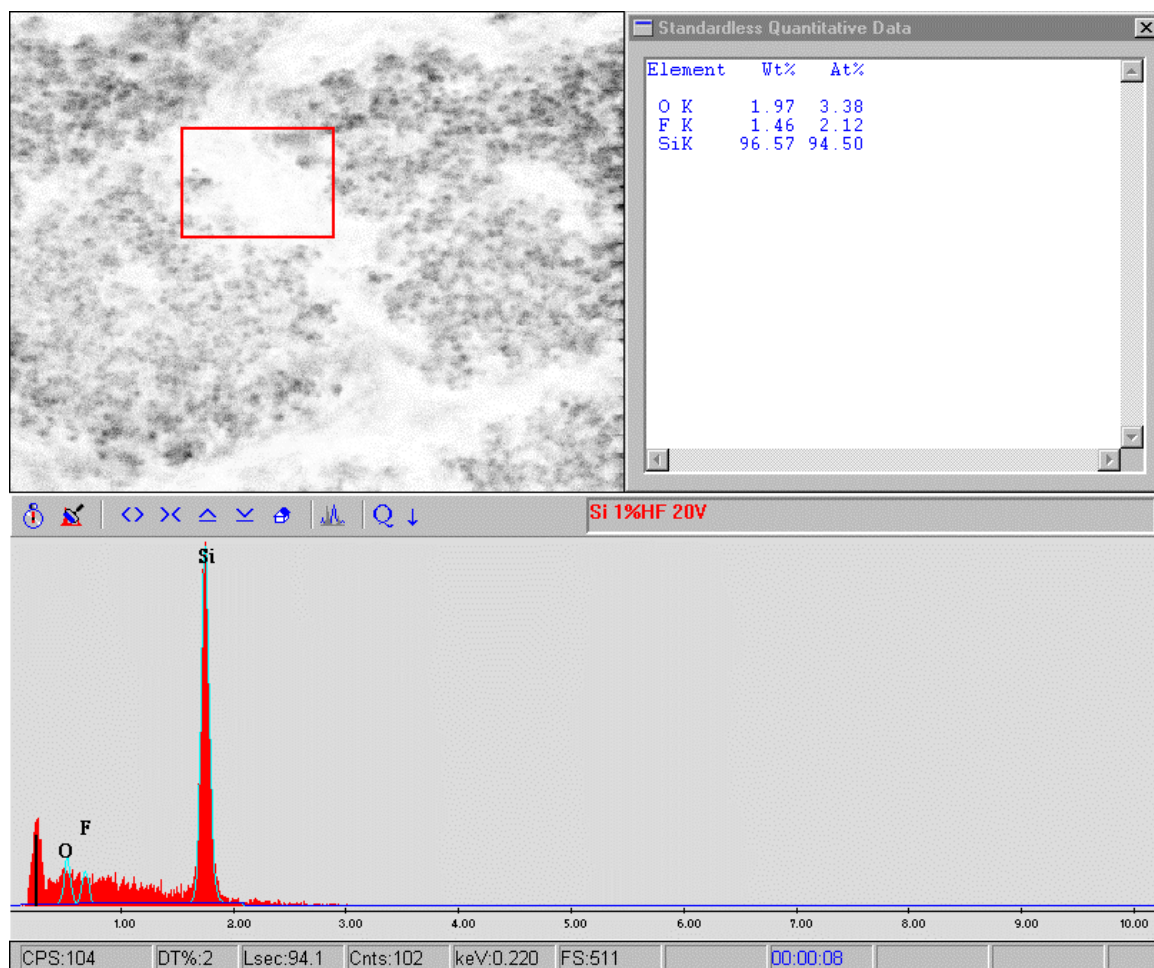


Figure 7.8. EDX of ‘fence’ structure.

7.3.3. DIMPLE PATTERN - TUNING THE ELECTROLYTE

Promising results are obtained, when samples are electropolished in a 5% HF electrolyte. As shown in the SEM image (Figure 7.9), there are some regions that possess a high degree of order, though global order is still missing. It is also noticed that during the sample preparation, there are a lot of oscillations in the current (Figure 7.10), which is linked to deteriorating the overall order of the pattern on the sample surface.

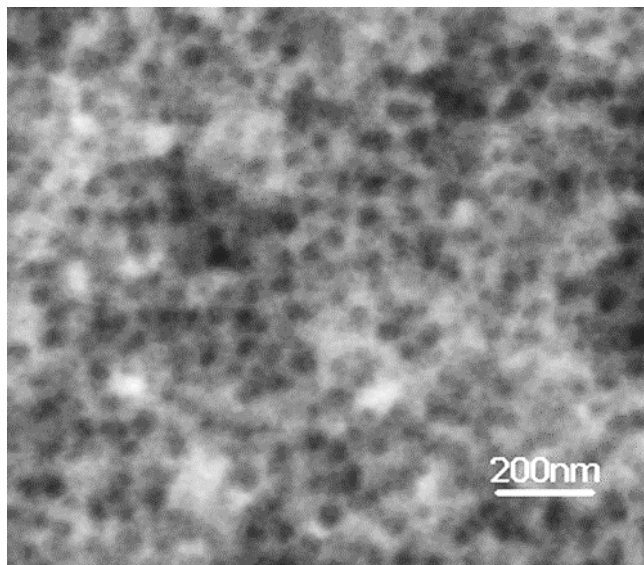


Figure 7.9. SEM of silicon electropolished at 15V in 5 percent HF for 5 minutes

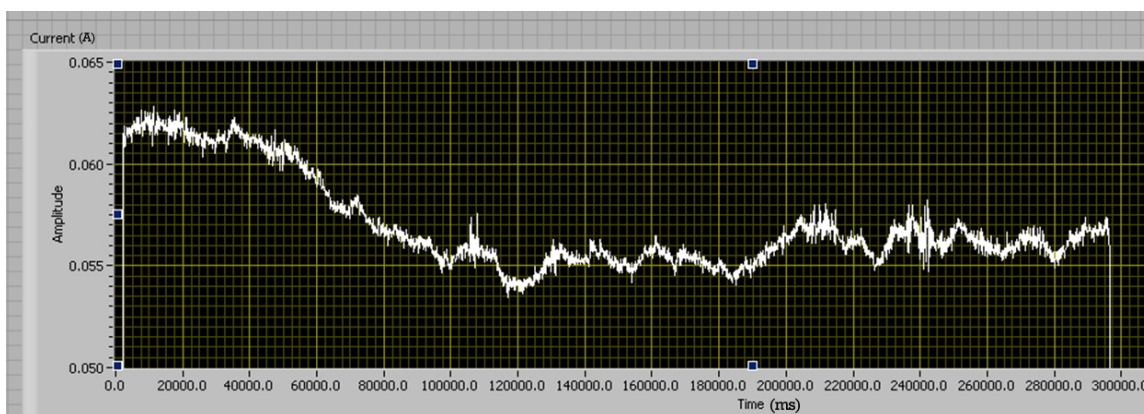


Figure 7.10 Oscillations in current during the electropolishing of silicon.

To dampen oscillations, various electrolytes have been tested, which include: 1M NaF, NH₄F (48%), acetic acid/HF, and ethylene glycol/HF.

7.3.3.1. SODIUM FLUORIDE

The reason for choosing NaF is that Na⁺ completely dissolves and ionizes in water, which can increase the overall conductivity of the electrolyte. The pH of the 1M NaF solution is within 7 and 8. SEM image (Figure 7.11) shows that the sample has

disordered nanoscale roughness on the surface. More oxide is built on the surface after the experiment, which indicates that the dissolving speed is related to the concentration of HF, not F^- .

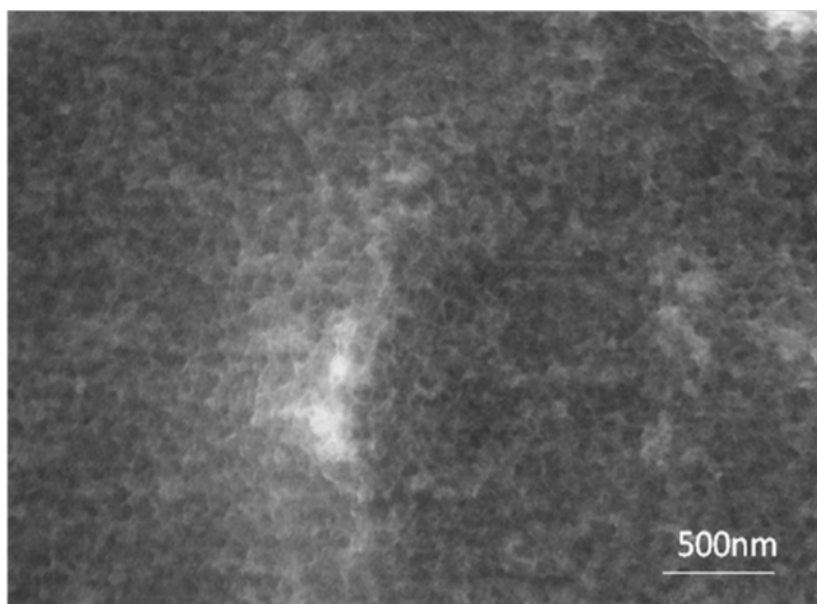


Figure 7.11. Silicon electropolished at 15V in 1M NaF

7.3.3.2. NH_4F

Ammonia fluoride has a pH between 6 and 7. When the silicon sample is treated in this electrolyte, vigorous bubbling is observed at the anode, which may be oxygen. In the end, a thick layer of oxide is left on the surface. Again, this indicates that the dissolving speed is not high enough.

The experiments with these two electrolytes give no better result than the 5% HF electrolyte, which indicates that the optimal electrolyte should still be fairly acidic.

7.3.3.3. ACETIC ACID/HF

Acetic acid, like HF, is a weak acid. A series of electrolytes with constant HF concentration (5%) and varying acetic acid concentration are tested to electropolish silicon. It is found that electrolytes with high acetic concentration (>50%) lead to the formation of porous silicon (Figure 7.12)

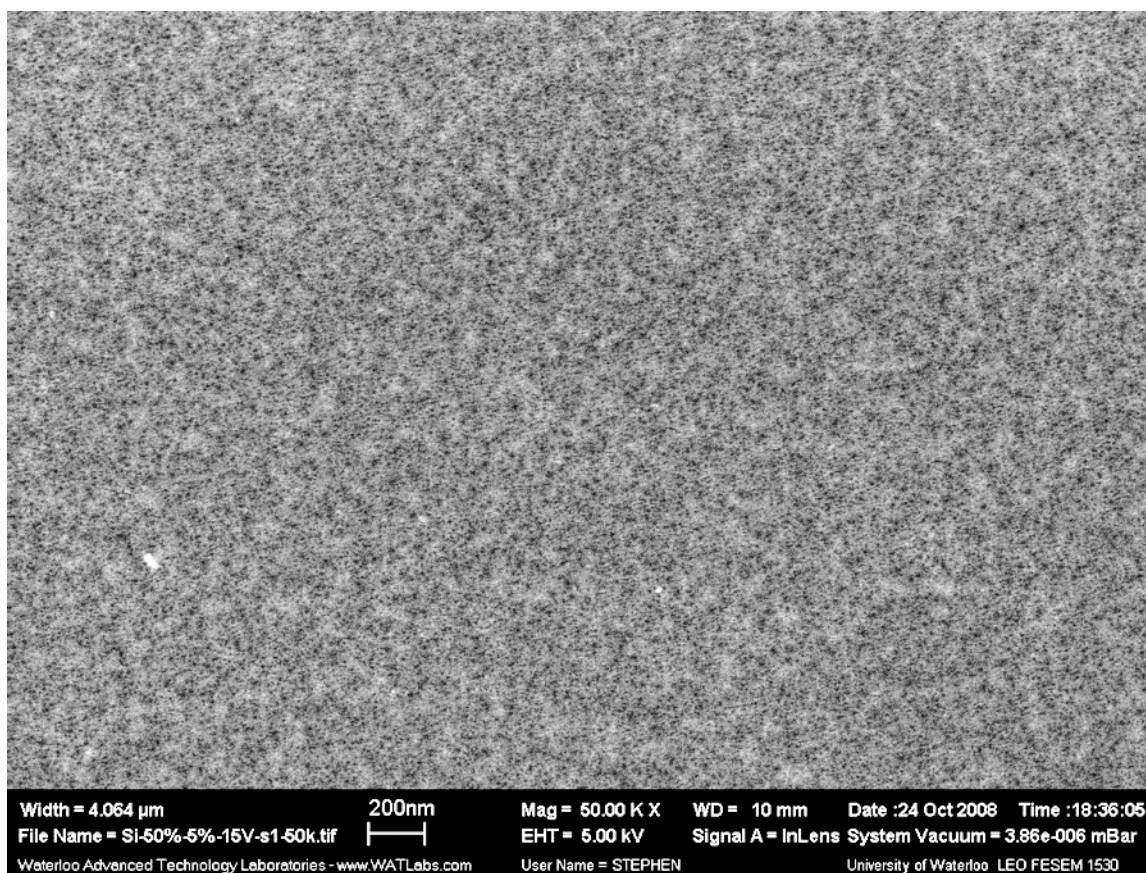


Figure 7.12. Porous silicon is achieved after the silicon sample is electropolished in 50% acetic acid with 5% HF at 15V

However, electrolyte with 40% acetic acid and 6.5% HF gave the most promising dimples ever observed (Figure 7.13), though the oscillation is still not dampened.

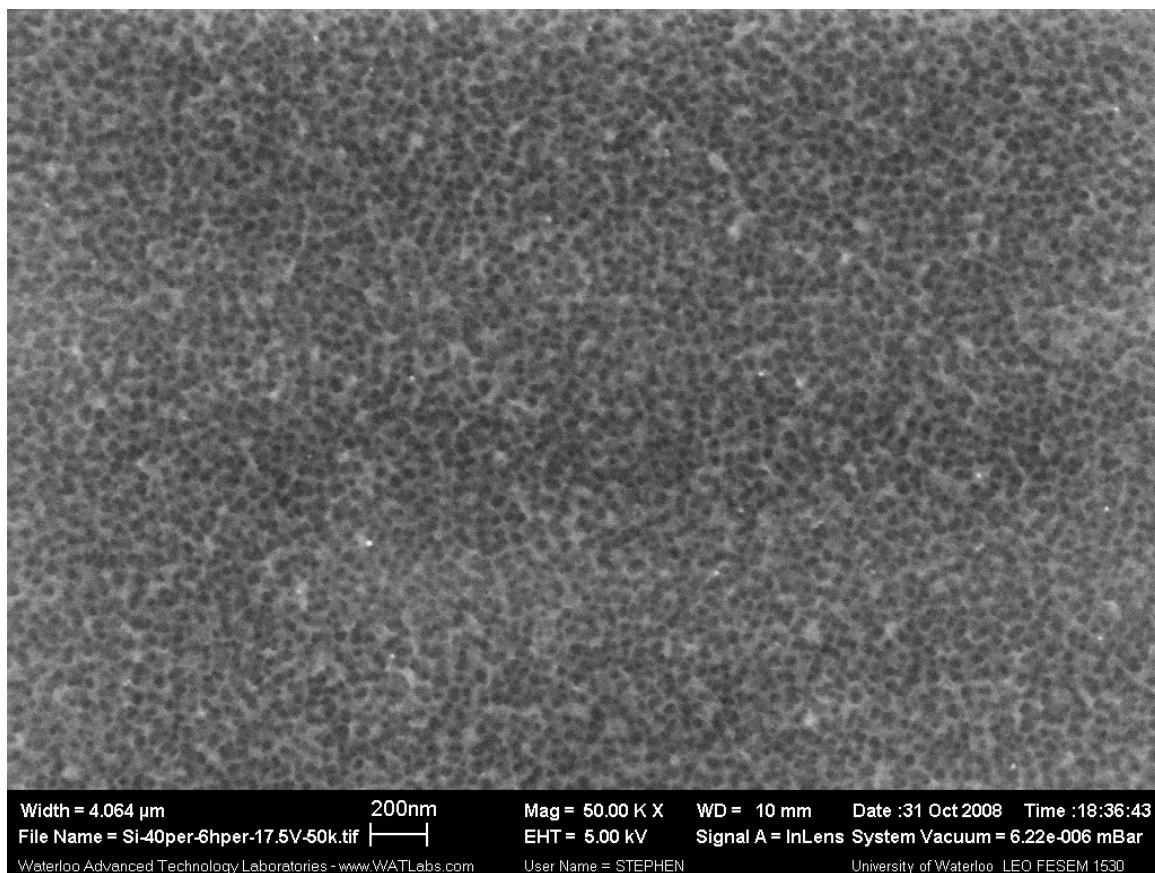


Figure 7.13. SEM image of the silicon sample electropolished in 40% acetic acid+ 6.5% HF at 17.5V for 5 minutes.

7.3.3.4. ETHYLENE GLYCOL/HF

The idea of adding ethylene glycol into the electrolyte is to increase electrolyte's viscosity, which partly mimics sulphuric acid. Besides that, ethylene glycol doesn't interfere with the pH of the electrolyte. Higher viscosity may slow down the reaction at the anode, which may help dampen the oscillation.

The volume ratio of the electrolyte tested is 4.5:1 (ethylene glycol/HF). After electropolishing, quasi-dimple pattern is observed on the surface, however, inhomogeneity of patterns is also observed. Figure 7.14 shows a series of SEM pictures

taken at the top of the sample (close to the surface of the electrolyte) to the bottom (away from the surface of the electrolyte). This indicates that the viscosity of this electrolyte is too high.

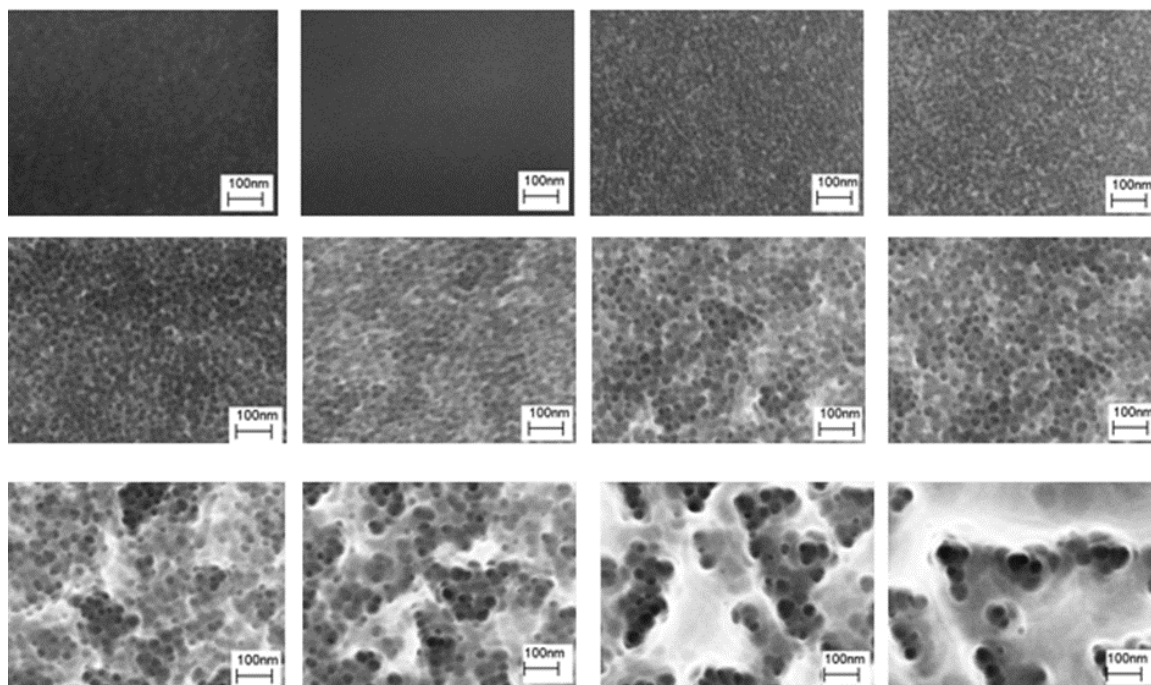


Figure 7.14. SEM of silicon electropolished in ethylene glycol (EG) and HF at 22V. The volume ratio of EG to HF is 4.5:1.

7.4. CONCLUSION

Electropolishing silicon in HF/H₂SO₄ electrolyte leads to the formation of porous silicon and yellow silicon oxide, which detaches off the surface. A white ‘fence’ structure rises on silicon samples electropolished in dilute HF solutions. EDX proves that these ‘fence’ patterns are based on silicon, not oxide. Promising results are achieved in the acetic acid/HF electrolyte. Patterns, similar to the dimple pattern, are achieved in the ethylene glycol and HF mixed electrolyte, which further study shall be based on.

CHAPTER-8

CONCLUSIONS AND OUTLOOK

“I would like to hold off on any comment on my beliefs about the cause of these strange appearances until an experimental basis can be offered to you.”

-Wilhelm Ostwald, 1900

The major impacts of this thesis work may be summarized as follows:

- The generalization of pattern formation on vanadium during electropolishing.

The window for the pattern to occur is extremely small. Novel patterns, such as pimples and labyrinths, are observed on electropolished vanadium. This pattern formation is subject to electrochemical parameters, such as electrolyte composition, electropolishing time, aspect ratio of the electrode size over the electrolyte volume. The spacing between each pattern is governed by the applied potential.

- The formation of different patterns other than dimples on tantalum during electropolishing. Additional study shows that the stripe pattern will eventually evolve into the dimple pattern over time. The size of dimples is not uniform (with bigger dimples at the receding part of the surface). It also depends on the current density during electropolishing. The transition from dimple pattern to tantalum nanotube is dependent on the water and HF concentration in the electrolyte.

- With the same method, dimple pattern has been extended onto a biomedical alloy (Ti-6V-4Al), which is extensively used for biomedical implants. The conditions for making dimples on this alloy are fine-tuned. The size of dimple is not uniform on the surface, which is subject to the surface chemical composition on the alloy. This nanopatterned alloy surface has promising application in biomedical implantation.

- Various types of disordered nanoscale patterns have been achieved on silicon *via* electropolishing. Our preliminary results show that given optimized electrolyte and potential, it is possible to generate ordered nanopattern on semiconductors *via* electropolishing, which should be of great industrial importance.

The future work can be performed under the following sections:

1. The continuing search of highly ordered electrochemical pattern formation on silicon and other semiconductors. Given the discovery of various kinds of dissipative patterns on metals *via* electropolishing, it is reasonable to postulate that such pattern could be extended onto semiconductors. Our preliminary results are very promising. The successful discovery of the dissipative pattern on semi-conductors depends on, but is not limited to, the conductivity of the electrode and the electrolyte, the dissolving speed of the oxide, and diffusion of ions.

2. Electrochemical pattern formation in benign electropolishing conditions.

Electrolytes used in this thesis contains HF or F^- , which greatly limits the techniques available to study this dissipative pattern formation as well as its potential industrial application. The search for a benign (HF-free) electrolyte, which can dissolve the anodic oxide, shall be given the same priority as the previous step.

3. Parameters controlling the pattern formation and pattern evolution. In

previous chapters, we have shown the parameters which can control the pattern formation, pattern transition, and pattern evolution. However, these are still ‘external’ parameters; the internal parameters, such as the thickness of the double layer and the ion concentration gradient, that directly link to the formation of patterns, still need investigation.

4. A progress in the physical (electrochemical layer) and mathematical model

is required to explain the pattern formation during electropolishing and predict various pattern formation on other metals and semi-conductors. With the advancement of knowledge from the previous step, a mathematical model describing the mechanism of the dissipative nanopattern formation is quite achievable. This mathematical model may also shine more lights on the electrochemical layer near the electrode during electropolishing. Furthermore, this model should be able to predict the formation of

patterns before experiments, to guide the search for patterns on other metals and semi-conductors.

BIBLIOGRAPHY

- (1) Ball, P. *The Self-Made Tapestry: Pattern Formation in Nature*; Oxford University Press: Oxford, 1998.
- (2) Kondo, S.; Miura, T. Reaction-Diffusion Model as a Framework for Understanding Biological Pattern Formation. *Science* **2010**, *329*, 1616–1620.
- (3) Theraulaz, G.; Bonabeau, E.; Nicolis, S. C.; Solé, R. V.; Fourcassié, V.; Blanco, S.; Fournier, R.; Joly, J.-L.; Fernández, P. Spatial Patterns in Ant Colonies. *Proc. Natl. Acad. Sci. U. S. A.* **2002**, *99*, 9645–9649.
- (4) Koschmieder, E. L.; Pallas, S. G. Heat Transfer through a Shallow, Horizontal Convecting Fluid Layer. *Int. J. Heat Mass Transf.* **1974**, *17*, 991–1002.
- (5) Zaikin, A. N.; Zhabotinsky, A. M. Concentration Wave Propagation in Two-Dimensional Liquid-Phase Self-Oscillating System. *Nature* **1970**, *225*, 535–537.
- (6) Cross, M.; Hohenberg, P. Pattern Formation outside of Equilibrium. *Rev. Mod. Phys.* **1993**, *65*, 851–1112.
- (7) Belousov, B. P. Periodicheski Deistvuyushchaya Reaktsia I Ee Mekhanizm [Periodically Acting Reaction and Its Mechanism]. In *Collection of abstracts on radiation medicine*; 1958; pp. 145–147.
- (8) Belousov, B. P.; Safronov, A. P. Novye Puti Kachestvennogo Analiza Kationov v Svete Izbrannoi Teorii Tsvetnosti [New Approaches to the Qualitative Analysis of Cations from the Point of View of the Selected Theory of Chromaticity]. In *Collection of abstracts on radiation medicine*; 1959; pp. 147–148.
- (9) Field, R. R. J.; Koros, E.; Noyes, R. M. R. Oscillations in Chemical Systems. II. Thorough Analysis of Temporal Oscillation in the Bromate-Cerium-Malonic Acid System. *J. Am. Chem. Soc.* **1972**, *381*, 8649–8664.
- (10) Field, R.; Burger, M. *Oscillations and Traveling Waves in Chemical Systems*; Wiley: New York, 1985.
- (11) Turing, A. M. The Chemical Basis of Morphogenesis. *Philos. Trans. R. Soc. B Biol. Sci.* **1952**, *237*, 37–72.
- (12) Singh, S. Dissipative Nanopatterning of Surfaces, McMaster, 2008.

- (13) Ouyang, Q.; Swinney, H. Transition from a Uniform State to Hexagonal and Striped Turing Patterns. *Nature* **1991**, *352*, 610–612.
- (14) Castets, V.; Dulos, E.; Boissonade, J.; Kepper, P. De. Experimental Evidence of a Sustained Standing Turing-Type Nonequilibrium Chemical Pattern. *Phys. Rev. Lett.* **1990**, *64*, 2953–2957.
- (15) Lengyel, I.; Epstein, I. R. Modeling of Turing Structures in the Chlorite-Iodide-Malonic Acid-Starch Reaction System. *Science* **1991**, *251*, 650–652.
- (16) Barrio, R. A.; Varea, C.; Aragón, J. L.; Maini, P. K. A Two-Dimensional Numerical Study of Spatial Pattern Formation in Interacting Turing Systems. *Bull. Math. Biol.* **1999**, *61*, 483–505.
- (17) Gierer, A.; Meinhardt, H. A Theory of Biological Pattern Formation. *Kybernetik* **1972**, *12*, 30–39.
- (18) Murray, J. Discussion: Turing's Theory of Morphogenesis—its Influence on Modelling Biological Pattern and Form. *Bull. Math. Biol.* **1990**, *52*, 119–152.
- (19) Painter, K. J.; Maini, P. K.; Othmer, H. G. Stripe Formation in Juvenile Pomacanthus Explained by a Generalized Turing Mechanism with Chemotaxis. *Proc. Natl. Acad. Sci. U. S. A.* **1999**, *96*, 5549–5554.
- (20) Harris, M. P.; Williamson, S.; Fallon, J. F.; Meinhardt, H.; Prum, R. O. Molecular Evidence for an Activator-Inhibitor Mechanism in Development of Embryonic Feather Branching. *Proc. Natl. Acad. Sci. U. S. A.* **2005**, *102*, 11734–11739.
- (21) Segel, L. A.; Jackson, J. L. Dissipative Structure: An Explanation and an Ecological Example. *J. Theor. Biol.* **1972**, *37*, 545–559.
- (22) Prigogine, I. *Self-Organization in Non-Equilibrium Systems*; Wiley: New York, 1977.
- (23) Whitesides, G. M.; Grzybowski, B. Self-Assembly at All Scales. *Science* **2002**, *295*, 2418–2421.
- (24) Whitesides, G. M.; Boncheva, M. Beyond Molecules: Self-Assembly of Mesoscopic and Macroscopic Components. *Proc. Natl. Acad. Sci. U. S. A.* **2002**, *99*, 4769–4774.
- (25) Glansdorff, P.; Prigogine, I. *Thermodynamic Theory of Structure, Stability and Fluctuations*; Wiley-Interscience: London, 1971.

- (26) Krischer, K.; Mazouz, N.; Grauel, P. Fronts, Waves, and Stationary Patterns in Electrochemical Systems. *Angew. Chem., Int. Ed.* **2001**, *40*, 850–869.
- (27) Fechner, G. T. Über Umkehrungen Der Polarität in Der Einfachen Kette. *SCHWEIGGER'S J. FÜR CHEMIE UND Phys.* **1828**, *53*, 129–151.
- (28) Beni, G.; Hackwood, S. Intermittent Turbulence and Period Doubling at the Corrosion-Pitting Transition in Iron. *J. Appl. Electrochem.* **1984**, *14*, 623.
- (29) Li, Y.; Oslonovitch, J.; Mazouz, N.; Plenge, F. Turing-Type Patterns on Electrode Surfaces. *Science* **2001**, *291*, 2395–2398.
- (30) Krischer, K. Spontaneous Formation of Spatiotemporal Patterns at the Electrode|electrolyte Interface. *J. Electroanal. Chem.* **2001**, *501*, 1–21.
- (31) Bard, A. A. J.; Faulkner, L. R. L.; Swain, E.; Robey, C. *Electrochemical Methods: Fundamentals and Applications*; 2nd ed.; John Wiley & Sons, INC.: New York, 1980.
- (32) Winkler, I.; Plevan, I.; Nechiporuk, V. Region of Occurrence of Convective Cells in the Cu^{2+} / Cu Electrochemical System. *Electrochim. Acta* **1996**, *41*, 2743–2745.
- (33) Baranowski, B.; Kawczyński, A. Experimental Determination of the Critical Rayleigh Number in Electrolyte Solutions with Concentration Polarization. *Electrochim. Acta* **1972**, *17*, 695–699.
- (34) Tassel, J. Van; Randall, C. Ionic Gradients at an Electrode above the Equilibrium Limit Current. 3. Stabilization of Ion Depleted Conduction by a Nanoporous Alumina Layer during Electrophoretic. *J. Phys. Chem. C* **2007**, *111*, 3358–3365.
- (35) Tassel, J. Van; Randall, C. Ionic Gradients at an Electrode above the Equilibrium Limit Current. 2. Transition to Convection. *J. Phys. Chem. C* **2007**, *111*, 3349–3357.
- (36) Dini, D.; Doblhofer, K.; Ertl, G. Nucleation of Solution Convection Channels as the First Step in Electro-Hydrodynamic Pattern Formation. *Phys. Chem. Chem. Phys.* **2000**, *2*, 1183–1186.
- (37) Orlik, M.; Rosenmund, J.; Doblhofer, K.; Ertl, G. Electrochemical Formation of Luminescent Convective Patterns in Thin-Layer Cells. *J. Phys. Chem. B* **1998**, *5647*, 1397–1403.
- (38) Nakabayashi, S.; Yanagida, M.; Uosaki, K. Dissipation Structure of Electrochemical Hydrodynamic Convection. *J. Phys. Chem.* **1996**, *100*, 714–717.

- (39) Krastev, I.; Koper, M. Pattern Formation during the Electrodeposition of a Silver-Antimony Alloy. *Physica A* **1995**, *213*, 199–208.
- (40) Joule, J. XX. On the Intermittent Character of the Voltaic Current in Certain Cases of Electrolysis; and on the Intensities of Various Voltaic Arrangements. *Philos. Mag.* **1844**, *26*, 106.
- (41) Ostwald, W. Periodische Erscheinungen Bei Der Auflösung Des Chrom in Säuren, 2. Mitteilung. *Zeitschrift für Phys. Chemie* **1900**, *35*, 204–256.
- (42) Nicolis, G. *Introduction to Nonlinear Science*; Cambridge University Press: Cambridge, 1995.
- (43) Koper, M. T. M. Non-Linear Phenomena in Electrochemical Systems. *J. Chem. Soc. Faraday Trans.* **1998**, *94*, 1369–1378.
- (44) Koper, M. The Theory of Electrochemical Instabilities. *Electrochim. Acta* **1992**, *37*, 1771–1778.
- (45) Lev, O.; Sheintuch, M.; Pisemen, L.; Yarnitzky, C. Standing and Propagating Wave Oscillations in the Anodic Dissolution of Nickel. *Nature* **1988**, *336*, 458–459.
- (46) Otterstedt, R.; Jaeger, N.; Plath, P.; Hudson, J. Wave Instabilities in an Excitable Electrochemical System. *Phys. Rev. E* **1998**, *58*, 6810–6813.
- (47) Strasser, P.; Christoph, J.; Lin, W.-F.; Eiswirth, M.; Hudson, J. L. Standing Wave Oscillations in an Electrocatalytic Reaction. *J. Phys. Chem. A* **2000**, *104*, 1854–1860.
- (48) Flätgen, G.; Krischer, K. Accelerating Fronts in an Electrochemical System due to Global Coupling. *Phys. Rev. E* **1995**, *51*, 3997–3998.
- (49) Flätgen, G.; Krischer, K.; Pettinger, B. Two-Dimensional Imaging of Potential Waves in Electrochemical Systems by Surface Plasmon Microscopy. *Science* **1995**, *269*, 668–671.
- (50) Haim, D.; Lev, O. Modeling Periodic and Chaotic Dynamics in Anodic Nickel Dissolution. *J. Phys. Chem.* **1992**, *96*, 2676–2681.
- (51) Haim, D.; Lev, O.; Pismen, L.; Sheintuch, M. Modelling Spatiotemporal Patterns in Anodic Nickel Dissolution. *Chem. Eng. Sci.* **1992**, *47*, 3907–3913.

- (52) Hudson, J.; Tabora, J.; Krischer, K.; Kevrekidis, I. Spatiotemporal Period Doubling during the Electrodisolution of Iron. *Phys. Lett. A* **1993**, *179*, 355–363.
- (53) Christoph, J.; Eiswirth, M. Theory of Electrochemical Pattern Formation. *Chaos* **2002**, *12*, 215–230.
- (54) Ross, J.; Arkin, A.; Mueller, S. Experimental Evidence for Turing Structures. *J. Phys. Chem.* **1995**, *99*, 10417–10419.
- (55) Flätgen, G.; Krischer, K. A General Model for Pattern Formation in Electrode Reactions. *J. Chem. Phys.* **1995**, *103*, 5428–5436.
- (56) Manickam, D. A.; Wang, Y.; Pantaleo, A. N.; Kruse, P. *Oscillations and Mesa Formation during Anodic Dissolution of Nickel in Highly Concentrated Sulfuric Acid*.
- (57) Feynman, R. There Is Plenty of Room at the Bottom. *Caltech Eng. Sci.* **1960**, *23*, 22–36.
- (58) Dos Santos Claro, P. C.; Castez, M. F.; Schilardi, P. L.; Luque, N. B.; Leiva, E. P. M.; Salvarezza, R. C. Spontaneous Nanoripple Formation on Metallic Templates. *ACS Nano* **2008**, *2*, 2531–2539.
- (59) Gates, B.; Xu, Q.; Stewart, M.; Ryan, D. New Approaches to Nanofabrication: Molding, Printing, and Other Techniques. *Chem. Rev.* **2005**, *105*, 1171–1196.
- (60) Cullis, A.; Canham, L. Visible Light Emission due to Quantum Size Effects in Highly Porous Crystalline Silicon. *Nature* **1991**, *353*, 335–338.
- (61) Xie, J.; Luan, B. Nanometer-scale Surface Modification of Ti6Al4V Alloy for Orthopedic Applications. *J. Biomed. Mater. Res. A* **2008**, *84A*, 63–72.
- (62) Singh, S.; Barden, W.; Kruse, P. Nanopatterning of Transition Metal Surfaces via Electrochemical Dimple Array Formation. *ACS Nano* **2008**, *2*, 2453–2464.
- (63) Hillebrand, R.; Muller, F.; Schwirn, K.; Lee, W.; Steinhart, M. Quantitative Analysis of the Grain Morphology in Self-Assembled Hexagonal Lattices. *ACS Nano* **2008**, *2*, 913–920.
- (64) Lee, W.; Ji, R.; Gösele, U.; Nielsch, K. Fast Fabrication of Long-Range Ordered Porous Alumina Membranes by Hard Anodization. *Nat. Mater.* **2006**, *5*, 741–747.
- (65) Li, F.; Zhang, L.; Metzger, R. On the Growth of Highly Ordered Pores in Anodized Aluminum Oxide. *Chem. Mater.* **1998**, *10*, 2470–2480.

- (66) Nielsch, K.; Choi, J.; Schwirn, K.; Wehrspohn, R. B.; Gösele, U. Self-Ordering Regimes of Porous Alumina: The 10 Porosity Rule. *Nano Lett.* **2002**, *2*, 677–680.
- (67) Schwirn, K.; Lee, W.; Hillebrand, R. Self-Ordered Anodic Aluminum Oxide Formed by H₂SO₄ Hard Anodization. *ACS Nano* **2008**, *2*, 302–310.
- (68) Li, A. P.; Müller, F.; Birner, A.; Nielsch, K.; Gösele, U. Hexagonal Pore Arrays with a 50–420 Nm Interpore Distance Formed by Self-Organization in Anodic Alumina. *J. Appl. Phys.* **1998**, *84*, 6023.
- (69) Masuda, H.; Fukuda, K. Ordered Metal Nanohole Arrays Made by a Two-Step Replication of Honeycomb Structures of Anodic Alumina. *Science* **1995**, *268*, 1466–1468.
- (70) Jessensky, O.; Müller, F.; Gösele, U. Self-Organized Formation of Hexagonal Pore Arrays in Anodic Alumina. *Appl. Phys. Lett.* **1998**, *72*, 1173–1175.
- (71) Macak, J.; Tsuchiya, H.; Schmuki, P. High-Aspect-Ratio TiO₂ Nanotubes by Anodization of Titanium. *Angew. Chem., Int. Ed.* **2005**, *44*, 2100–2102.
- (72) Zhang, W.; Xi, Z.; Li, G.; Wang, Q.; Tang, H.; Liu, Y.; Zhao, Y.; Jiang, L. Highly Ordered Coaxial Bimodal Nanotube Arrays Prepared by Self-Organizing Anodization on Ti Alloy. *Small* **2009**, *5*, 1742–1746.
- (73) Tang, X.; Li, D. Fabrication, Geometry, and Mechanical Properties of Highly Ordered TiO₂ Nanotubular Arrays. *J. Phys. Chem. C* **2009**, *113*, 7107–7113.
- (74) Wei, W.; Macak, J. M.; Schmuki, P. High Aspect Ratio Ordered Nanoporous Ta₂O₅ Films by Anodization of Ta. *Electrochem. Commun.* **2008**, *10*, 428–432.
- (75) Allam, N. N. K. N.; Feng, X. J. X.; Grimes, C. C. A. Self-Assembled Fabrication of Vertically Oriented Ta₂O₅ Nanotube Arrays, and Membranes Thereof, by One-Step Tantalum Anodization. *Chem. Mater.* **2008**, *20*, 6477–6481.
- (76) Barton, J. E.; Stender, C. L.; Li, P.; Odom, T. W. Structural Control of Anodized Tantalum Oxide Nanotubes. *J. Mater. Chem.* **2009**, *19*, 4896–4898.
- (77) Yang, Y.; Albu, S. P.; Kim, D.; Schmuki, P. Enabling the Anodic Growth of Highly Ordered V₂O₅ Nanoporous/nanotubular Structures. *Angew. Chem., Int. Ed.* **2011**, *50*, 9071–9075.
- (78) Macak, J. M.; Tsuchiya, H.; Taveira, L.; Ghicov, A.; Schmuki, P. Self-Organized Nanotubular Oxide Layers on Ti-6Al-7Nb and Ti-6Al-4V Formed by Anodization in NH₄F Solutions. *J. Biomed. Mater. Res. A* **2005**, *75*, 928–933.

- (79) Ruckh, T.; Porter, J. R.; Allam, N. K.; Feng, X.; Grimes, C. a; Popat, K. C. Nanostructured Tantalum as a Template for Enhanced Osseointegration. *Nanotechnology* **2009**, *20*, 045102.
- (80) Rani, S.; Roy, S. C.; Paulose, M.; Varghese, O. K.; Mor, G. K.; Kim, S.; Yoriya, S.; Latempa, T. J.; Grimes, C. A. Synthesis and Applications of Electrochemically Self-Assembled Titania Nanotube Arrays. *Phys. Chem. Chem. Phys.* **2010**, *12*, 2780–2800.
- (81) Yang, Y.; Peng, Z.; Wang, G.; Ruan, G.; Fan, X.; Li, L.; Fei, H. Three-Dimensional Thin Film for Lithium-Ion Batteries and Supercapacitors. *ACS Nano* **2014**, *8*, 7279–7287.
- (82) Li, P.; Stender, C. L.; Ringe, E.; Marks, L. D.; Odom, T. W. Synthesis of TaS₂ Nanotubes from Ta₂O₅ Nanotube Templates. *Small* **2010**, *6*, 1096–1099.
- (83) El-sayed, H. A.; Birss, V. I. Controlled Interconversion of Nanoarray of Ta Dimples and High Aspect Ratio Ta Oxide Nanotubes. *Nano Lett.* **2009**, *9*, 20–25.
- (84) Houser, J.; Hebert, K. The Role of Viscous Flow of Oxide in the Growth of Self-Ordered Porous Anodic Alumina Films. *Nat. Mater.* **2009**, *8*, 415–420.
- (85) Hebert, K.; Albu, S.; Paramasivam, I.; Schmuki, P. Morphological Instability Leading to Formation of Porous Anodic Oxide Films. *Nat. Mater.* **2012**, *11*, 162–166.
- (86) Chen, W.; Lai, M.; Tsai, K. Spontaneous Formation of Ordered Nanobubbles in Anodic Tungsten Oxide during Anodization. *J. Phys. Chem. C* **2011**, *115*, 18406–18411.
- (87) Zhu, X.; Song, Y.; Yu, D.; Zhang, C.; Yao, W. A Novel Nanostructure Fabricated by an Improved Two-Step Anodizing Technology. *Electrochem. Commun.* **2013**, *29*, 71–74.
- (88) Ruiquan, Y.; Longfei, J.; Xufei, Z.; Ye, S.; Dongliang, Y.; Aijun, H. Theoretical Derivation of Ionic Current and Electronic Current and Comparison between Fitting Curves and Measured Curves. *RSC Adv.* **2012**, *2*, 12474.
- (89) Roy, P.; Berger, S.; Schmuki, P. TiO₂ Nanotubes: Synthesis and Applications. *Angew. Chem., Int. Ed.* **2011**, *50*, 2904–2939.
- (90) Ghicov, A.; Schmuki, P. Self-Ordering Electrochemistry: A Review on Growth and Functionality of TiO₂ Nanotubes and Other Self-Aligned MO_x Structures. *Chem. Commun.* **2009**, 2791–2808.

- (91) El-Sayed, H.; Birss, V. Controlled Growth and Monitoring of Tantalum Oxide Nanostructures. *Nanoscale* **2010**, *2*, 793–798.
- (92) Zhao, G.-Y.; Xu, C.-L.; Guo, D.-J.; Li, H.; Li, H.-L. Patterning Polycrystalline Aluminum by Electropolishing at Low Voltages. *J. Solid State Electrochem.* **2005**, *10*, 266–269.
- (93) Sarkar, J.; Khan, G.; Basumallick, A. The Microscopic Origin of Self-Organized Nanostripe Pattern Formation on an Electropolished Aluminium Surface. *Nanotechnology* **2009**, *20*, 1–7.
- (94) Ricker, R. E.; Miller, A. E.; Yue, D. F.; Banerjee, G.; Bandyopadhyay, S. Nanofabrication of a Quantum Dot Array: Atomic Force Microscopy of Electropolished Aluminum. *J. Electron. Mater.* **1996**, *25*, 1585–1592.
- (95) Bandyopadhyay, S.; Miller, A. E.; Chang, H. C.; Banerjee, G.; Yuzhakov, V.; Yue, D.-F.; Ricker, R. E.; Jones, S.; Eastman, J. Electrochemically Assembled Quasi-Periodic Quantum Dot Arrays. *Nanotechnology* **1996**, *7*, 360–371.
- (96) Kong, L.-B.; Huang, Y.; Guo, Y.; Li, H.-L. A Facile Approach to Preparation of Nanostripes on the Electropolished Aluminum Surface. *Mater. Lett.* **2005**, *59*, 1656–1659.
- (97) Yuzhakov, V.; Chang, H.; Miller, A. Pattern Formation during Electropolishing. *Phys. Rev. B* **1997**, *56*, 12608–12624.
- (98) Yuzhakov, V.; Takhistov, P. Pattern Selection during Electropolishing due to Double-Layer Effects. *Chaos* **1999**, *9*, 62–77.
- (99) Konovalov, V.; Zangari, G.; Metzger, R. Highly Ordered Nanotopographies on Electropolished Aluminum Single Crystals. *Chem. Mater.* **1999**, *11*, 1997–1999.
- (100) Guo, W.; Johnson, D. Role of Interfacial Energy during Pattern Formation of Electropolishing. *Phys. Rev. B* **2003**, *67*, 075411.
- (101) Guo, W.; Johnson, D. T. Pattern Selection with Anisotropy during Aluminum Electropolishing. *J. Cryst. Growth* **2004**, *268*, 258–271.
- (102) El-Sayed, H.; Singh, S.; Greiner, M. T.; Kruse, P. Formation of Highly Ordered Arrays of Dimples on Tantalum at the Nanoscale. *Nano Lett.* **2006**, *6*, 2995–2999.
- (103) El-Sayed, H.; Singh, S.; Kruse, P. Formation of Dimpled Tantalum Surfaces from Electropolishing. *J. Electrochem. Soc.* **2007**, *154*, C728–C732.

- (104) Caicedo-Martinez, C. E.; Koroleva, E. V.; Thompson, G. E.; Skeldon, P.; Shimizu, K.; Habazaki, H.; Hoellrigl, G. Surface Nanotextures on Aluminium. *Surf. Interface Anal.* **2002**, *34*, 405–408.
- (105) Vignal, V.; Roux, J.; Flandrois, S.; Fevrier, A. Nanoscopic Studies of Stainless Steel Electropolishing. *Corros. Sci.* **2000**, *42*, 1041–1053.
- (106) Tsuchiya, H.; Suzumura, T.; Terada, Y.; Fujimoto, S. Formation of Self-Organized Pores on Type 316 Stainless Steel in Organic Solvents. *Electrochim. Acta* **2012**, *82*, 333–338.
- (107) Datta, M. Anodic Dissolution of Metals at High Rates. *IBM J. Res. Dev.* **1993**, *31*, 207–225.
- (108) Hudson, J.; Tsotsis, T. Electrochemical Reaction Dynamics: A Review. *Chem. Eng. Sci.* **1994**, *49*, 1493–1572.
- (109) Awez Mohammad, A.; Arnott, Z. L.; Wang, Y.; Kruse, P. Note: Benign and Reproducible Preparation of Titanium Tips. *Rev. Sci. Instrum.* **2014**, *85*, 026113.
- (110) Gault, B.; Moody, M. P.; Cairney, J. M.; Ringer, S. P. *Atom Probe Microscopy*; Springer: New York, 2012.
- (111) ASTM. Annual Book of ASTM Standards, 1979.
- (112) Landolt, D.; Chauvy, P.-F.; Zinger, O. Electrochemical Micromachining, Polishing and Surface Structuring of Metals: Fundamental Aspects and New Developments. *Electrochim. Acta* **2003**, *48*, 3185–3201.
- (113) Lin, C.; Hu, C. Electropolishing of 304 Stainless Steel: Surface Roughness Control Using Experimental Design Strategies and a Summarized Electropolishing Model. *Electrochim. Acta* **2008**, *53*, 3356–3363.
- (114) Landolt, D. Fundamental Aspects of Electropolishing. *Electrochim. Acta* **1987**, *32*, 1–11.
- (115) Kirchheim, R.; Major, K.; Tiffl, G. Diffusion and Solid-Film Formation during Electropolishing of Metals. *J. Electrochem. Soc.* **1981**, *128*, 1027–1034.
- (116) Datta, M.; Vercruysse, D. Transpassive Dissolution of 420 Stainless Steel in Concentrated Acids under Electropolishing Conditions. *J. Electrochem. Soc.* **1990**, *137*, 3016–3023.

- (117) Fang, J.; Wu, N. XPS and AES Studies of the Composition of the Viscous Liquid Film in the Electropolishing of Copper. *J. Appl. Electrochem.* **1990**, *20*, 231–234.
- (118) Fang, J.; Wu, N. Determination of the Composition of Viscous Liquid Film on Electropolishing Copper Surface by XPS and AES. *J. Electrochem. Soc.* **1989**, *136*, 3800–3803.
- (119) Matlosz, M. Modeling of Impedance Mechanisms in Electropolishing. *Electrochim. Acta* **1995**, *40*, 393–401.
- (120) Edwards, J. The Mechanism of Electropolishing of Copper in Phosphoric Acid Solutions. *J. Electrochem. Soc.* **1953**, *100*, 189C–194C.
- (121) Abbott, A. P.; Capper, G.; McKenzie, K. J.; Ryder, K. S. Voltammetric and Impedance Studies of the Electropolishing of Type 316 Stainless Steel in a Choline Chloride Based Ionic Liquid. *Electrochim. Acta* **2006**, *51*, 4420–4425.
- (122) Glarum, S. H.; Marshall, J. H. The Anodic Dissolution of Copper into Phosphoric Acid. *J. Electrochem. Soc.* **1985**, *132*, 2872–2878.
- (123) Alanis, I.; Schiffrin, D. The Influence of Mass Transfer on the Mechanism of Electropolishing of Nickel in Aqueous Sulphuric Acid. *Electrochim. Acta* **1982**, *27*, 837–845.
- (124) Kuo, H. C.; Landolt, D. Rotating Disc Electrode Study of Anodic Dissolution of Iron in Concentrated Chloride Media. *Electrochim. Acta* **1975**, *20*, 393–399.
- (125) Higgins, J. K. The Anodic Dissolution and Electrolytic Polishing of Metals. *J. Electrochem. Soc.* **1959**, *106*, 999–1005.
- (126) Datta, M.; Landolt, D. On the Role of Mass Transport in High Rate Dissolution of Iron and Nickel in ECM electrolytes—I. Chloride Solutions. *Electrochim. Acta* **1980**, *25*, 1255–1262.
- (127) Landolt, D.; Muller, R.; Tobias, C. W. High Rate Anodic Dissolution of Copper. *J. Electrochem. Soc.* **1969**, *116*, 1384–1390.
- (128) Datta, M.; Landolt, D. Surface Brightening during High Rate Nickel Dissolution in Nitrate Electrolytes. *J. Electrochem. Soc.* **1975**, *122*, 1466–1472.
- (129) Datta, M.; Landolt, D. On the Influence of Electrolyte Concentration, pH and Temperature on Surface Brightening of Nickel under ECM Conditions. *J. Appl. Electrochem.* **1977**, *7*, 247–252.

- (130) Datta, M.; Landolt, D. On the Role of Mass Transport in High Rate Dissolution of Iron and Nickel in ECM electrolytes—II. Chlorate and Nitrate Solutions. *Electrochim. Acta* **1980**, *25*, 1263–1271.
- (131) Pauric, A. D.; Baig, S. A.; Pantaleo, A. N.; Wang, Y.; Kruse, P. Sponge-Like Porous Metal Surfaces from Anodization in Very Concentrated Acids. *J. Electrochem. Soc.* **2012**, *160*, C12–C18.
- (132) Binnig, G.; Quate, C.; Gerber, C. Atomic Force Microscope. *Phys. Rev. Lett.* **1986**, *56*, 930–934.
- (133) Martin, Y.; Williams, C. C.; Wickramasinghe, H. K. Atomic Force Microscope–force Mapping and Profiling on a Sub 100-Å Scale. *J. Appl. Phys.* **1987**, *61*, 4723–4730.
- (134) Randolph, S. J.; Fowlkes, J. D.; Rack, P. D. Focused, Nanoscale Electron-Beam-Induced Deposition and Etching. *Crit. Rev. Solid State Mater. Sci.* **2006**, *31*, 55–89.
- (135) Kruse, P. Chemical Characterization of Biological and Technological Surfaces. In *Functional Properties of Bio-Inspired Surfaces: Characterization and Technological applications*; Favret, E.; Fuentes, N., Eds.; 2009; pp. 233–277.
- (136) Cardarelli, F. Less Common Nonferrous Metals. In *Materials Handbook*; Cardarelli, F., Ed.; Springer: London, 2008; pp. 213–454.
- (137) Kolasinski, K.; Barclay, W. The Stoichiometry of Electroless Silicon Etching in Solutions of V₂O₅ and HF. *Angew. Chem., Int. Ed.* **2013**, *52*, 6731–6734.
- (138) ImageJ <http://imagej.nih.gov/ij/> (accessed Jul 21, 2014).
- (139) Radial Profile Plot <http://rsb.info.nih.gov/ij/plugins/radial-profile.html> (accessed Jul 21, 2014).
- (140) Weissler, A. Formation of Hydrogen Peroxide by Ultrasonic Waves: Free Radicals. *J. Am. Chem. Soc.* **1959**, *332*, 1077–1081.
- (141) Kim, H.; Miyaji, F. Preparation of Bioactive Ti and Its Alloys via Simple Chemical Surface Treatment. *J. Biomed. Mater. Res. A* **1996**, *32*, 409–417.
- (142) Stevens, M. M.; George, J. H. Exploring and Engineering the Cell Surface Interface. *Science* **2005**, *310*, 1135–1138.

- (143) Bettinger, C.; Zhang, Z.; Gerecht, S.; Borenstein, J.; Langer, R. Enhancement of in Vitro Capillary Tube Formation by Substrate Nanotopography. *Adv. Mater.* **2008**, *20*, 99–103.
- (144) Park, J.; Bauer, S.; Schmuki, P.; von der Mark, K.; Mark, K. Von Der. Narrow Window in Nanoscale Dependent Activation of Endothelial Cell Growth and Differentiation on TiO₂ Nanotube Surfaces. *Nano Lett.* **2009**, *9*, 3157–3164.
- (145) Huang, J.; Grater, S.; Corbellini, F.; Rinck, S.; Bock, E.; Kemkemer, R.; Kessler, H.; Ding, J.; Spatz, J. Impact of Order and Disorder in RGD Nanopatterns on Cell Adhesion. *Nano Lett.* **2009**, *9*, 1111–1116.
- (146) Park, J.; Bauer, S.; Schlegel, K. A.; Neukam, F. W.; von der Mark, K.; Schmuki, P. TiO₂ Nanotube Surfaces: 15 Nm--an Optimal Length Scale of Surface Topography for Cell Adhesion and Differentiation. *Small* **2009**, *5*, 666–671.
- (147) Richert, L.; Vetrone, F.; Yi, J.-H.; Zalzal, S. F.; Wuest, J. D.; Rosei, F.; Nanci, A. Surface Nanopatterning to Control Cell Growth. *Adv. Mater.* **2008**, *20*, 1488–1492.
- (148) Hovgaard, M.; Rechendorff, K. Fibronectin Adsorption on Tantalum: The Influence of Nanoroughness. *J. Phys. Chem. B* **2008**, *112*, 8241–8249.
- (149) Dolatshahi-Pirouz, A.; Jensen, T.; Kraft, D. Fibronectin Adsorption, Cell Adhesion, and Proliferation on Nanostructured Tantalum Surfaces. *ACS Nano* **2010**, *4*, 2874–2882.
- (150) Xie, J.; Luan, B. L. Microstructural and Electrochemical Characterization of Hydroxyapatite-Coated Ti6Al4V Alloy for Medical Implants. *J. Mater. Res.* **2011**, *23*, 768–779.
- (151) Tran, P. A.; Sarin, L.; Hurt, R. H.; Webster, T. J. Opportunities for Nanotechnology-Enabled Bioactive Bone Implants. *J. Mater. Chem.* **2009**, *19*, 2653.
- (152) Vetrone, F.; Variola, F. Nanoscale Oxidative Patterning of Metallic Surfaces to Modulate Cell Activity and Fate. *Nano Lett.* **2009**, *9*, 659–665.
- (153) Ducheyne, P.; Radin, S. Phosphate Ceramic Coatings on Porous Titanium: Effect of Structure and Composition on Electrophoretic Deposition, Vacuum Sintering and in Vitro Dissolution. *Biomaterials* **1990**, *11*, 244–254.
- (154) Yi, J.-H.; Bernard, C.; Variola, F.; Zalzal, S. F.; Wuest, J. D.; Rosei, F.; Nanci, A. Characterization of a Bioactive Nanotextured Surface Created by Controlled Chemical Oxidation of Titanium. *Surf. Sci.* **2006**, *600*, 4613–4621.

- (155) Clair, S.; Variola, F.; Kondratenko, M.; Jedrzejowski, P.; Nanci, A.; Rosei, F.; Perepichka, D. F. Self-Assembled Monolayer of Alkanephosphoric Acid on Nanotextured Ti. *J. Chem. Phys.* **2008**, *128*, 144705.
- (156) G. P. Williams, Section 1.1 Electron binding energies. In: X-ray data booklet, edited by A. C. Thompson and E. Vaughan (Lawrence Berkeley National Laboratory, Berkley, 2010).
- (157) Jain, T.; Agrawal, T. The Haswell microarchitecture—4th Generation Processor. *Int. J. Comput. Sci. Inf. Technol.* **2013**, *4*, 477–480.
- (158) Grätzel, M. Photoelectrochemical Cells. *Nature* **2001**, *414*, 338–344.
- (159) Pingree, L. S. C.; Schmitz, M. J.; Kramer, D. E.; Hersam, M. C. Laser Assisted Field Induced Oxide Nanopatterning of Hydrogen Passivated Silicon Surfaces. *Appl. Phys. Lett.* **2007**, *073110*, 17–20.
- (160) Shestopalov, A. A.; Morris, C. C. J.; Vogen, B. N. B.; Hoertz, A.; Clark, R. L.; Toone, E. J. Soft-Lithographic Approach to Functionalization and Nanopatterning Oxide-Free Silicon. *Langmuir* **2011**, *27*, 6478–6485.
- (161) Crouse, D.; Lo, Y.-H.; Miller, A. E.; Crouse, M. Self-Ordered Pore Structure of Anodized Aluminum on Silicon and Pattern Transfer. *Appl. Phys. Lett.* **2000**, *76*, 49.
- (162) Lu, Y.; Chen, S. C. Nanopatterning of a Silicon Surface by near-Field Enhanced Laser Irradiation. *Nanotechnology* **2003**, *14*, 505–508.
- (163) McKendry, R.; Huck, W.; Weeks, B. Creating Nanoscale Patterns of Dendrimers on Silicon Surfaces with Dip-Pen Nanolithography. *Nano Lett.* **2002**, *2*, 713–716.
- (164) Rauscher, M.; Spohn, H. Porous Silicon Formation and Electropolishing. *Phys. Rev. E* **2001**, *64*, 031604.
- (165) Canham, L. Silicon Quantum Wire Array Fabrication by Electrochemical and Chemical Dissolution of Wafers. *Appl. Phys. Lett.* **1990**, *57*, 1046–1048.
- (166) Sato, K.; Shikida, M.; Matsushima, Y. Characterization of Orientation-Dependent Etching Properties of Single-Crystal Silicon: Effects of KOH Concentration. *Sensors Actuators A* **1998**, *61*, 87–93.
- (167) Gardelis, S.; Tsiaoussis, I.; Frangis, N.; Nassiopoulou, A. G. Ultra-Thin Films with Embedded Si Nanocrystals Fabricated by Electrochemical Dissolution of Bulk

Crystalline Si in the Transition Regime between Porosification and Electropolishing. *Nanotechnology* **2007**, *18*, 115705.

- (168) Model 487 Picoammeter/Voltage Source
<http://www.keithley.com/products/dcac/sensitive/lowcurrent?mn=6487> (accessed Sep 4, 2014).

APPENDIX

10.1. APPENDIX A. LABVIEW PROGRAM

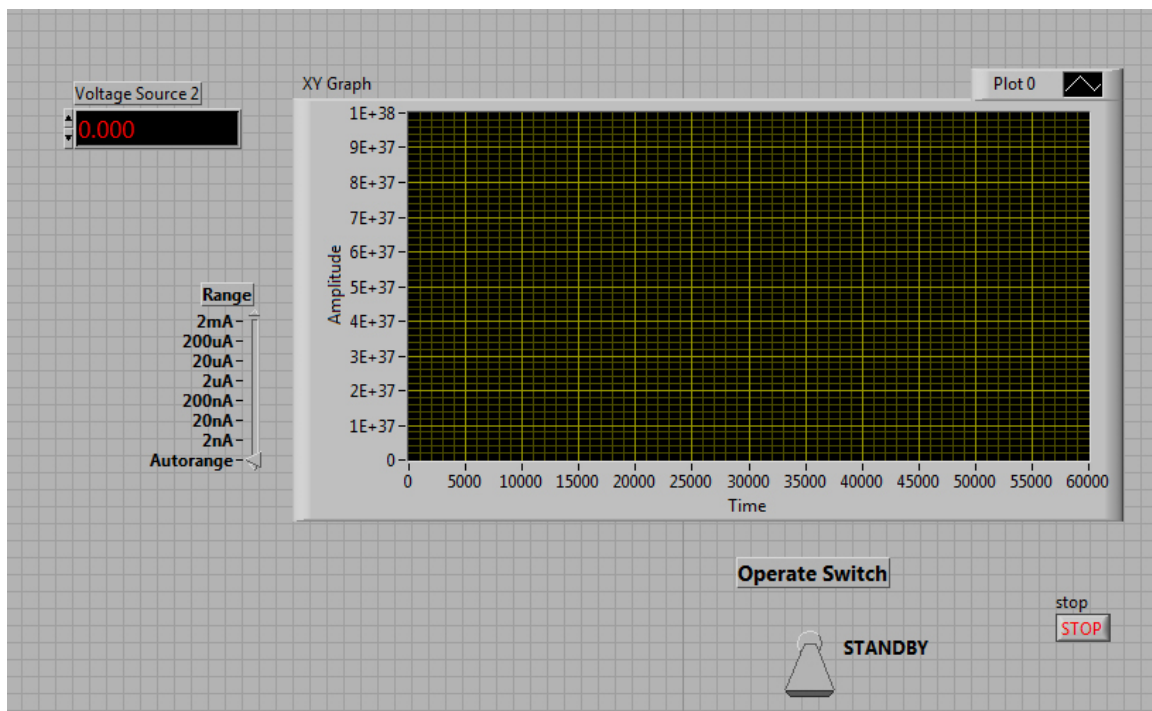


Figure 10.1 The front panel of the Labview program for Picoammeter.

This is the front panel (user interface) of the Labview program written for Picoammeter (*Keithley 487*)¹⁶⁸. Upon running of the program, the ‘operate switch’ is to be changed from ‘STANDBY’ to ‘OPERATING’. A voltage, as indicated by *Voltage Source 2*, will be provided by the Picoammeter. Current range can be chosen from ‘Range’ or ‘Aurorance’ can be selected. Current over time is plotted in the chart area real-time. After pressing ‘STOP’, the potential is turned off and the current data is automatically saved as a txt file.

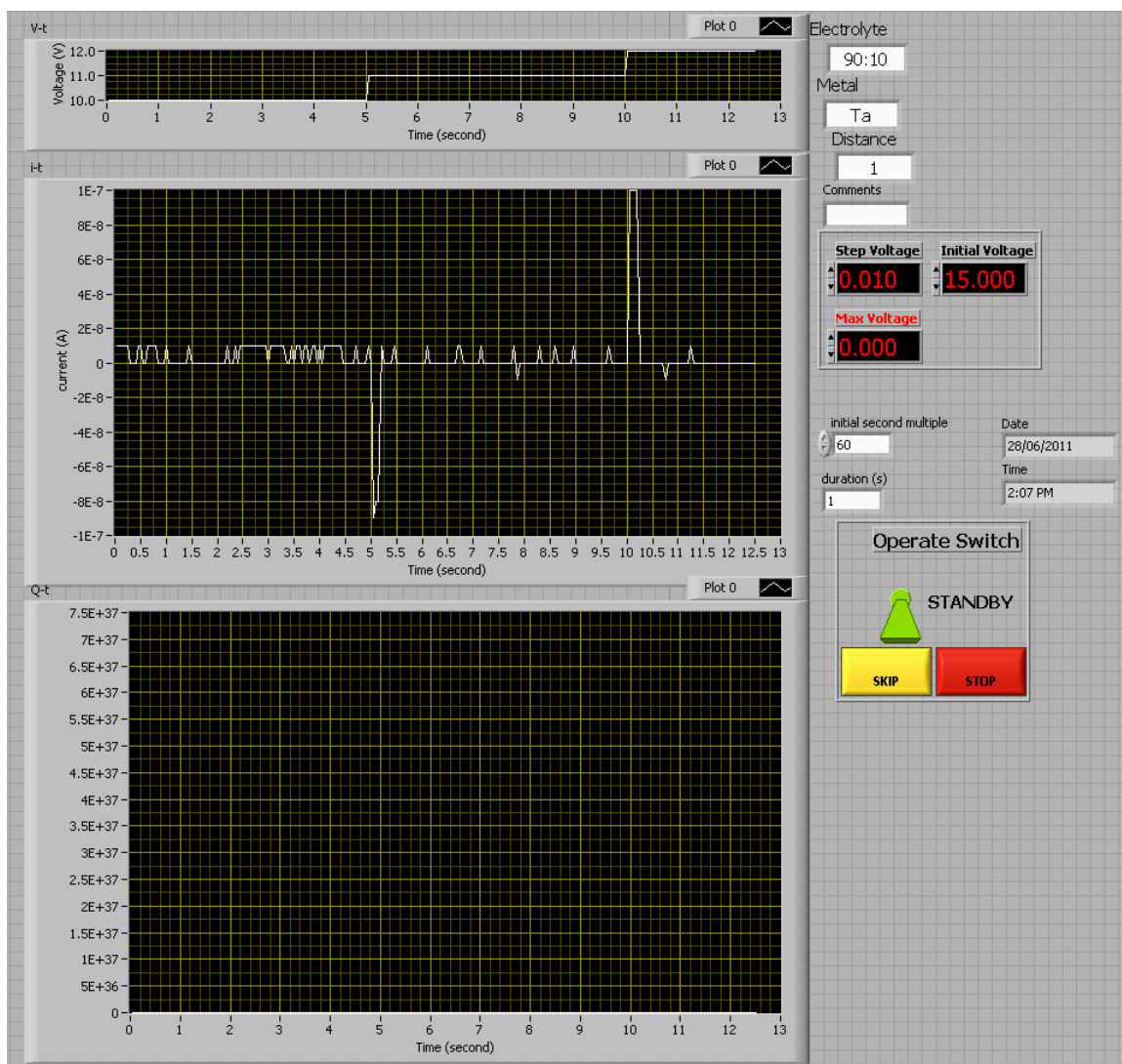


Figure 10.3. The Labview front panel of Version 2.0 for *Keithley 487*.

This is the Labview front panel (user interface) of Version 2.0 for the Picoammeter (*Keithley 487*). Inputs into ‘Electrolyte’, ‘Metal’, ‘Distance’, and ‘Comments’ will be saved to the first few lines of a txt file, together with experiment date and time, which are generated automatically.

The output potential can be programmed by ‘initial voltage’, ‘step voltage’, ‘Max voltage’ and the duration at each voltage. The actual voltage output will be plotted in the first chart (V-t) in real time.

Upon running of the program, an .exe file, the power source will be in the ‘STANDBY’ mode until the green switch is flipped up. The voltage, as programmed, will be provided by the Picoammeter. Current over time is plotted in the second chart (i-t). Current range is ‘Autorange’ by default. Current is integrated to give Charge, which is also plotted against time in chart Q-t.

‘Skip’ skips the present voltage and jumps to the next voltage. The voltage output will be turned off immediate, if ‘STOP’ is pressed or at the end of experiment as programmed. The current over time and charge over time data are automatically saved as a txt file, which can be imported into Excel for further analysis.

10.2. APPENDIX B CERTIFICATES OF ANALYSIS



EMD Chemicals Inc.
480 S. Democrat Road
Gibbstown, NJ 08027
Phone 856-423-6300
Fax 856-423-4389

Name: Hydrofluoric Acid
48%, GR ACS
Meets ACS Specifications

Formula: HF in water

Item Number: HX0621-2, HX0621-3

Formula Wt: 20.01

Lot Number: 52083

Data Order No: 000428957

CHARACTERISTIC	REQUIREMENT		RESULTS	UNITS
	Min.	Max.		
#Expiration date			31-MAR-2014	
Aluminum (Al)		0.05	0.008	ppm
Antimony (Sb)		0.03	0.00	ppm
Arsenic (As)		0.05	<0.05	ppm
Assay	48.5	50.5	49.17	%
Barium (Ba)		0.05	< 0.001	ppm
Beryllium (Be)		0.02	< 0.001	ppm
Bismuth (Bi)		0.10	< 0.001	ppm
Boron (B)		0.05	0.00	ppm
Cadmium (Cd)		0.05	< 0.001	ppm
Calcium (Ca)		1	0.007	ppm
Chloride (Cl)		5	<5	ppm
Chromium (Cr)		0.01	< 0.001	ppm
Cobalt (Co)		0.02	< 0.001	ppm
Color (APHA)		10	<10	
Copper (Cu)		0.02	< 0.002	ppm
Fluosilicic acid (H ₂ SiF ₄)		0.005	<0.005	%
Form			Clear liquid	
Gallium (Ga)		0.02	0.00	ppm
Germanium (Ge)		0.1	< 0.01	ppm
Gold (Au)		0.10	0.00	ppm
Heavy metals (as Pb)		0.5	<0.5	ppm
Iron (Fe)		0.5	0.012	ppm
Lead (Pb)		0.05	< 0.001	ppm
Lithium (Li)		0.02	< 0.001	ppm
Magnesium (Mg)		0.2	< 0.010	ppm
Manganese (Mn)		0.05	< 0.001	ppm
Molybdenum (Mo)		0.05	< 0.001	ppm
Nickel (Ni)		0.02	< 0.001	ppm
Nitrate (NO ₃)		5	<5	ppm
Phosphate (PO ₄)		0.5	<0.5	ppm
Potassium (K)		0.1	0.002	ppm

1/2

Residue after ignition		5	<5	ppm
Silver (Ag)		0.02	< 0.001	ppm
Sodium (Na)		0.2	0.004	ppm
Strontium (Sr)		0.1	< 0.001	ppm
Sulfate (SO ₄)		1	<1	ppm
Sulfate and sulfite (as SO ₄)		5	<3	ppm
Sulfite (SO ₃)		2	<2	ppm
Thallium (Tl)		0.05	< 0.001	ppm
Tin (Sn)		0.10	0.00	ppm
Titanium (Ti)		0.1	0.003	ppm
Vanadium (V)		0.05	< 0.001	ppm
Zinc (Zn)		0.1	0.002	ppm
Zirconium (Zr)		0.1	< 0.001	ppm

Gene A. Desotelle

Gene A. Desotelle,
Quality Control Manager

Release Date: 4/9/2012

EMD Chemicals Inc.
(Formerly EM Science, A Division of EM Industries, Inc.)
An Affiliate of Merck KGaA, Darmstadt, Germany



Certificate of Analysis

Product Name	SULPHURIC ACID	Chemical Formula	H ₂ SO ₄
Item Number	8825-1-05	Formula Weight	98.08
Lot Number	130624	UN Number	1830
Date Issued	Monday, August 18, 2014	CAS Number	7664-93-9
Gradename	Reagent		

Test Description	UoM	Limit	Result
Meets ACS Specifications		-	-
Appearance	N/A	Free and clear	Conforms
Assay	%	95.0 to 98.0	96.2
Maximum Allowable		-	-
Colour	APHA	10	< 10
Residue after ignition	ppm	5	< 5
Chloride (Cl)	ppm	0.2	< 0.2
Nitrate (NO ₃)	ppm	0.5	< 0.5
Ammonium (NH ₄)	ppm	2	< 2
Substances reducing permanganate (as SO ₂)	ppm	2	< 2
Arsenic (As)	ppm	0.01	< 0.01
Heavy metals (as Pb)	ppm	1	< 1
Iron (Fe)	ppm	0.2	< 0.2
Mercury (Hg)	ppb	5	< 5

Caledon Laboratories Ltd certifies that this copy of an electronic CoFA accurately represents the quality of the product and lot number indicated

40 Armstrong Avenue, Georgetown, Ontario L7G-4R9 Phone (905) 877-0101, Fax (905) 877-6666

SIGMA-ALDRICH®

sigma-aldrich.com

3050 Spruce Street, Saint Louis, MO 63103, USA

Website: www.sigmaaldrich.com

Email USA: techserv@sial.com

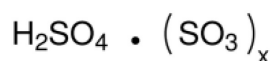
Outside USA: eurtechserv@sial.com

Certificate of Analysis

Product Name:

Sulfuric acid, fuming – reagent grade, 20% free SO₃ basis

Product Number: 435597
Batch Number: SHBD4215V
Brand: SIAL
CAS Number: 8014-95-7
MDL Number: MFCD00064589
Formula: H₂O₄S
Formula Weight: 98.08 g/mol
Quality Release Date: 25 JUN 2013



Test	Specification	Result
Appearance (Color)	Colorless to Yellow and Colorless to Brown	Colorless
Appearance (Form)	Liquid	Liquid
Purity (Titration by NaOH)	18.0 - 24.0 %	18.1 %



Jamie Gleason, Manager
Quality Control
Sheboygan Falls, WI US

Sigma-Aldrich warrants, that at the time of the quality release or subsequent retest date this product conformed to the information contained in this publication. The current Specification sheet may be available at Sigma-Aldrich.com. For further inquiries, please contact Technical Service. Purchaser must determine the suitability of the product for its particular use. See reverse side of invoice or packing slip for additional terms and conditions of sale.

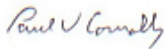
Certificate of Analysis		Alfa Aesar <small>A Johnson Matthey Company</small>
Product No.:	44105	
Product:	Vanadium wire, 0.25mm (0.01in) dia, 99.8% (metals basis)	
Lot No.:	K19Z022	
V 99.92 %		
Al	180	B < 10
Cr	< 20	Cu < 10
H	< 10	Mo < 10
Nb	< 100	Ni < 10
P	< 10	S < 50
Sn	< 50	Ta < 50
W	< 20	Zr < 10
C	< 100	
Fe	17	
N	50	
O	480	
Si	260	
Ti	< 10	

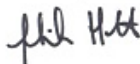
Values given in ppm unless otherwise noted

This document has been electronically generated and does not require a signature.

www.alfa.com

NORTH AMERICA Tel: +1 800 343 0860 or +1 519 521 0000 Fax: +1 800 322 4757 Email: info@alfa.com	GERMANY Tel: 0800 4566 0566 or +49 721 88307 200 Fax: 06066 4577 4577 or +49 721 88307 300 Email: Eurosales@alfa.com	UNITED KINGDOM Tel: 0800 801012 or +44 (0)1524 850506 Fax: +44 (0)1524 950688 Email: UKsales@alfa.com	FRANCE Tel: 0800 03 51 47 or +33 (0)1 6862 2090 Fax: 0800 10 20 67 or +33 (0)1 6862 8954 Email: France@alfa.com	INDIA Tel: +91 800 812424 or +91 800 812525 or +91 800 812626 Fax: +91 8416 266669 Email: India@alfa.com	CHINA Tel: +86 (21) 6542 8600 Fax: +86 (21) 6542 8651 Email: saleschina@alfa.com	KOREA Tel: +82 2 3146 6000 Fax: +82 2 3146 6062 Email: saleskorea@alfa.com
--	--	--	---	--	--	--

Certificate of Analysis		Alfa Aesar [®] <small>A Johnson Matthey Company</small>	
Tantalum foil, 0.127mm (0.005in) thick, annealed, 99.95% (metals basis)			
Stock Number: 10352			
Lot Number: D26S043			
Analysis			
Ta 99.99 %			
O	24	N	8
C	5	H	1
Fe	28	Ni	29
Cr	12	Cu	1
Si	2	Ti	1
Mo	4	W	12
Nb	9		
Values given in ppm unless otherwise noted			
Hardness		HV-108	
Certified by:			
			
Quality Control			
www.alfa.com			

Certificate of Analysis		Alfa Aesar <small>A Johnson Matthey Company</small>	
Tantalum wire, 0.25mm (0.01in) dia, annealed, 99.9+% (metals basis)			
Stock Number: 10348			
Lot Number: L28U044			
Analysis			
Ta 99.98 %			
C	35	Fe	38
H	< 10	Hf	< 5
Mg	5	Mo	19
N	12	Nb	240
Ni	11	O	120
Pb	< 5	Si	19
Ti	< 5	W	34
Zr	< 5		
Values given in ppm unless otherwise noted			
Certified by:			
			
Quality Control			
www.alfa.com			